

# Cross Calibration of the Measurements of the Electron Component of Extensive Air Showers of KASCADE-Grande and HEAT

ZUR ERLANGUNG DES AKADEMISCHEN GRADES EINES  
DOKTORS DER NATURWISSENSCHAFTEN  
VON DER FAKULTÄT FÜR PHYSIK DES  
KARLSRUHER INSTITUTS FÜR TECHNOLOGIE (KIT)

GENEHMIGTE

DISSERTATION

VON

Dipl.-Phys. Michael Wommer  
aus Neunkirchen/Saar

Dezember 2011

Tag der mündlichen Prüfung: 20. Januar 2012  
Referent: Prof. Dr. Johannes Blümer  
Korreferent: Prof. Dr. Thomas Müller



## Zusammenfassung

KASCADE-Grande ist ein Experiment am Campus Nord des Karlsruher Instituts für Technologie. Es ist dazu in der Lage, alle Komponenten von ausgedehnten Luftschauern, die bei der Wechselwirkung der kosmischen Strahlung mit der Atmosphäre entstehen, zu vermessen. Diese sind die Elektronenzahl ( $N_e$ ), die Anzahl der Myonen ( $N_\mu$ ) und die hadronische Komponente. Ziel des Experimentes ist die genaue Bestimmung des Energiespektrums und der Komposition der kosmischen Strahlung im Energiebereich von  $10^{16}$  eV bis  $10^{18}$  eV.

Gegenstand dieser Arbeit ist die Rekonstruktion des Energiespektrums der kosmischen Strahlung mithilfe der Elektronenkomponente ausgedehnter Luftschauer, gemessen mit KASCADE-Grande. Es wird in einem Zenitwinkelbereich zwischen  $0^\circ$  und  $40^\circ$  mit der Methode der konstanten Intensitäten die Elektronenzahl  $N_e$  auf die Absorption in der Atmosphäre korrigiert. Durch die Verwendung ausgedehnter Monte-Carlo Simulationen wird das Energiespektrum der kosmischen Strahlung bestimmt. Die resultierenden Energiespektren für die verschiedenen Kompositionsannahmen folgen einem einfachen Potenzgesetz. Schauerfluktuationen bilden den Grossteil der systematischen Unsicherheiten in der Bestimmung des Energiespektrums. Nach korrekter Berücksichtigung selbiger durch Anwendung eines Entfaltungsalgorithmus zeigen sich selbst im Allteilchenspektrum feine Strukturen, die bei einer Energie von circa  $10^{17}$  eV erscheinen. Desweiteren wird mithilfe des Elektronen-Myonen-Verhältnisses eine Massentrennung durchgeführt. Die erhaltenen Spektren für eine leichte und schwere Komponente sind vereinbar mit einer Kniestruktur für schwere Elemente (Eisen) bei einer Energie von circa  $10^{17}$  eV. Um die größte Unwägbarkeit der vorgestellten Methode zu vermeiden, wird eine Kalibrations-Prozedur entwickelt, die auf dem Vergleich mit Fluoreszenzmessdaten beruht. Diese wird mithilfe von Monte-Carlo Simulationen validiert und kann in naher Zukunft mit Daten der HEAT-Teleskope am Pierre Auger Observatorium durchgeführt werden.



## Abstract

KASCADE-Grande is an experiment for the detection of extensive air showers at Campus North of the Karlsruhe Institute of Technology. It is capable of measuring all different components of air showers, which arise when primary cosmic rays impinge on Earth. These are the number of electrons ( $N_e$ ), the number of muons ( $N_\mu$ ), and the hadronic component. The experiment aims for the precise determination of the energy spectrum and composition of cosmic rays in the energy range between  $10^{16}$  and  $10^{18}$  eV.

Subject of this thesis is the reconstruction of the energy spectrum of cosmic rays on basis of the electron component of extensive air showers measured by KASCADE-Grande. By the application of the method of constant intensities the electron number  $N_e$  is corrected for attenuation effects suffered in the atmosphere in a zenith angle range from 0 to  $40^\circ$ . With the help of extended Monte-Carlo simulations the energy spectrum of cosmic rays is inferred. The resulting energy spectra for the different composition assumptions can be described by a single power law. Shower fluctuations build the biggest part of the systematic uncertainties in the determination of the energy spectrum. Treating correctly the latter by employment of an unfolding algorithm even the all-particle spectrum shows fine structures which occur at an energy of approximately  $10^{17}$  eV. In addition, the electron muon ratio is used for the separation of different mass groups. The reconstructed spectra for a light and heavy component are compatible with a kneelike structure for the heavy elements (iron) at an energy of approximately  $10^{17}$  eV. In order to avoid the biggest difficulties of the presented method a calibration procedure is developed which relies on the comparison with fluorescence data. This procedure is validated with Monte-Carlo simulations and can be accomplished in the near future with data from the HEAT telescopes of the Pierre Auger Observatory.



# Contents

<b>1</b>	<b>Introduction</b>	<b>1</b>
<b>2</b>	<b>Cosmic Rays</b>	<b>3</b>
2.1	Energy Spectrum . . . . .	3
2.2	Composition . . . . .	6
2.3	Sources and Acceleration . . . . .	7
2.4	Extensive Air Showers . . . . .	9
2.5	Heitler-Model . . . . .	12
<b>3</b>	<b>KASCADE-Grande</b>	<b>15</b>
3.1	Layout . . . . .	15
3.2	Reconstruction of Shower Parameters . . . . .	20
<b>4</b>	<b>Electron Number Reconstruction</b>	<b>27</b>
4.1	Simulation Sets . . . . .	27
4.2	Lateral Density Functions . . . . .	29
4.3	Detector Resolution . . . . .	35
4.4	Data Sample . . . . .	37
<b>5</b>	<b>Constant Intensity Cut Method</b>	<b>43</b>
5.1	Zenith Angle Classification . . . . .	43
5.2	Electron Number Spectra . . . . .	44
5.3	Energy Conversion . . . . .	50
5.4	Sources of Uncertainties . . . . .	53
5.5	Composition, Y-Cut Method . . . . .	57
<b>6</b>	<b>Energy Spectra</b>	<b>59</b>
6.1	QGSjetII . . . . .	59
6.2	EPOS . . . . .	61
6.3	Deconvolution . . . . .	62
6.4	Y-Cut . . . . .	67

<b>7</b>	<b>The Pierre Auger Observatory</b>	<b>71</b>
7.1	Pierre Auger Observatory . . . . .	71
7.2	HEAT . . . . .	73
<b>8</b>	<b>Cross Calibration</b>	<b>77</b>
8.1	HEAT Electron Size . . . . .	77
8.2	Atmospheric Influence . . . . .	79
8.3	Cross Calibration . . . . .	80
<b>9</b>	<b>Conclusion</b>	<b>83</b>
<b>A</b>	<b>Appendix to Chapter 3</b>	<b>85</b>
<b>B</b>	<b>Appendix to Chapter 5</b>	<b>88</b>
<b>C</b>	<b>Appendix to Chapter 6</b>	<b>91</b>

# Chapter 1

## Introduction

Astroparticle physics is a almost hundred years old subdomain of physics which has made a huge progress during the last decades. In the year 2012 there will be the great event of the centenary of Victor Hess's discovery of cosmic rays. So already 100 years after mankind has firstly dealt with the charged particles reaching us from outer space they are still in the focus of science and can tell us a lot about our universe.

KASCADE-Grande is an air shower experiment located at Campus North of the Karlsruhe Institute of Technology. It is capable of detecting all the different components of extensive air showers, which arise when cosmic rays hit Earth's atmosphere. These are electron number ( $N_e$ ), muon number ( $N_\mu$ ) and hadrons. Main task of the experiment is the precise measurement of the cosmic ray energy spectrum and composition in the energy range  $10^{16}$  to  $10^{18}$  eV. Due to the low rates in this energy range it is only possible to interpret the footprint on ground level that is caused by the secondary shower particles for the investigation of the primary cosmic ray flux. For this interpretation it is necessary to apply sophisticated statistical methods. The cosmic ray energy spectrum follows over a wide range a power law  $\frac{dN}{dE} \propto E^{-\gamma}$ . At an energy of  $E_K \approx 4$  PeV a change of index occurs from  $\gamma \approx 2.7$  at lower energies to  $\gamma \approx 3.1$  for higher energies. This feature is commonly known as knee in the spectrum. It is mainly caused by the flux decrease of light elements (hydrogen and helium). This has been a main result of the data analysis of the KASCADE experiment [Ulr04]. At the moment the most probable model for the explanation of the knee forecasts a rigidity dependent position of the index change, i. e. the position is directly proportional to the corresponding elements valence:  $E_K^Z = Z \cdot E_K^H$ , with  $E_K^H \approx 4$  PeV being the position of the hydrogen knee. This means an expected knee position of approximately  $10^{17}$  eV for the iron component. The latter energy is not reached by the KASCADE experiment. That is one of the main reasons for the extension to KASCADE-Grande.

This thesis deals with the reconstruction of the cosmic ray energy spectrum analysing

KASCADE-Grande data. The application of a constant intensity method on basis of the observable electron number is explained. It benefits in a very high number of usable events due to the wide range in zenith angle from 0 to 40°. Basis for the here presented analysis is the spectrum of the electron number which is corrected for attenuation effects suffered in the atmosphere. Different methods are presented for the conversion from particle number of air showers which can be measured at ground level to the primary particle's energy. Especially the correct treatment of shower fluctuations by an unfolding method on basis of the Gold algorithm is enlightened. In addition a method for composition determination which is determined by the ratio of electrons to muons is presented. At the end of this work future prospects are given on how the dependence on detailed Monte Carlo simulations and in particular the high-energy interaction models can be reduced. For this purpose data from the low energy extension HEAT of the Pierre Auger Observatory can be used. HEAT has a overlap region of one decade in energy with the KASCADE-Grande experiment. Therefore the Grande measurements can be calibrated with fluorescence data taken by HEAT. To perform this cross calibration an electron number like measure for the fluorescence telescope is developed. So the correlation between electron number and primary particle's energy on basis of fluorescence data can be applied to KASCADE-Grande. In this way the measurement becomes more independent from hadronic interaction models.

# Chapter 2

## Cosmic Rays

Up to the year 1912 the scientific community had thought that the ionizing rays detectable at ground stem from natural occurring radioactive isotopes in the Earth. But then the Austrian scientist Victor Franz Hess has discovered during his balloon flights that the intensity of this radiation becomes stronger with increasing height above ground level [Hes12]. From this intensity gain he concluded that the radiation reaches the Earth from outer space and denoted it as ‘Höhenstrahlung’. In the year 1925 R. Millikan established the term cosmic radiation. Primarily those rays were thought to consist of high energetic photons, but at the end of the nineteen-twenties Compton besides others has discovered charged atomic nuclei being the most abundant ingredient of cosmic rays. Thirteen years later Pierre Auger and Peter Kohlhörster independently from each other revealed the phenomenon of extensive air showers, which are triggered by the interaction of high-energy cosmic radiation with the Earth’s atmosphere [Aug39]. Since that time the following questions are more or less unsolved and still relevant: What are the sources of cosmic rays? What elements are contained in cosmic rays and in which abundance? How can those particles be accelerated to such incredible high energies? During the course of the last century many generations of scientists have tried to answer these questions and a new subdomain of physics was born, the Astroparticle Physics.

### 2.1 Energy Spectrum

The energy of cosmic rays ranges from some keV up to roughly 0.1 ZeV [Bir95]. They mainly consist of protons and alpha particles. Up to an energy of 0.1 TeV the radiation is influenced by the solar wind, i. e. a modulation subject to solar activity is detectable. The lower the energy of this radiation the more it is shielded, therefore beginning from an energy of 0.1 TeV the undisturbed detection is possible without any interference. The energy spectrum of cosmic rays resembles over a wide range beginning from some

GeV up to the highest energies a steeply down dropping power law

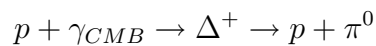
$$\frac{dN}{dE} \propto E^{-\gamma}$$

as depicted in Figure 2.1.

The power law gives a hint on the non-thermal origin of the radiation [Hör04]. The flux drops down over the whole energy range by more than 30 orders of magnitude. There are two distinct features in the spectrum where the spectral index changes significantly. In addition there are hints for many more not yet established smaller fine structures in the spectrum. The spectral index  $\gamma$  equals 2.7 up to an energy of roughly 4 PeV. Starting from here the slope of the spectrum becomes smaller. This down bending of the spectrum is commonly referred to as the knee in the cosmic ray spectrum. The value of the spectral index after the knee is roughly 3.1. For the explanation of this first index change in the spectrum many possible scenarios are currently under investigation.

Since our galaxy is not dominated by a magnetic field which is strong enough to confine particles with energies higher than the knee energy (their radius of gyration is too large), one possible explanation for the knee structure in the spectrum is the escape of the particles out of our galaxy during their propagation. In addition, in the most common acceleration mechanisms the knee energy is the upper limit of the achievable particle energy. Both scenarios lead to an index change whose position is proportional to the particle's valence. Extended investigations in this energy range by the KASCADE experiment have shown that the knee is directly caused by the drop of the light cosmic ray component, mainly hydrogen and helium [Ulr04].

In contrast to the former paragraph there is a further class of knee models, the so-called top down models which have the common feature that the position of the knee in the spectrum directly depends on the mass number of the cosmic ray particle. In one example of those models the different knee positions are directly explained by the energy loss high-energetic particles suffer when interacting with background particles in the galaxy. A complete survey on the various models leading to the different features in the cosmic ray spectrum can be found in [Hör04]. In the energy region between 0.1 EeV and 10 EeV the transition from galactic to extragalactic cosmic rays is supposed to occur. At an energy of roughly 4 EeV the spectrum flattens and  $\gamma$  equals again 2.7, this feature is referred to as ankle [Blu09]. The reduction of the intensity decrease with increasing energy at the ankle is supposed to be caused by the extragalactic component's advent. At an energy of roughly 60 EeV the Greisen-Zatsepin-Kuz'min-Cutoff (GZK-Cutoff) is expected to happen. Here the energy of the CMB photons in the rest frame of the proton nuclei is high enough to excite the proton to a  $\Delta$ -resonance:



or

$$p + \gamma_{CMB} \rightarrow \Delta^+ \rightarrow n + \pi^+.$$

That mechanism explains how protons stemming from distant sources loose energy. Or vice versa it gives a distance above which the universe becomes opaque for cosmic rays at the highest energies. So protons with an higher energy than  $6 \cdot 10^{19}$  eV are limited by this effect to a mean free path of approximately 50 Mpc [Gre66], [Zat66].

The flux of the radiation decreases from 1000 particles per  $\text{m}^2$  and s at one GeV to less

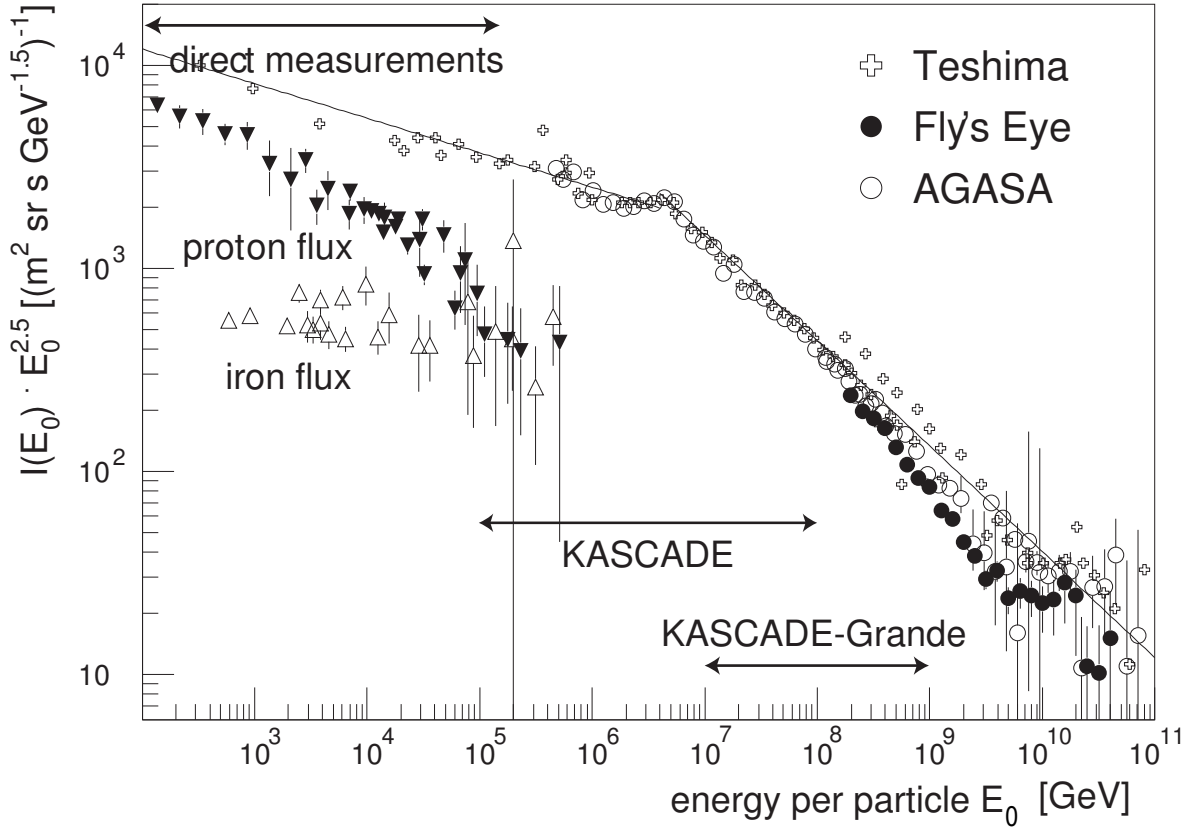


Figure 2.1: The energy spectrum of cosmic rays with marked measurement ranges of different experiments (source: [Mül03]). For reasons of structure clarification the flux was multiplied with  $E^{2.5}$ .

than one particle per  $\text{km}^2$  and century at the highest energies. That is one reason why direct measurements with limited detector area, like satellite or balloon experiments, e.g. TRACER [Mül07], are just feasible up to energies of some tenth of PeV. Due to the low flux and the limited technology for balloons and satellites, the investigation of cosmic rays with higher energies is only possible with detector arrays at ground which cover a large area. Those arrays consist either of particle detectors, fluorescence telescopes or radio antennas. With those apparati the secondary particles which were

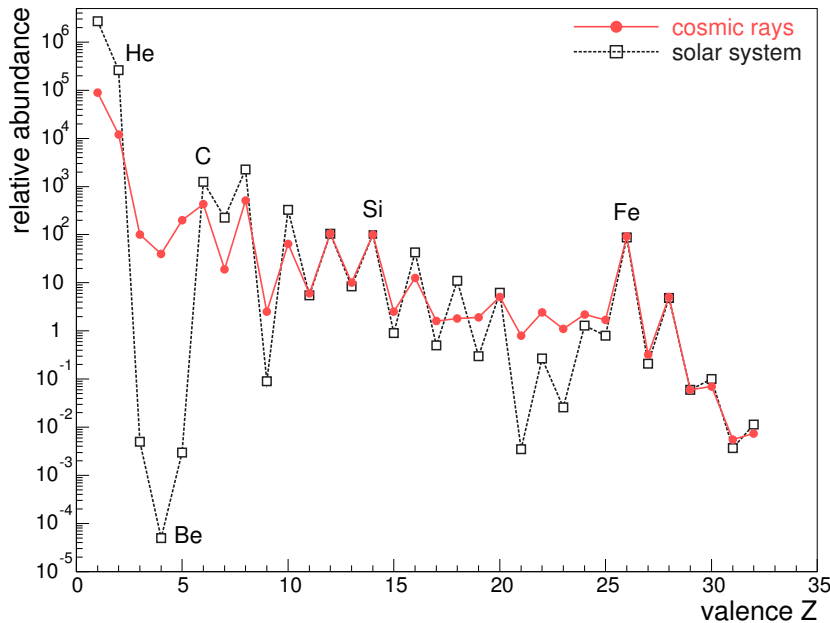


Figure 2.2: Comparison of elemental abundances in cosmic rays and our solar system, the values are normalized to silicon=100 (taken from [Mül03]).

produced in the atmosphere, the extensive air showers, are counted.

## 2.2 Composition

In the low energy regime up to about 100 TeV the flux is high enough to allow a direct measurement of the cosmic ray elemental composition via satellite or balloon experiments. In general all elements that we know in our solar system are also abundant in cosmic rays, which consist of 2% electrons and photons and the rest being charged atomic nuclei. The charged hadronic component of cosmic rays is composed of 85% protons, approx. 12% helium nuclei and approx. 3% heavier nuclei [Gru00]. Due to the very steep power law of the spectrum the latter values are dominated by the low energy region. The elemental abundances are very similar to the ones of our solar system with some distinct interesting features (confer Figure 2.2). Li, Be, and B are in cosmic rays more abundant than in our solar system. This fact can be explained by the spallation of nuclei of the CNO group. By inelastic interactions of the very abundant element iron the excess of elements with a charge number  $Z$  from 20 to 25 is explainable. The ratio of radioactive to the corresponding stable isotopes can give a hint on the age or the residence time in our galaxy of cosmic rays. A mean value of roughly  $10^6$  years can be calculated, e. g. from the  $\text{Be}^9/\text{Be}^{10}$ -relation [Gai90].

At the high-energy region of cosmic rays (means higher than 100 TeV) the current knowledge still lacks the exact mass composition. There are many hints on the development towards a heavier composition with increasing energy after the knee region [Fin11], confer Chapter 6.

## 2.3 Sources and Acceleration

### Sources

For that part of cosmic rays whose origin lies within our galaxy there are currently different possible sources under discussion. Two main source candidates are so-called supernova remnants (SNR) and pulsars. The energy density of cosmic rays equals  $1 \text{ eV/cm}^3$ , i. e. is of the same order as that of the cosmic microwave background although cosmic rays have a non-thermal origin. On basis of this value the necessary power for guaranteeing the energy content of cosmic rays can be estimated. It results in a value of  $5 \cdot 10^{40} \text{ erg}^\dagger$  for the required power taking 300 pc as thickness of our galactic disk, 30 kpc as its diameter and a mean sojourn time of roughly  $10^7$  years. The only appropriate objects in our galaxy which are able to provide such power are supernova remnants. The average released amount of energy by a supernova equals  $10^{51} \text{ erg}$  and at an average event rate of roughly three per century and galaxy just a tenth of its energy would have to be conferred to cosmic rays for producing the afore mentioned power.

At the examples of Cassiopeia A and SN 1006 it has been shown that the theories for the acceleration of cosmic rays in supernova remnants, developed by Berezhko et al. [Ber04], are consistent with experimental data. The data of these objects observed by the Chandra telescope are compatible with an efficient acceleration of hadronic cosmic rays inside and give hints on strong magnetic fields (in the case of Cas A:  $B \approx 500 \mu\text{G}$ , [Ber04]). Similar results can be reported by the HESS collaboration, especially the direct evidence of the existence of charged particles in SNR RX J1713.7-3946 by gamma ray observations the TeV region [Völ04] gives strong hints for supernova remnants being the source for galactic cosmic rays.

So-called active galactic nuclei (AGN) are currently the most probable candidates for the origin of the ultra-high-energy cosmic rays which reach us from outside our galaxy. In general an active galactic nucleus is an object consisting of a black hole in the centre surrounded by an accretion disk, which feeds the black hole, and perpendicular to the disk plane two jets of matter and radiation. With respect to the viewing angle it can be further classified (as blazar, Seyfert I, Seyfert II or radio galaxy). They possess all the essential requirements to accelerate cosmic rays via Fermi mechanisms (confer the following section). The direction correlation analysis by the Pierre Auger collaboration allows AGNs to be the sources of ultra-high-energy cosmic rays. In this analysis the linear extrapolation of arriving directions of cosmic rays at the highest energies ( $E > 55 \text{ EeV}$ ) are compared to the Veron Cetty catalogue positions of active galactic nuclei [Abr07]. By doing so it could have been shown a certain correlation. However in a following analysis with more statistics the effect is less pronounced but

---

<sup>†</sup>  $1 \text{ erg}[\text{ergodyn}] = 10^{-7} \text{ J/s}$

still detectable [Abr10a].

In addition there are further rather exotic models to answer the question on the origin. Even the decay of so-called topological defects could serve as source for the particles at highest energies. Though the decay of super-heavy dark matter particles or topological defects is likely not to be a good source candidate. The latter give a photon flux ten times too high with respect to the measured values by the Auger Observatory [Abr08]. The emission of ‘cannonballs’ [Dar07] is discussed as solution for the problem, too. The latter model could also explain the energy spectrum beyond the knee region [Pla02] applying second order Fermi acceleration.

## Acceleration and Propagation

A general description of possible processes which lead to an energy gain of charged particles was established by Enrico Fermi, whereat he was distinguishing two principal scenarios. In second order Fermi acceleration charged particles interact with moving magnetic fields, which are mostly embedded in a cloud of plasma. In this mechanism one particle gains per interaction a mean energy amount of  $\Delta E/E \propto (v/c)^2$ , with  $v$  being the speed of the plasma cloud containing the magnetic field. However first order Fermi acceleration is the more effective mechanism. It describes the acceleration of charged particles in a so-called shock wave, which can arise e.g. in a supernova explosion. The energy gain per traverse of the shock wave is direct proportional to the difference in speed of the media before and behind the impact zone. With the help of these acceleration mechanisms maximal particle energies of  $\approx Z \cdot (0.5 - 5)$  PeV (depending on the model) are achievable. Assuming a constant escape probability from the acceleration area for this kind of mechanism, an energy spectrum with the shape of a power law with an index of  $\gamma \approx 2$  is obtained. In the course of the further diffusion through the galaxy the exponent of the power law changes to  $\gamma \approx 2.7$  via propagation effects.

The stochastic deflection in magnetic fields during the diffusion of cosmic rays in the interstellar medium causes the isotropy of charged cosmic rays observed on Earth. Currently the question if there are certain anisotropies in the arrival direction distribution of cosmic rays, especially at the highest energies, is under investigation.

For the description of the propagation of the radiation certain transport equations are utilized. The latter take into account diffusion, energy change, interaction, creation and annihilation of particles (confer [Ber90]). The complexity of those equations becomes very often rather high. The introduction of boundary conditions simplifies the mathematical description. One example is the assumption of a time independent escape probability which leads to the so-called ‘leaky box model’. In addition there are further different models, for more details see [Gai90].

## 2.4 Extensive Air Showers

A high-energy charged particle coming from outer space initiates a cascade of secondary particles when hitting the Earth's atmosphere. This cascade develops through the complete atmosphere and its footprint can be detected at Earth's surface. The entity of particles in the atmosphere is commonly known as extensive air shower (EAS). In this context the adjective primary always indicates the impinging particle. Secondary refers to the produced particles in the atmosphere. In the first interaction whose position depends on relativistic energy of the primary particle and its cross section (typical height of 10 to 40 km) daughter particles are produced. The latter share the primary particle's energy and they self undergo further interactions, a particle cascade arises. The pancake-like shower front with a thickness of  $\approx 2$  m and a diameter of up to several kilometers blazes its trail through the atmosphere until the Earth's surface [Lon81].

The air shower can be subdivided in three different parts, an electromagnetic one, a muonic one, and a hadronic one (confer Figure 2.3). This particle avalanche reaches after a certain number of interactions its maximum. From there on the particle number decreases again because the particle energies are too low for further production of new reaction products. This cascade development is the detection principle on which air shower arrays are based. The atmosphere itself serves as calorimeter in which the detected particle interacts and deposits its energy.

### 2.4.1 Shower Components

#### Hadronic Component

The smallest fraction of the total particle number of an EAS is represented by hadrons. However they are strongly interacting particles (baryons and mesons) and therefore the biggest part of the primary particle's energy goes into the hadronic part. The reactions of the high-energy particles are strongly focused in forward direction. Therefore the hadronic component lies in the direct vicinity of the original arrival direction. The latter means that the shower core is build up by high-energy fragments of nuclei, baryons (mainly neutrons and protons) and mesons. In each hadronic interaction roughly a third of the energy is transferred to the electromagnetic component. The latter process works via the decay of neutral pions. The decay of the charged pions produces the muonic component of an extensive air shower. The interactions with the particles of the Earth's atmosphere can formally be described by:

$$A_{cr} + A_{air} \longrightarrow A'_{cr} + A'_{air} + \pi^{\pm}, \pi^0, K^{\pm}, K^0, \eta, n, p, \Lambda, A, \dots$$

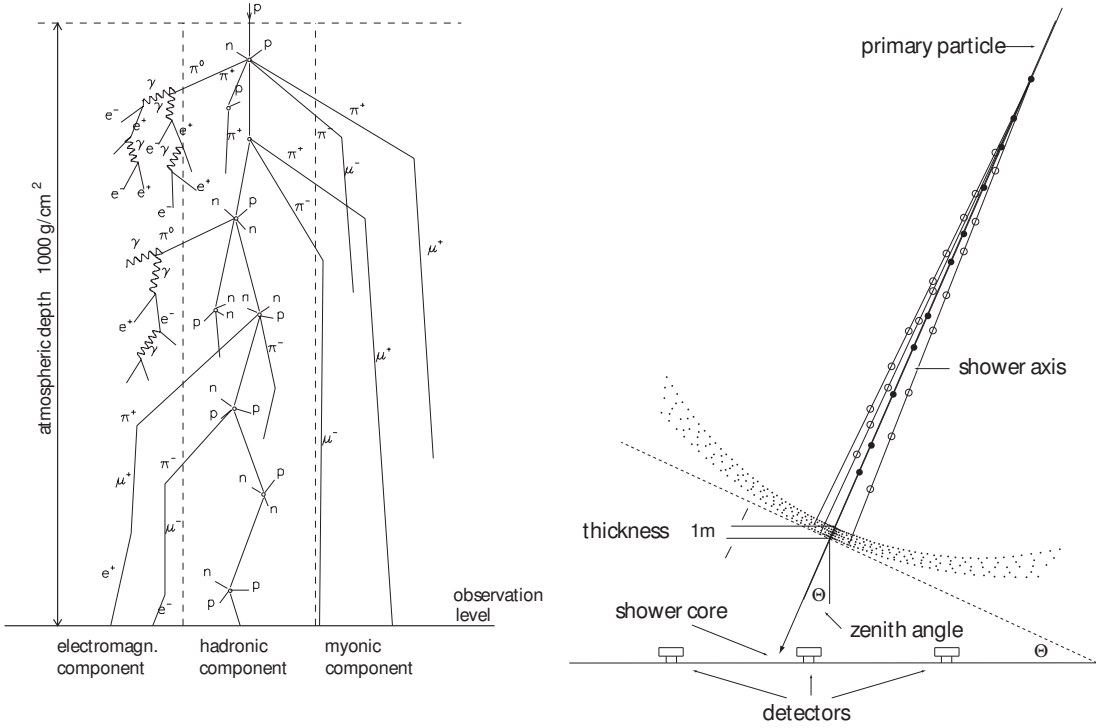


Figure 2.3: Left-hand side: scheme of an extensive air shower with its different components; right-hand side: arrival of shower front at ground [All75].

### Electromagnetic Component

The electromagnetic component consists mainly of electrons and photons. It is the part with the highest number of particles. The feeding source of this shower component is the decay of neutral pions into two photons:  $\pi^0 \longrightarrow \gamma + \gamma$ . These photons can produce electron-positron pairs as long as their energy is high enough. The electrons produce new photons via bremsstrahlung. This process is repeated as long as the energy is high enough.

To describe the lateral extent of the electromagnetic component, in many experiments a so-called NKG-function is utilized [Gre56]

$$\rho_e(r) = \frac{\Gamma(4.5 - s)}{\Gamma(s)\Gamma(4.5 - s)} \frac{N_e}{2\pi r^2} \left(\frac{r}{r_m}\right)^{s-2} \left(1 + \frac{r}{r_m}\right)^{s-4.5}. \quad (2.1)$$

This function is adopted to the measured distribution of the electron densities.  $\rho_e(r)$  is the electron density at distance  $r$  from the shower core;  $s$  is the lateral “age” parameter;  $N_e$  stands for the total number of electrons;  $r_m$  is the so-called Molière radius which is correlated to the multiple scattering. In the adjustment procedure the age parameter  $s$  and the Molière radius  $r_m$  lose their original meaning and depend in general on the

geographic position and the energy threshold of an experiment.

### Muonic Component

The muonic component of an extensive air shower is produced by the decay of mesons especially the decay of the charged mesons in muons. Since the particles of an EAS move almost at the speed of light, just a small fraction of the muons decays following

$$\mu^\pm \rightarrow e^\pm + \nu_\mu(\bar{\nu}_\mu) + \bar{\nu}_e(\nu_e).$$

The reactions which cause the attenuation, e. g. bremsstrahlung, are diminished for muons by a factor of  $(m_\mu/m_e)^2 = 10^5$ . Hence the muon number detectable at ground differs not much from that one in the shower maximum. Muons with energies of more than 100 GeV originate from an early stage of the shower cascade. Hence with their help information on the longitudinal shower development can be deduced.

An extensive air shower whose first particle was a hydrogen nucleus with an energy of 100 PeV holds at the observation level of KASCADE-Grande in average a muon number of  $N_\mu \approx 8 \cdot 10^5$  and an electron number of  $N_e \approx 2 \cdot 10^7$ . In contrast an air shower with the same primary particle energy but initiated by an iron nucleus holds in average a muon number of  $N_\mu \approx 10^6$  and an electron number of  $N_e \approx 8 \cdot 10^6$ . At observation level, taking the energy as constant, the electron size of a shower increases with decreasing mass number of the primary particle. The opposite holds for the number of muons. It increases with increasing mass number, because the muonic component is directly fed by the hadronic one. The electron number's variation range for different primaries' mass numbers is much bigger than the one of the muon size.

In addition there are other components which arise from extensive air showers. Charged particles generate Cherenkov light in the atmosphere when having highly relativistic velocities. This Cherenkov light is mainly emitted in forward direction. The secondary air shower particles can also excite the nitrogen molecules in the atmosphere. When these molecules deexcite they emit the energy difference as fluorescence light. The fluorescence light can be detected by special telescopes like in the Pierre Auger Observatory. One main difference when using Cherenkov or fluorescence telescopes for air shower detection is the measurement of a longitudinal profile instead of the footprint at ground level. The electrons of an air shower produce also an electromagnetic signal in the MHz range. This radio component is investigated by many collaborations in the world.

## 2.5 Heitler-Model

As the general topic of this work is the reconstruction of the energy spectrum of cosmic rays and especially the relation between number of electrons of an extensive air shower at observation level and energy of the primary particle above the Earth's atmosphere in the following section the Heitler-model is described. This model explains with basic physical approaches the individual nuclear reactions in particle cascades. Although it can't make such detailed predictions as for example today's Monte Carlo simulations with CORSIKA, it is very instructive and illuminates the basic processes in an extensive air shower. This model connects in a comprehensible way the number of particles in the maximum of the shower development with the initial physical quantities. Furthermore principal properties of the shower development in the atmosphere can be understood with the help of Heitler's basic explanations.

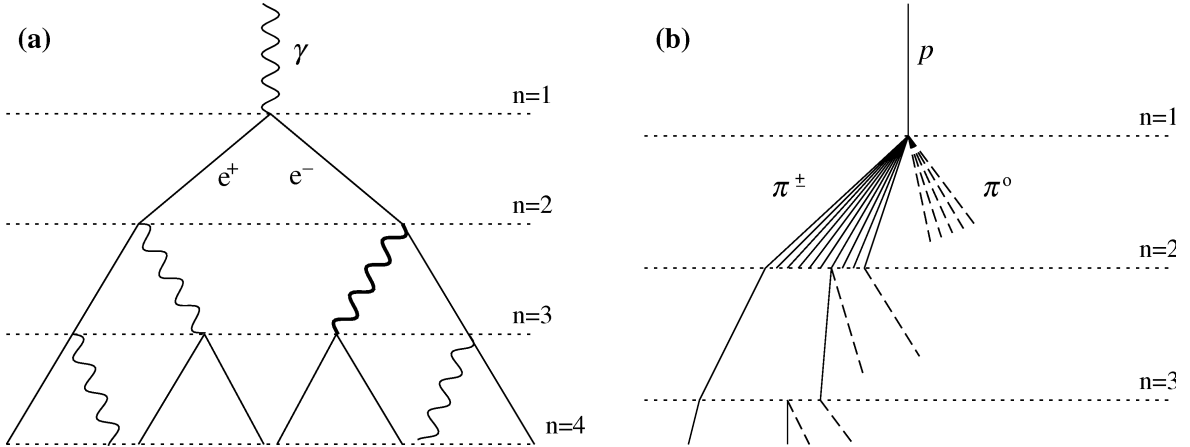


Figure 2.4: (a) electromagnetic cascade; (b) hadronic cascade, solid lines represent charged pions - dashed lines neutral pions.

Heitler invented as first a simple splitting approximation for the description of a photon induced electromagnetic shower [Hei44]. This model was further extended for the description of hadronic cascades by Jim Matthews [Mat05]. The main principle is that after each interaction length  $\lambda$  two new particles are generated like depicted in Figure 2.4. It is assumed that in each splitting the primary particle's energy is equally distributed to the arising particles. This process is repeated until the energy of the particles is not any longer sufficient enough for producing new particles. This energy threshold is called critical energy  $E_c$ . The following conclusion is the fact that the number of particles in the shower maximum is direct proportional to the shower inducing particle's energy and the depth of the shower maximum is growing linearly with the logarithmic primary particle's energy. These findings are illuminated in more details in the following. The current number of particles (subject to the column depth  $X$ )

is given by  $N(X) = 2^{X/\lambda}$ .  $X/\lambda$  denotes the number of interactions  $n$ . The maximal number of produced particles equals  $N(X_{max}) = E_0/E_c$  with  $E_0$  being the energy of the first particle which initiates the cascade. Thus the atmospheric depth at which the shower development culminates is described by  $X_{max} = \frac{\lambda}{\ln 2} \cdot \ln(E_0/E_c)$ . Another very instructive aspect of the Heitler model is the superposition principle. A shower which is started by a primary particle with mass number  $A$  and energy  $E_0$  can be described as the superposition of  $A$  proton induced showers with a by  $A$  reduced energy of  $\frac{E_0}{A}$ . By this model the differences in the shower fluctuations of different primaries can be explained. The heavier the primary particle the lower are the fluctuations of the secondary particles.

In addition there are several theories which extend the Heitler model, e. g. in [Hör07] the number of muons in the maximum of a shower is given by:

$$N_\mu \approx 5.77 \cdot 10^{16} \left( \frac{E_0}{1 \text{ PeV}} \right)^{2.97} N_e^{-2.17}. \quad (2.2)$$

Taking the muons as constant (their attenuation length is of comparable size as the atmosphere), with an assumed exponential electron attenuation (with  $\Lambda \approx 190 \frac{\text{g}}{\text{cm}^2}$ ,  $N_{e,Detector} = N_{e,max} \cdot \exp\left(-\frac{X_{atm}-X_{max}}{\Lambda}\right)$  and  $X = X(\Theta) = X \cdot \sec \Theta$ ) for the logarithmic electron size at observation level can be found:

$$\lg N_e = -0.46 \lg N_\mu + 1.37 \lg \frac{E}{\text{GeV}} - 0.43 \cdot \frac{X_{atm} - X_{max}}{\Lambda} \sec \Theta - 0.53. \quad (2.3)$$

$X_{atm} \approx 1023 \frac{\text{g}}{\text{cm}^2}$  is the observation level at KASCADE-Grande and  $X_{max}$  the depth of the shower maximum, whereat

$$X_{max} = 443 \text{g/cm}^2 + 70 \text{g/cm}^2 \lg(E/\text{PeV}) - 36.7 \text{g/cm}^2 \ln A$$

from [Hör07] is applied (with a mean logarithmic mass of  $\ln A \approx 2.5$ ). This leads to:

$$\lg N_e = -0.46 \lg N_\mu + 1.53 \lg \frac{E}{\text{GeV}} - 2.22 \sec \Theta - 0.53. \quad (2.4)$$



# Chapter 3

## KASCADE-Grande

The KASCADE-Grande experiment consists of the former EAS-TOP detectors [Agl88] and the original KASCADE detector (KARlsruhe Shower Core and Array DETector). The 37 detector stations of the Grande array are distributed on the area of the Karlsruhe Institute of Technology (KIT) Campus North (110m a.s.l.) like displayed in Figure 3.1. The extension causes the possibility to measure extensive air showers which are produced by cosmic rays up to an energy of 1 EeV. Hence the exploration of the energy region between knee and ankle, which is not well understood, is feasible. The scope subsequent to the knee is very interesting and important because in this region both the knee of the heavy component and the transition from galactic to extragalactic cosmic rays become apparent to occur.

The experiment consists of the former KASCADE-experiment [Ant03], the Piccolo trigger array and the Grande detector array. Every Grande station is equipped with approx. 10 m<sup>2</sup> of plastic scintillator with a thickness of 4 cm. The single stations are arranged on a hexagonal grid. The overall sensitive area which is covered by the detector array amounts to half a square kilometer [Nav04]. The mentioned detector properties lead to an average rate of four air shower events per second with an energy higher than 0.1 PeV. The Grande array detects the charged component of an air shower. The separation of electron and muon component is done with the help of the KASCADE array. A combined fit of the electromagnetic and muonic part provides the shower observables  $N_e$  and  $N_\mu$ . The Grande detector is working fully efficiently above an electron number of  $N_e \approx 10^6$  and a spatial resolution of 6.4 m, alternatively 0.6° [Pie07] for the arrival direction, is achieved.

### 3.1 Layout

In table 3.1 all the different components of KASCADE-Grande are displayed together with their specific properties. Characterized in detail as follows:

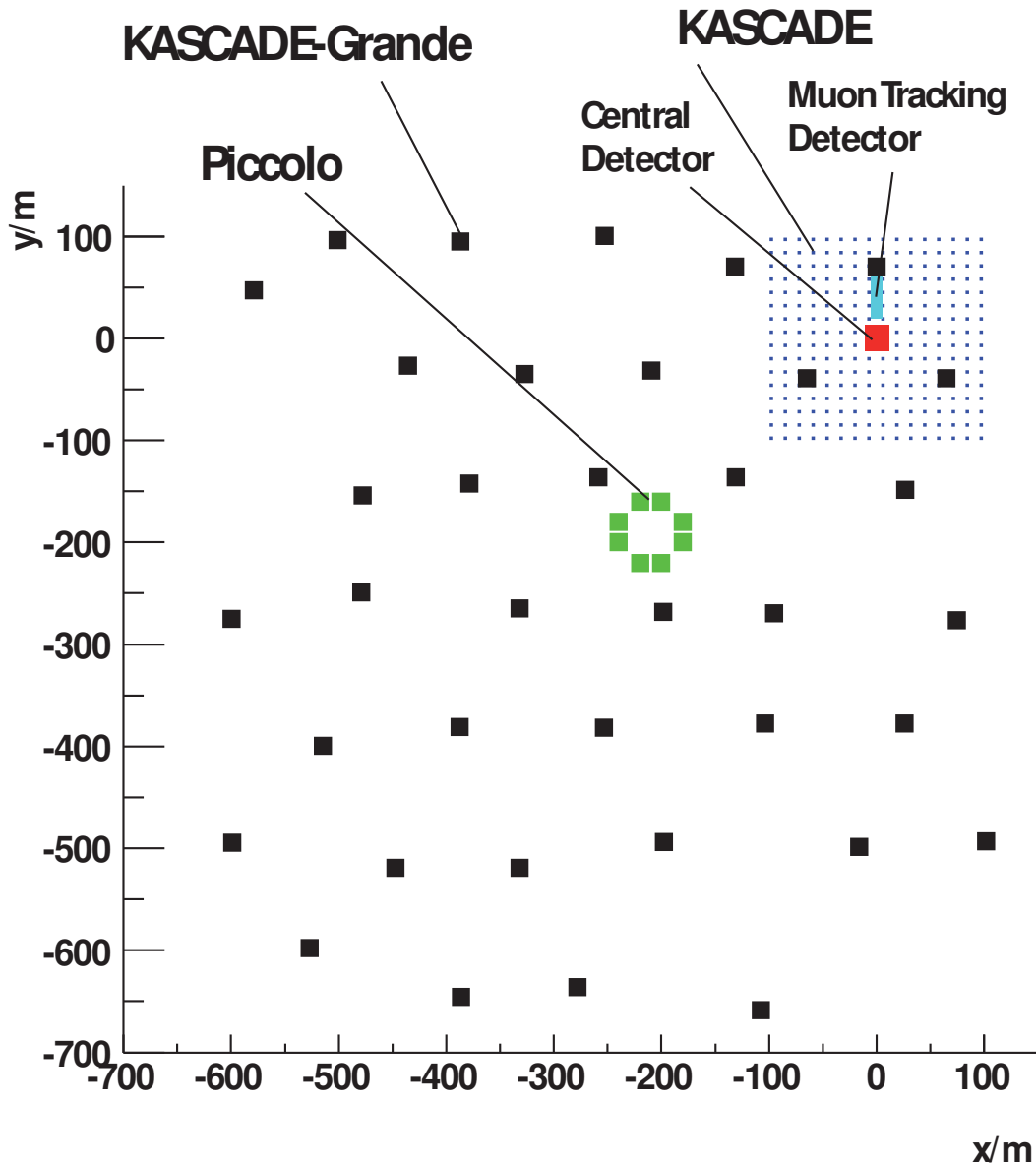


Figure 3.1: Sketch of the KASCADE-Grande detector array at KIT Campus North.

## KASCADE

The KASCADE-experiment comprises amongst others 252 detector stations which are able to discriminate between electrons and muons. These stations are aligned on a rectangular grid with a spacing of 13 m (confer Figure 3.2, left part). The sensitive area accounts for  $200 \cdot 200 \text{ m}^2$  and the array is subdivided in 16 so-called clusters, each of which comprises 16 detector stations. The four inner clusters consist of just 15 stations due to the position of the central detector in the middle of the array. In the 12 outer clusters every detector station itself is made up of 2  $e/\gamma$ -detectors and

detector	particles	area[m <sup>2</sup> ]	threshold
Grande	$e/\gamma + \mu$	370	5 MeV
Piccolo	$e/\gamma + \mu$	80	5 MeV
KASCADE-array (liquid scintillator)	$e/\gamma$	490	5 MeV
KASCADE-array (plastic scintillator)	$\mu$	622	230 MeV
MTD	$\mu$	4 · 128	800 MeV
central detector:			
calorimeter	$h$	8 · 304	50 GeV
trigger plane	$\mu$	208	490 MeV
MWPC	$\mu$	2 · 129	2.4 GeV
LST	$\mu$	250	2.4 GeV

Table 3.1: The different components of the KASCADE-Grande experiment and their specific properties. The given thresholds correspond to particle energies above the absorber materials of the detectors.

4  $\mu$ -detectors. The closer to the shower centre the more likely it is that hadrons and electrons penetrate the muon detector's shielding. Therefore the detector stations in the inner clusters are equipped with just 4  $e/\gamma$ -detectors and no muon counters. The detector area accounts just for a small fraction of the overall sensitive area (several percents) therefore only statements to local particle densities can be made. On basis of the latter the global shower properties, like electron and muon number, can be

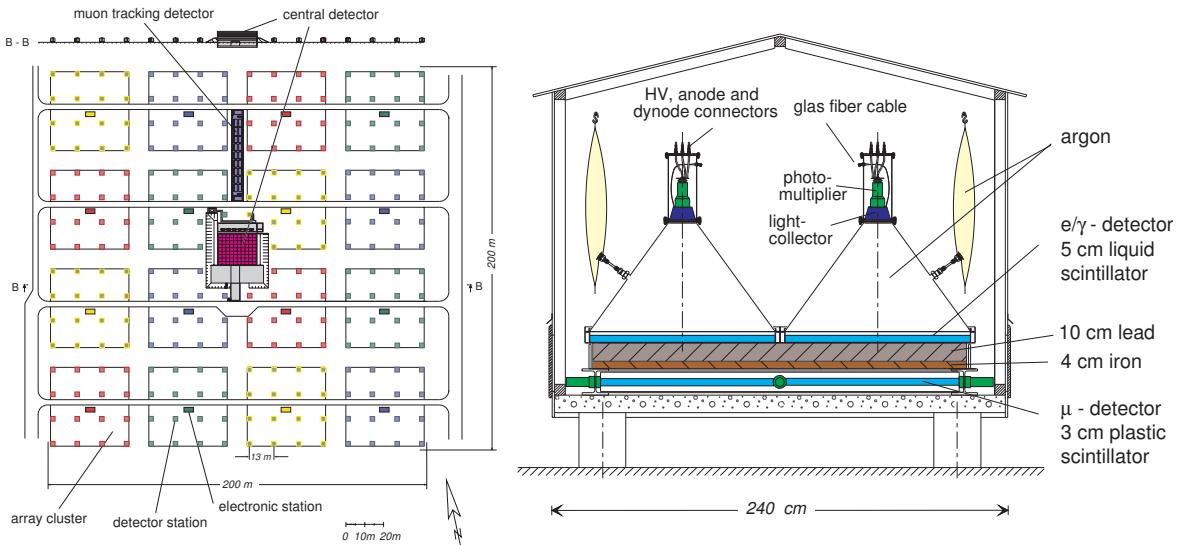


Figure 3.2: On the left-hand side: schematic view of the KASCADE-experiment; on the right-hand side: lateral cut diagram of a single KASCADE detector station.

calculated by different reconstruction procedures. Common to all these procedures is at first the reconstruction of the lateral density function which resembles the particle density subject to the distance of the shower core.

In Figure 3.2, right-hand side, the layout of a single KASCADE detector station is displayed. Every  $e/\gamma$ -detector is build up by a tub which is filled with organic scintillation liquid read out by a light collecting cone with photomultiplier. The corresponding mean energy resolution is 8% for an energy of 12 MeV, which is the average energy deposit of a minimal ionizing particle. At the afore mentioned energy the time resolution amounts to approximately 0.8 ns. In the outer cluster's detector stations the muon detectors (3 cm thick plastic scintillators) can be found below the  $e/\gamma$ -detectors shielded by layers of lead and iron. The energy resolution of these scintillators equals roughly 10% at an energy of 8 MeV which is the mean energy deposit of a minimal ionizing particle.

An additional detector part is the central detector which is located in the centre of the KASCADE array. It mainly consists of the hadron calorimeter. The latter is build by eight layers of liquid ionization chambers, each two of them separated by an iron absorption layer [Eng99]. The central detector is capable of detecting all three different shower components. The lowest section contains two layers of multi wire proportional chambers and one layer of limited streamer tubes which detect muons with an energy  $E > 2.4$  GeV with a position resolution of less than 10 cm.

The muon tracking detector (MTD) [Dol02] is located to the north of the central detector in an underground tunnel (dimensions:  $44 \cdot 5.4 \cdot 2.4$  m<sup>3</sup>). Above the tunnel there is a shielding of concrete, iron and soil to absorb the electromagnetic shower component. This shielding corresponds to 18 electromagnetic radiation lengths giving 0.8 GeV as energy threshold for vertical muons. With the help of these detectors the muon production height can be inferred. This observable is a good estimator for the primary particle's mass. With the muon production height it is also possible to perform detailed tests of hadronic interaction models.

## Piccolo

The piccolo detector array fulfils the task of connecting the Grande extension with the former KASCADE setup, in particular the muon detector of the central building and the muon tracking detector. This is done by providing a trigger signal for KASCADE and Grande. Very often for a shower whose core lies far apart from the KASCADE array the registered particle densities in the KASCADE detectors are too low for building a self trigger. On the other hand for inclined showers the delay times of the particles are too large for the transmission of a trigger signal via cable connection from Grande to KASCADE. The task of providing a trigger signal for both arrays can be fulfilled by the Piccolo detector which is situated between the center of the Grande array and

KASCADE. Piccolo consists of eight detector stations which are equipped with  $10 \text{ m}^2$  of plastic scintillator originating from the dismantled KARMEN experiment. The mean mutual distance between two Piccolo stations equals 20 m.

## Grande-Array

In Figure 3.1 the arrangement of the 37 Grande detector stations is depicted. The latter are with a mean distance of 137 m distributed on the area of KIT Campus North. They are further grouped in 18 trigger hexagons which contain 7 detector stations each. Every trigger hexagon is formed by 6 outer stations and one central station in the middle. A single station is equipped with 16 organic scintillation counters which form as a whole  $10 \text{ m}^2$  of sensitive detection area. The schematic setup is displayed in Figure 3.3. Via light collecting pyramids on whose ends photomultiplier tubes are installed the plastic scintillators are read out. The used photomultipliers (PMTs) have a signal yield of approximately  $1.6 \text{ pC/m.i.p.}^\dagger$ . The four inner scintillator modules are read out additionally by a PMT with a lower signal gain (roughly  $0.08 \text{ pC/m.i.p.}$ ) in order to avoid saturation effects. In this way the measurement can be assured even in those cases where the detector is directly hit by the shower core, and very high particle densities can be detected (up to several hundred charged particles per square meter). The collected data in the individual stations are transmitted to a central station therefore all stations are connected via 700 m long fibre optic cables with the central data acquisition station (Grande-DAQ).

## LOPES

LOPES (**L**Ofar **P**rototyp**E** **S**tation) is an experiment which detects the radio component of extensive air showers. It is located at the KIT Campus North at the same site as KASCADE-Grande. The start of LOPES is marked by the installation of 10 inverted V-shaped dipole antennae in the year 2003. Since its formation the experiment has been extended and improved several times, for details see [Neh08]. KASCADE-Grande is providing a trigger signal for the LOPES antennae. LOPES has detected cosmic rays for the first time unambiguously by the radio signal emitted by the secondary particles in the atmosphere [Fal05]. During the last years many different antenna types and configurations have been successfully developed and tested by the LOPES collaboration in Karlsruhe.

---

<sup>†</sup>minimum ionizing particle

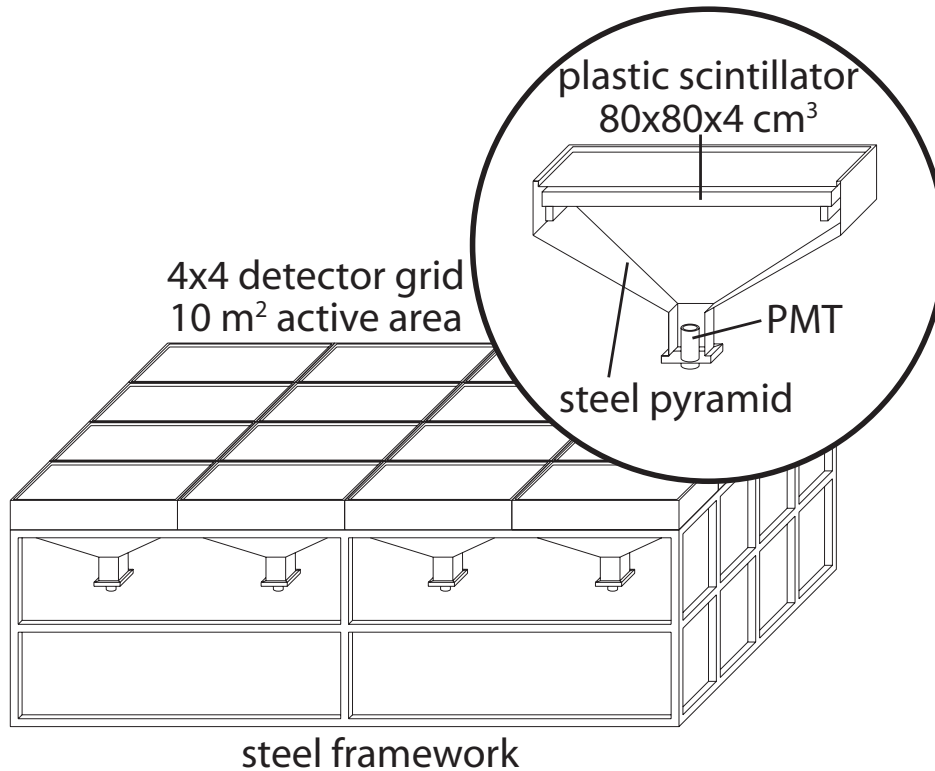


Figure 3.3: Schematic setup of a Grande detector station.

## 3.2 Reconstruction of Shower Parameters

The analysis of the raw data of the experiment (energy deposits and timing information) is conducted by an iterative process in three stages, referred to as level 1 to 3. The software package which performs the reconstruction is called KRETA (**K**ASCADE **R**econstruction for **E**x**T**ensive **A**ir showers). In the following subsections a detailed description of the different iteration steps for KRETA version 1.1901 is given which was developed entirely for this thesis in order to improve the electron number reconstruction. The here described KRETA version is different from the standard version usually used. In the beginning there is a quick and rough estimation process for the shower properties whose main purpose is the delivery of start values for the more precise procedures in the following reconstruction steps. In the KRETA version used for this thesis the modified KASCADE reconstruction procedure is applied (for more details see [Ant01]). The new feature of KRETA version 1.1901 is the possibility of using the data from KASCADE together with those from Grande, especially the information from the KASCADE  $e/\gamma$ -detectors is conserved for the reconstruction, instead of analysing both data sets in a more separated way like it was done before. By adding the density and timing information of the Grande detector stations into the KASCADE

reconstruction chain the KRETA software has been improved and is able to perform a combined reconstruction of data from both detector arrays. In order to exclude data from saturated KASCADE stations in the reconstruction chain, density values for KASCADE stations with a distance of less than 80 m to the shower centre are not taken into account. In the following the reconstruction procedure for air showers with high energies is explained (trigger signal in Grande for  $E > 3$  PeV).

In the second and third reconstruction step a NKG function is used to describe the lateral density functions of charged particles as well as electrons and muons:

$$\rho_{e,\mu}(r) = \frac{N_{e,\mu}}{2\pi \cdot r_m^2} \cdot \left(\frac{r}{r_m}\right)^{s-\alpha} \cdot \left(1 + \frac{r}{r_m}\right)^{s-\beta} \cdot \frac{\Gamma(\beta - s)}{\Gamma(s - \alpha + 2)\Gamma(\alpha + \beta - 2 - 2s)}. \quad (3.1)$$

In all the various cases in which the above function is applied the only fixed parameters are  $\alpha$ ,  $\beta$  and the molière radius  $r_m$ . There are just different values depending on the type of particle as well as the reconstruction level, as can be seen in table 3.2.

The general structure of the KRETA code is subdivided in single routines, so-called processors. Among them there is a Grande-, and a processor for the combined reconstruction. In every level of the reconstruction procedure the Grande processor runs at first and delivers the information concerning timing and also the arrival direction. After that the combined processor does its work and analyses the energy deposits.

## Level 1

In this first step the ADC- and TDC-channel entries are converted into energy deposits and time values using the current energy calibration data for the different detectors. In addition detectors with implausible energy or timing information are rejected by the comparison with the 8 nearest neighbouring stations. Such fake data can originate from uncorrelated muons or single hadrons which deposit their energies in the detectors. The final values form the basis for the calculation of the underlying physical parameters of the EAS in KRETA. The reconstruction starts in this level with the determination of rough estimators for the shower centre, arrival direction and the shower sizes (numbers of particles at observation level) by basic methods like weighting and calculation of the centre of gravity.

All the observables concerning the timing information are reconstructed by the Grande processor first. The direction of the impinging primary particle is determined in this level by a very simple procedure. The three detector stations with the highest energy deposits directly describe the plane shower front whose normal direction is parallel to the direction of the incoming cosmic ray particle. There is just one exception when the shower core lies inside the area of the KASCADE array. In this case also the shower core is reconstructed by the combined processor.

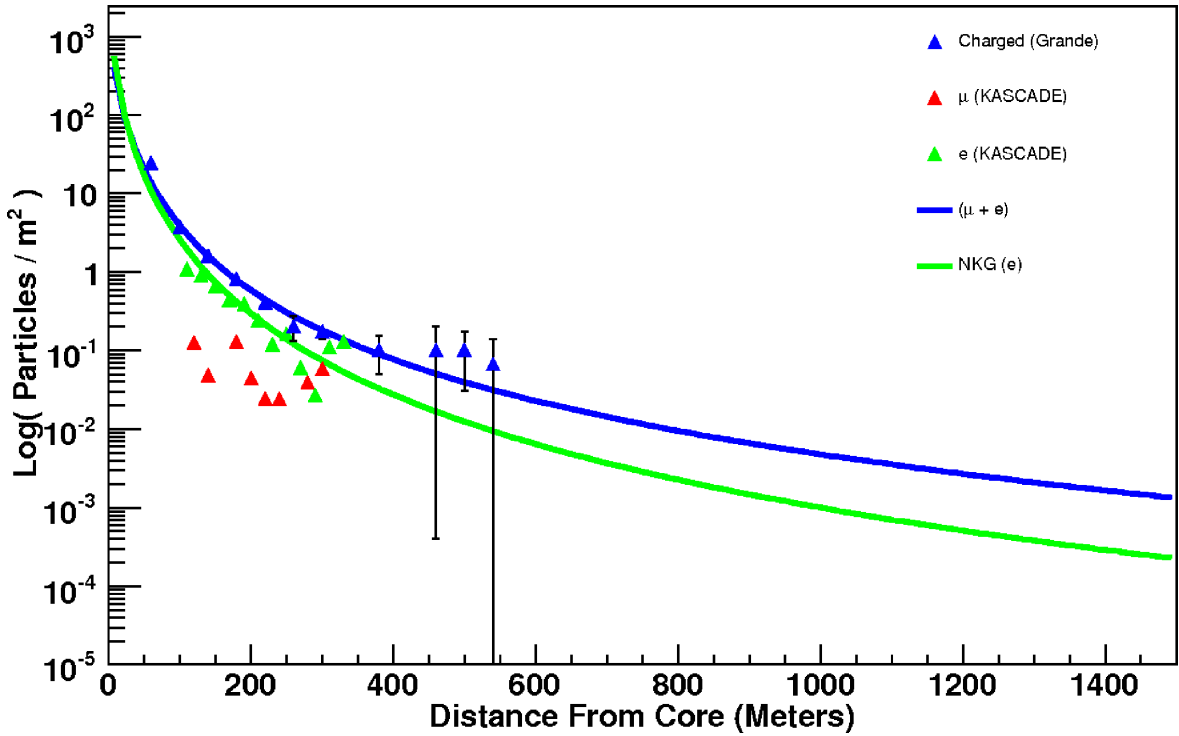


Figure 3.4: Example event's measured lateral density values. Shown are also the NKG functions fitted to the charged particle and electron densities (confer also [Cos09]).

Afterwards the processor for the combined reconstruction treats the energy deposit information from both the Grande and the KASCADE stations. The shower core is determined as a centre of gravity via weighting of the different detector positions with the corresponding recorded energy deposits. The number of charged particles is estimated by summing up the measured particles in the different detector stations and the expected values for the silent stations which are determined by a simple lateral density function with fixed parameters, especially the age parameter is not free (see  $s$  in equation 4.2). By the evaluation of an empirical formula which describes the dependence of the overall charged particle number on the deposited energy in the detector stations the first estimate for the number of charged particles is performed. The number of muons is reconstructed in a similar way. In this first stage the evaluation of empirical formulas subject to the summed up energy deposits in the muon detectors of KASCADE delivers the estimated muon number.

Those starting observable values serve in the subsequent reconstruction level as starting points for the adjustment procedures.

## Level 2

In general the second level of the reconstruction starts the main procedures. With level 1 entering as starting values all physical observables are reconstructed. Primarily in level 2 the charged particle density function is determined. Subsequently the muon density function is reconstructed. In table 3.2 the parameter values for the different NKG functions used for the adjustment of the lateral density functions are given. The parameter values for all levels have been optimized to guarantee a reliable and precise operation of the combined reconstruction of KASCADE and Grande data.

The first step in this level is the improvement of the arrival direction. Beginning with this reconstruction step all necessary physical variables are given in the shower frame in which the z-axis is defined by the shower direction. The standard procedure for the reconstruction of the arrival direction is using the timing information from all Grande detector stations by weighting them with the locally measured particle densities. In order to perform this weighting procedure the arrival time of the first particle per station is compared to a mean arrival time which is determined by simulations for a given radial distance to the shower centre. By this comparison a probability for being the real first particles of the shower front is attached to the first measured arrival time. The next step is the determination of the shower front via an adjustment procedure to the different arrival times from the detectors. In this fitting procedure the aforementioned probability is taken into account as a weight. As direct result the arrival direction of the cosmic ray particle is now known. As prerequisite for the described procedure the shower core has to be determined so this is the first possible level in which this procedure can be applied. The algorithm for the arrival direction reconstruction is described in detail in [Mai03].

In this iteration level particle numbers and densities are determined. With the help of so-called lateral energy correction functions (LECFs) the energy deposits are converted to particle densities. The LECFs are calculated on the basis of detailed Monte Carlo simulations and they take into account effects like the energy deposit caused by photons in the detector. In this way the energy deposit caused by photons and hadrons is taken into account when calculating the densities of e. g. charged particles in the detector stations. These functions describe the mean in the detectors deposited energy per particle as a function of distance to the shower centre. So the determination of the LECFs plays a decisive role in the reconstruction chain because they characterize the transition from energy deposits which are physically measured in the detectors to particle numbers which are the measures used in the final physics analyses. In addition these functions are adapted to different particle types, e. g. in the LECF for charged particles the ratio of charged particles to gamma particles is implicitly contained. The function for the conversion to muon densities has the main purpose of correcting the punch-through effect. As prerequisite for the application of the LECFs serve the values

for shower centre and zenith angle from level 1.

The improved direction information directly feeds the determination of the lateral density functions on the basis of new density values in this level. This is done by adjustment of a NKG function to the charged particle densities and to the muonic densities in shower disc coordinates. The corresponding parameter values which are used in this level of reconstruction are listed in table 3.2. The age value for the muon density function is parameterized subject to the charged particle number from level 1. The result of the core determination in this level is the final result, there are no more modifications in the next level of the reconstruction.

parameter	values for		
	$N_\mu$ all levels	$N_{ch,e}$ level 1&3	level 2
$\alpha$	1.5	1.6	1.6
$\beta$	3.7	3.4	3.5
$r_m$	420 m	30 m	20 m

Table 3.2: The fixed parameter values for the different NKG functions used in all levels of the reconstruction in KRETA.

### Level 3

In the last stage of the reconstruction algorithm the values for the inclination angles and the shower sizes are finalized, but the main task in this level is the splitting of charged particles into muons and electrons. No further modification for the position of the shower core is done in this stage. So the first step is a renewed conversion of the energy deposits to particle densities by application of the LECFs with the results of level 2 for the shower core position and the zenith angle.

With these new particle densities again a NKG function is fitted to the muon and charged densities with the parameter values as written in table 3.2 with fixed core position. In this last step the final distinction between muons and electrons is performed. It is done by adjusting a combination of fixed muon and free electron lateral density function to the charged particle densities coming both from the KASCADE detectors and the Grande detector stations. The overall particle numbers are then the result of the integration from  $r > 0$  until  $\infty$  of the lateral density functions. This step delivers the final values for electron number, muon number, and arrival direction. These reconstructed characteristic air shower parameters are then used in all further analyses. In Figure 3.4 the reconstruction of the lateral density function can be seen. Shown are the individual density values for the different shower

components originating from the last reconstruction level. For the charged particles and the electrons also the NKG fit function is displayed in this figure. It has to be mentioned that mean averaged densities are used. The binning is done around the shower core in circular rings with a thickness of 40 m in case of Grande densities and 20 m for KASCADE.

In the analysis presented in this thesis the main observable used is the number of electrons  $N_e$  because electrons form the most numerous component in an air shower and they directly excite nitrogen molecules in the atmosphere and cause in this way the fluorescence light of an extensive air shower. The meaning of the lateral density function in the reconstruction of the observable electron number  $N_e$  is illustrated in detail in the following chapter.



# Chapter 4

## Electron Number Reconstruction

This chapter deals with the reconstruction properties of the air shower parameter electron number (also called electron size). General studies on the lateral density function for KASCADE-Grande are presented. In addition the lateral density function adapted to full simulations is compared to the simulated true densities as well as the real measured densities. First rough estimations of the primary particles' mass can already be enabled by these comparisons. In the end the final uncertainties of the electron size subject to different variables are discussed. Similar studies as presented in this chapter but for the observable muon size can be found in [Bur07].

### 4.1 Simulation Sets

For the presented studies several sets of simulations are used. In all cases CORSIKA (**CO**smic **R**ay **S**imulation for **K**ASCADE, [Hec98]) was used to simulate the air shower events. CORSIKA is a Monte-Carlo simulation software which describes the development of an extensive air shower in the atmosphere in a probabilistic way. Therein the actual occurrence of single nuclear reactions is controlled by random numbers and the corresponding processes' cross sections which are given by hadronic interaction models. The **Q**uark-**G**luon-**S**tring-jet (QGSjet) models are based on the Gribov-Regge theory which describes the hadronic interactions by the exchange of hypothetical particles, so-called pomerons. The electromagnetic interactions are even at the highest energies completely described by quantum electrodynamics, that is the reason why the EGS-package [Nel85] is employed for the description of ionisation losses, bremsstrahlung, pair production, and scattering.

The outgoing results are characterized by the high-energy interaction model used in the simulations due to the lack of experimental data coming from collider experiments for these extreme energies. A good comparison between first LHC data and predictions stemming from interaction models can be found in [Ent11]. Therein the justification for the equal use of current high-energy interaction models like EPOS and QGSjetII [Ost06] is given.

After the simulation of the air shower until the Earth's surface the GEANT3 (**GE**ometry **ANd** **T**racking 3 tool, [Bru93]) based simulation tool CRES (**C**osmic **R**ay **E**vent **S**imulation) was applied for the description of the detector's response. The obtained data were then reconstructed with the KRETA code just the same way as for real data (confer Chapter 3.2). In CORSIKA different interaction models which characterize the shower physics are used. In the present investigations FLUKA [Fas00] as low-energy interaction model and QGSjetII [Ost06] as high-energy interaction model are adopted. The latter is the improved successor of QGSjet01 [Kal97]. The difference between these two models lies mainly in altered extrapolations for various reactions' cross sections. A further model used in the here presented analysis is EPOS [Wer06]. EPOS is a quantum mechanical multiple scattering approach on the basis of partons and strings.

A set of simulations contains fully (including detector simulation) simulated events which follow an energy spectrum  $\propto E^{-\gamma}$  with an index of  $\gamma = 2$ . This index was chosen as a good compromise between computing time and statistics. Each set of simulations consists of 114237 fully simulated showers in the first energy bin from  $5.62 \cdot 10^{13}$ eV to  $1 \cdot 10^{14}$ eV and ends up by following a  $E^{-2}$  spectrum with 5 events in the last energy bin from  $5.62 \cdot 10^{17}$ eV to  $1 \cdot 10^{18}$ eV. For a better description of the high energetic part there are additional simulation sets just at the highest energies. This high energy extension starts at  $5.62 \cdot 10^{17}$ eV and ends at an energy of  $3.16 \cdot 10^{18}$ eV. Within this energy range there are three energy bins containing 16, 9, and 5 events per primary particle type. So there is at least one energy intervall above the KASCADE-Grande detector energy range and hence the effect of fluctuations to lower energies can be studied in the whole measurement range, even for the highest energies. To increase the given statistics additionally each event is used several times (usually 10) at different randomly chosen positions of the detector array. This procedure is in the following referred to as oversampling. Due to this oversampling a special formula has to be applied for the calculation of statistical uncertainties in simulations. The multiple use of generated shower events enlarges the uncertainties, though the different showers are thrown to different array positions. In the end the different events are not totally statistically independent and this fact has been taken into account for the calculation of the error of the mean value as follows:

$$\sigma(\bar{x}) = \sqrt{\frac{\sigma_{\text{CRES}}^2 + (k - 1) \cdot \sigma_{\text{CORSIKA}}^2}{N \cdot k}}, \quad (4.1)$$

whereas  $k$  denotes the number of multiple uses of a single CORSIKA event and  $N$  the number of statistical independent showers thus  $N \cdot k$  gives the total number of events. The presented classification with respect to the arrival direction was chosen in order to guarantee the same expected number of air shower events in every angular bin, i. e.

interval no.	angle limits	acceptance / $A_{det}$
1	0 - 16.7°	0.26
2	16.7° - 24.0°	0.26
3	24.0° - 29.9°	0.26
4	29.9° - 35.1°	0.26
5	35.1° - 40.0°	0.26

Table 4.1: Limits of the different zenith angular ranges.

the same acceptance in every bin when full isotropy in distribution of arrival directions is given. The acceptance of a certain zenith angle bin beginning at  $\Theta_i$  and ending at  $\Theta_f$  amounts to:

$$\int dA \int d\Omega = A_{det} \cdot 2\pi \int_{\Theta_i}^{\Theta_f} \sin \Theta \cos \Theta d\Theta = A_{det} \cdot \frac{\pi}{2} (\cos(2\Theta_i) - \cos(2\Theta_f)).$$

The overall acceptance in the zenith angle range  $0 - 40^\circ$  equals  $1.30 \cdot A_{det}$  where  $A_{det}$  denotes the fiducial area of the detector. Dividing this value in 5 equal parts results in the angular subdivision given in table 4.1.

## 4.2 Lateral Density Functions

In every air shower experiment which measures particles the choice and adjustment of a proper lateral density function (LDF) plays a crucial role in the reconstruction of the primary particle's properties. The LDF specifies the mean particle density as a function of the distance to the shower core. Only the evaluation of the fitted lateral density function allows for the reconstruction of the overall shower sizes therefore the lateral density function plays a key role in understanding the signal of the detector. In this section lateral density functions for electrons measured by the KASCADE-Grande experiment are compared with CORSIKA Monte Carlo results. In the simulations itself the effect of the detector response on lateral density functions is investigated. By these studies it can be shown that the detector is understood well which is represented by the precise detector simulations.

Another aspect of lateral density functions is the sensitivity to the primary particle's mass. The electron lateral density function for a hydrogen induced air shower is steeper than the one for a iron induced air shower with same primary particle energy. In other words the steeper the lateral density function the younger is the air shower whereas the latter implies its development in the atmosphere started at a closer point to the Earth's surface. That means that at a certain constant distance far away from the shower core the electron density is larger the higher the mass number of the primary

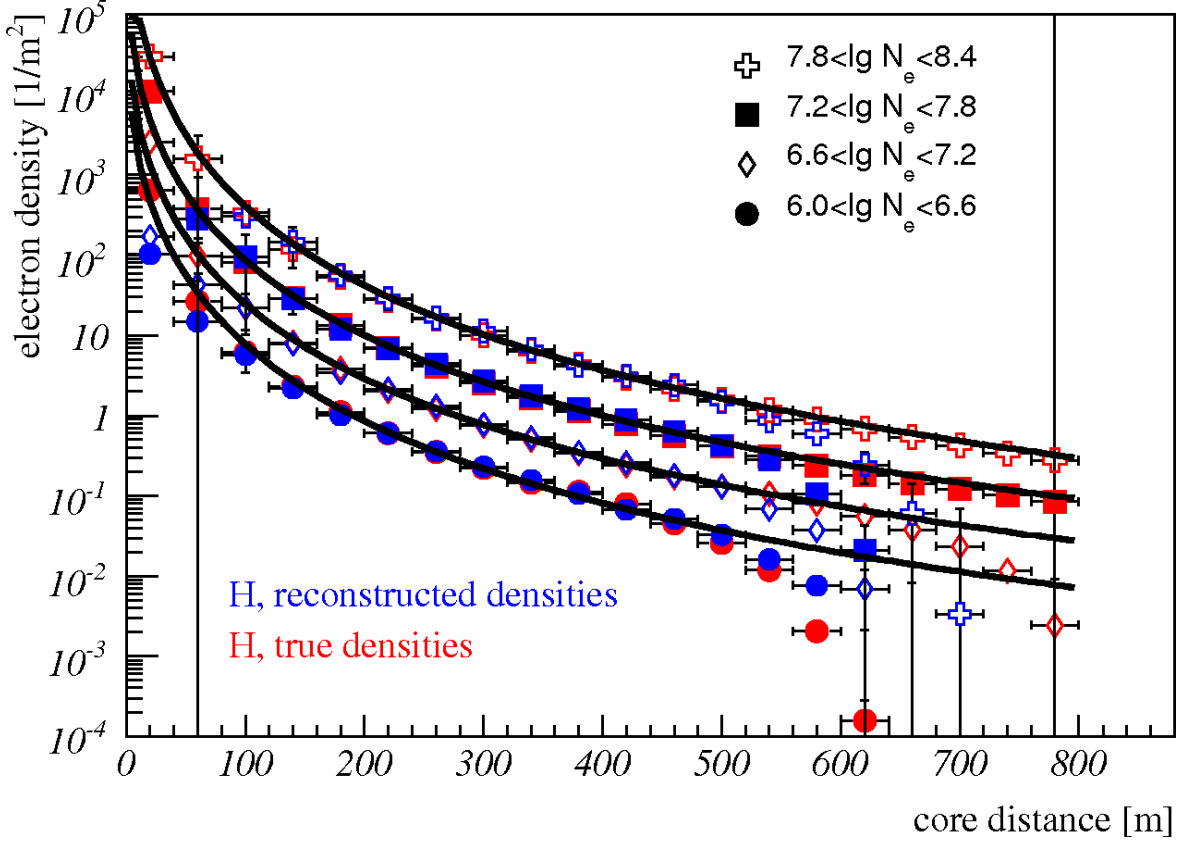


Figure 4.1: Simulated true CORSIKA mean lateral density functions in comparison with those with full detector simulation for a pure hydrogen composition. The shown functions are NKG functions which were adjusted to the reconstructed density values. The error bars represent the statistical uncertainties. Binning was performed in true electron number.

particle assuming besides mass the same cosmic ray properties. A comprehensive description of the lateral density functions used for the KASCADE experiment can be found in [Ape05]. The studies described in this section are inspired by the latter article and try to infer the corresponding results for the KASCADE-Grande experiment.

As described in section 3.2, in the KASCADE-Grande experiment a Nishimura-Kamata-Greisen (NKG) function is applied to describe pertinently the densities of electrons subject to the distance from the air shower centre:

$$\rho(r) = \frac{N_e}{2\pi \cdot r_m^2} \cdot \left(\frac{r}{r_m}\right)^{s-\alpha} \cdot \left(1 + \frac{r}{r_m}\right)^{s-\beta} \cdot \frac{\Gamma(\beta - s)}{\Gamma(s - \alpha + 2)\Gamma(\alpha + \beta - 2 - 2s)}. \quad (4.2)$$

As result of detailed simulation studies the parameters  $\alpha$  and  $\beta$  have been found to work best at values of 1.6 respectively 3.4. The Molière radius  $R_M$  is taken as 30 m for the here presented analysis. The above function (4.2) is Greisen's approximation to

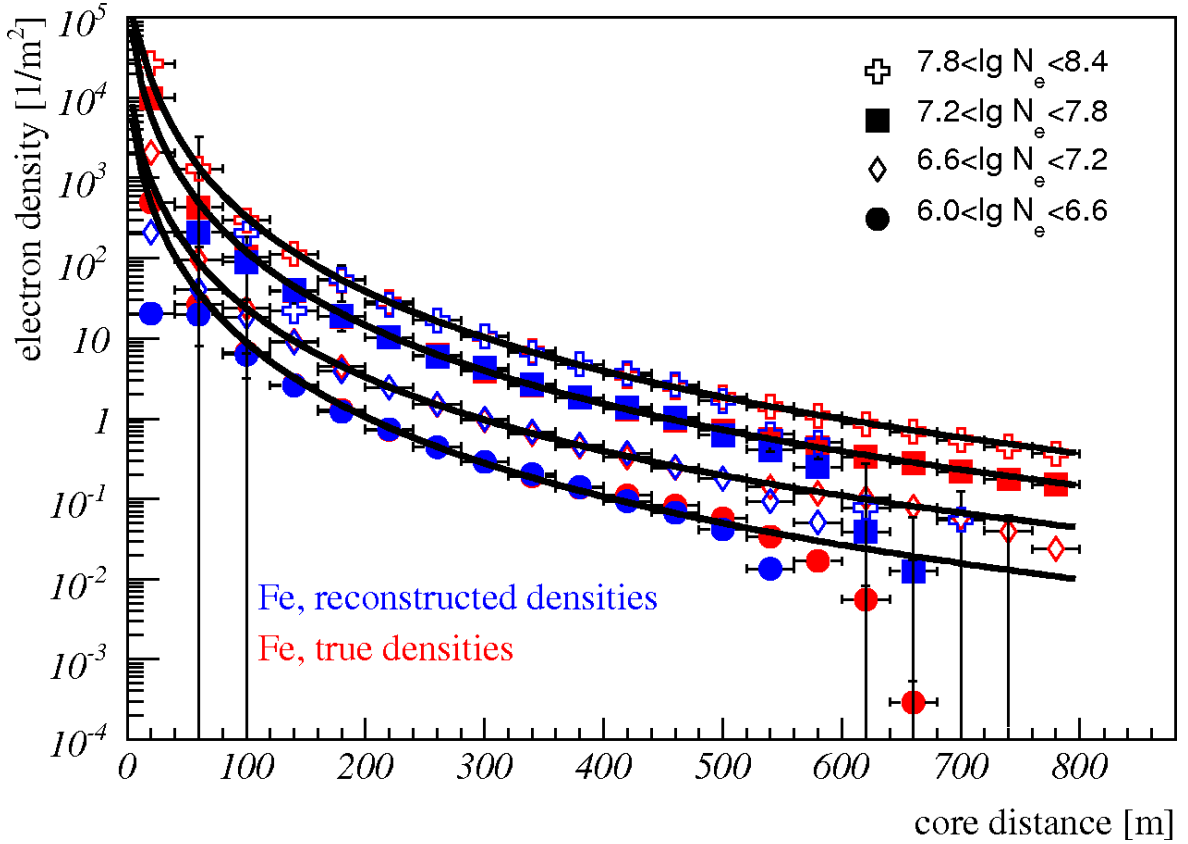


Figure 4.2: Simulated true CORSIKA mean lateral density functions in comparison with those with full detector simulation for a pure iron composition. Shown are NKG functions fitted to the reconstructed density values. The error bars represent the statistical uncertainties.

the Nishimura-Kamata functions which can be found in [Kam58]. In the latter work the authors performed detailed analytical calculations for electromagnetic showers. The figures in this section are all based on simulations which were performed with the models QGSjetII as high energy and FLUKA as low energy interaction model. The details of the simulation set are described in the previous section (Section 4.1). In Figure 4.1 the lateral density of electrons for Hydrogen induced air showers is depicted. Taken are just the simulated events from the first interval in zenith angle. Shown is the comparison of the true shower densities, named as 'true', and the densities coming out of the full detector simulation, called 'reconstructed'. Depicted are mean lateral density functions for different intervals of electron number as can be seen in the legends of the individual figures. For all investigations the binning was performed in true electron number. This figure shows that there are two main regions where problems, i.e. big differences between the true and reconstructed densities,

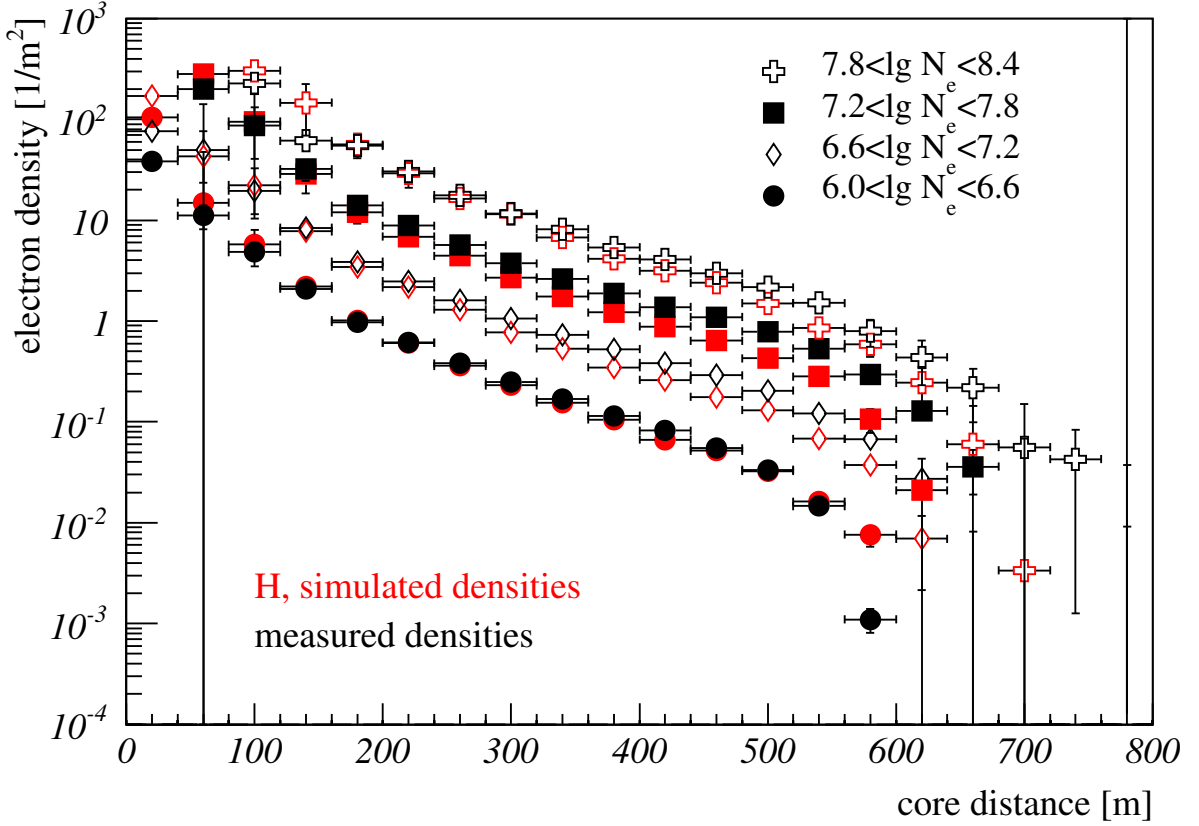


Figure 4.3: Real measured lateral density functions from data in comparison with Hydrogen simulations (QGSjetII), shown is the first angle intervall.

occur. In the direct vicinity of the shower centre the mean electron density is too low compared to the true density. This can be traced back to saturated detector stations which then decrease the electron density. But, as it can be seen in Figure 4.1, the restriction of the fit range of the NKG functions to an intermediate fiducial intervall, enables the functions to regive the true values of the densities even for distances in the vicinity of the shower centre. For all NKG functions shown in this section the fit range lies between 80 and 520 m. The medium range of the NKG functions which were adjusted to the reconstructed densities perfectly describe the true values. The second region with slight problems in the description of the real densities is far away from the shower centre. Here the densities are too low in direct comparison with the true ones. This is an intrinsic shortcoming of the method. Because it deals with mean values of densities the detector limit of one particle per  $10 \text{ m}^2$  ( $0.1 \text{ per m}^2$  in density) is undercut. The simulation data are running out of statistics for these high distances therefore the mean densities can reach such low values. But, the general description of the data with the adjusted function works very well.

The same behaviour as for hydrogen can be seen for a pure iron composition. In Figure

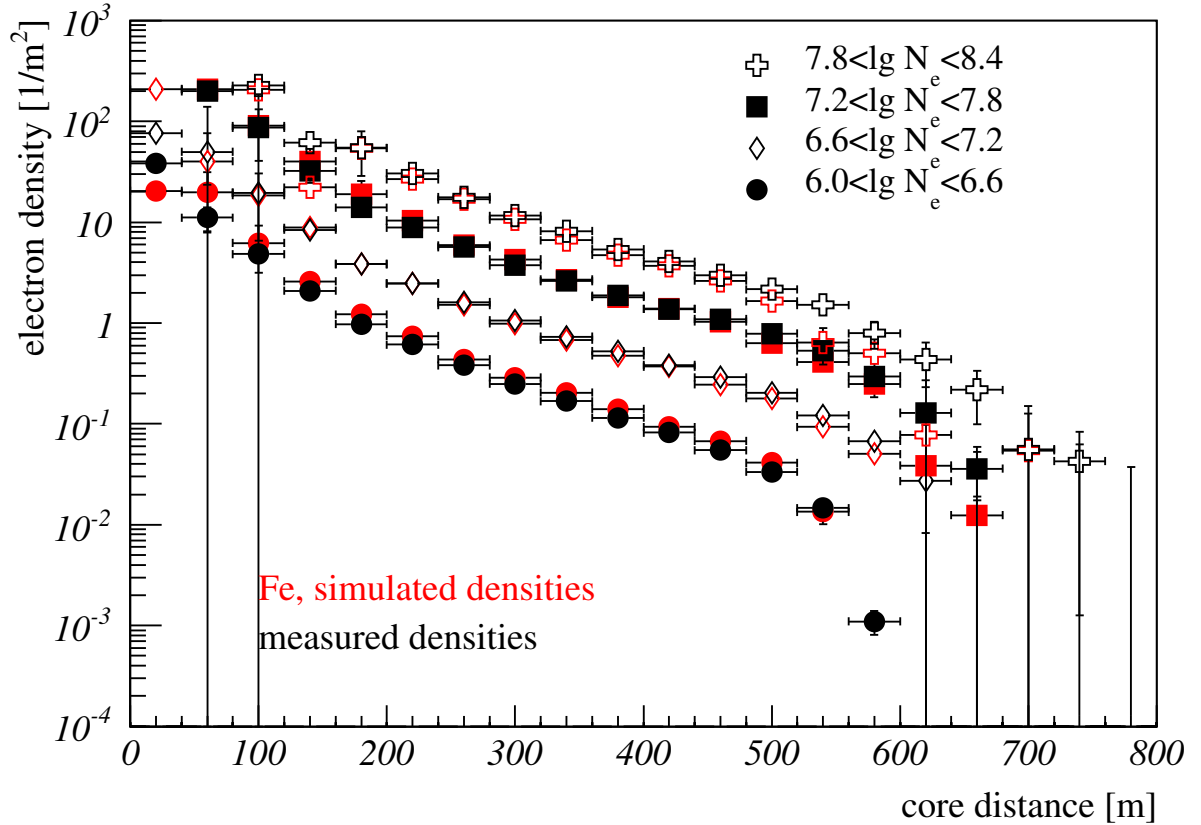


Figure 4.4: Measured real data lateral density functions in comparison with Iron simulations (QGSjetII) for the first angular range.

4.2 the mean lateral electron densities are given up to a zenith angle of  $16.7^\circ$  for iron induced air shower simulations. The displayed graphs are fits of NKG functions to the fully simulated shower densities for the individual size ranges. The true CORSIKA densities are compatible with the reconstructed NKG functions. The lateral density functions for iron show in general a flatter course than for lighter primary particles. In the following section a compilation of the measured data densities and the full simulated ones is described. In Figure 4.3 the comparison of hydrogen simulations with the measured data lateral density functions for the most vertical air shower events is shown. In this depiction the densities for different electron size intervalls are shown. In first approximation the energy of the inducing particle scales with the shower size, so the higher size values correspond to higher energies. It can be seen that the lightest primary particle's simulations agree best with data for low energies, in the beginning of the energy intervall. With increasing size and energy the lateral density functions for hydrogen simulations more and more differ from the measured distributions. This implies a decreasing hydrogen fraction with increasing energy which causes the average mass number to become higher.

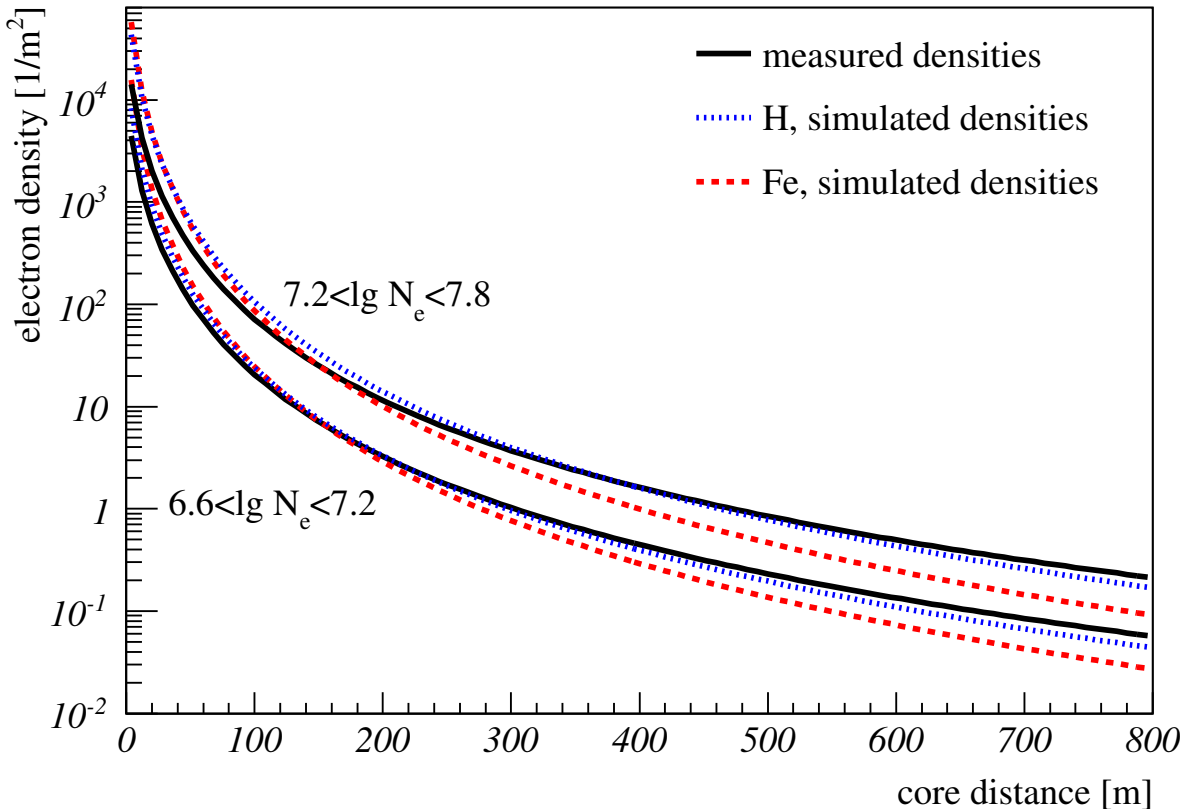


Figure 4.5: NKG functions fitted to data, hydrogen simulations, and iron simulations. Shown are the functions for the second and third electron number interval.

In contrast to the former section in Figure 4.4 a compilation of the real measured electron densities and the simulations for iron induced air showers is shown. The iron simulations give a good data description for those density values stemming from the highest energies.

In Figure 4.5 a compilation of the fitted NKG functions is given. For the second and third electron number interval the adjusted NKG functions for measured data, hydrogen simulations, and iron simulations are compared. One possible reason for the differences of data and the iron simulations function can be that for simulations the true electron number was used for binning whereas for measured data the reconstructed electron number was used. According to the course of the different functions in Figure 4.5 in measured data we had elements slightly heavier than iron. However slight differences are expected because in simulations models dominate the main shower properties. Keeping in mind this aspect the simulations describe the measured data distributions sufficiently well.

### 4.3 Detector Resolution

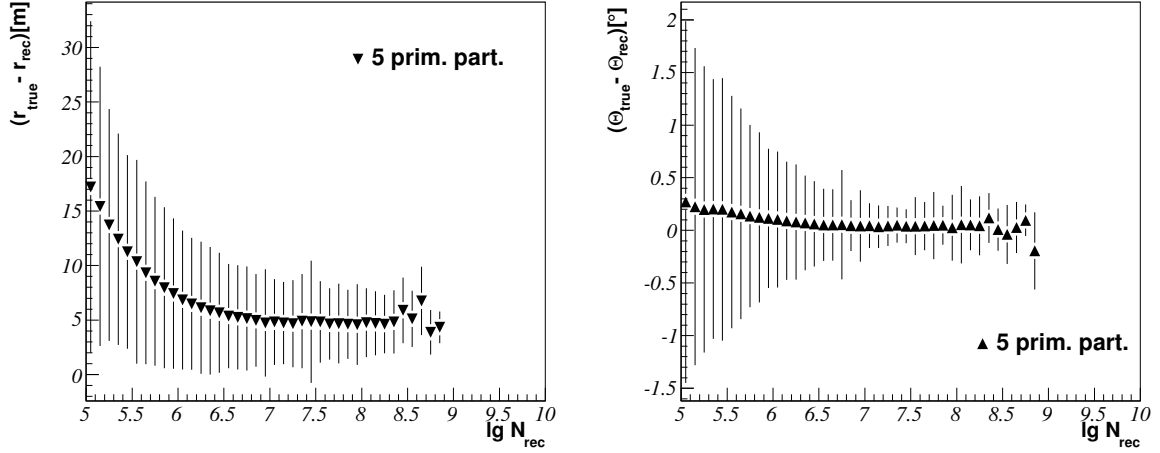


Figure 4.6: In both pictures the error bars represent the spread of the distributions, markers represent bias. Simulated data are contained from 0 to 40° zenith angle for a composition consisting of 5 primary particles in equal proportions. Left: Resolution of shower core. Right: Zenith angle resolution.

In this section important information concerning the main observables used in the analysis can be found. As the number of secondary electrons is the main observable in this work the uncertainties of this variable is crucial for the quality of the whole analysis. The zenith angle has a direct influence on the absorption correction applied in this work. The number of muons is used for the separation of light and heavy primary particles. For the event selection concerning the fiducial area a precise knowledge of the shower core coordinates is necessary. The only possible access to investigate the precision of the detector in reconstructing the aforementioned observables is the employment of detailed Monte Carlo simulations. For all the figures shown in this section the same quality cuts as for the data sample have been applied. The left part of Figure 4.6 shows the resolution in core position determination of air shower events. The graph describes the uncertainty in the position reconstruction of cores as a function of the reconstructed electron number. The markers represent the bias, the error bars symbolize the spread of the individual distributions and therewith the resolution. The core position resolution equals approximately 5 m. In this special case bias and resolution are of the same order of magnitude because the difference between reconstructed and true radius vector for the shower core coordinates is plotted. The right part of Figure 4.6 shows the resolution of the zenith angle subject

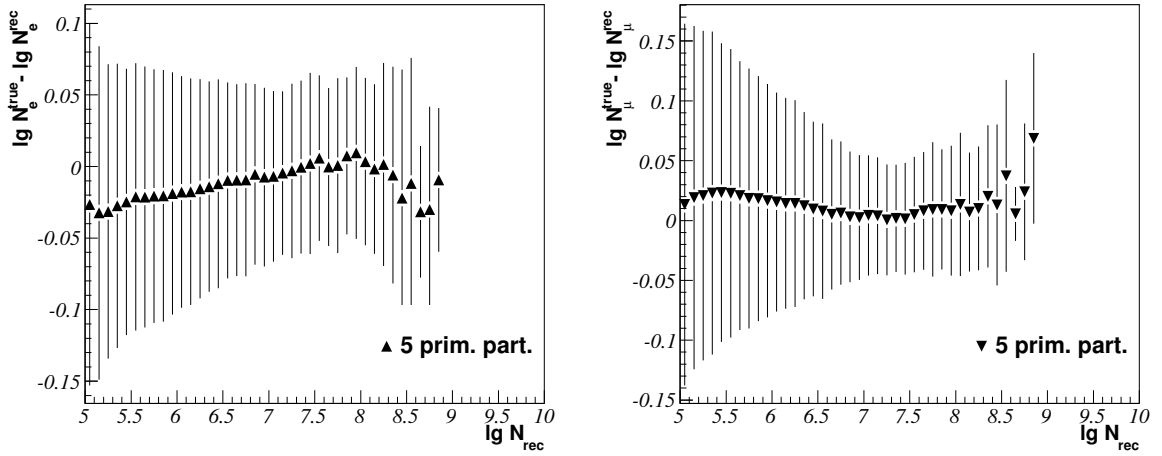


Figure 4.7: In both pictures the error bars represent the spread of the distributions, markers represent bias. Simulated data are contained from 0 to 40° zenith angle for a composition consisting of 5 primary particles in equal proportions. Left: Resolution of electron number. Right: Muon number resolution.

to reconstructed electron number. For higher reconstructed electron numbers than  $10^6$  almost no systematic shift is visible. The mean resolution in zenith angle equals approximately  $0.5^\circ$ .

In the left part of Figure 4.7 the logarithmic electron number resolution is depicted. The logarithmic electron number's resolution equals 0.07 for events above the detector threshold. At the beginning of the electron number range an overestimation of 0.02 in  $\lg N_e$  can be seen. This overestimation almost vanishes with increasing electron number. The right part of Figure 4.7 shows the resolution in muon number. Depicted is the difference of true and reconstructed number of muons. The average resolution of logarithmic muon number equals approximately 0.06 and a slight underestimation of 0.01 can be stated.

In Figure 4.8 the relative electron number uncertainty subject to the true number of electrons is depicted for a mixture of 5 primary particles. The graph shows the mean values for shower simulations up to  $40^\circ$  inclination. To the simulated dataset used the same quality cuts as for data (see Section 4.4) have been applied. It can be seen that with the reconstruction procedure used a very precise knowledge of the number of electrons is achieved. Just for extreme values of electron number the uncertainty is bigger than 2%. At the beginning of the showed range this is caused by the still rising efficiency of the detector with increasing number of particles and accordingly energy.

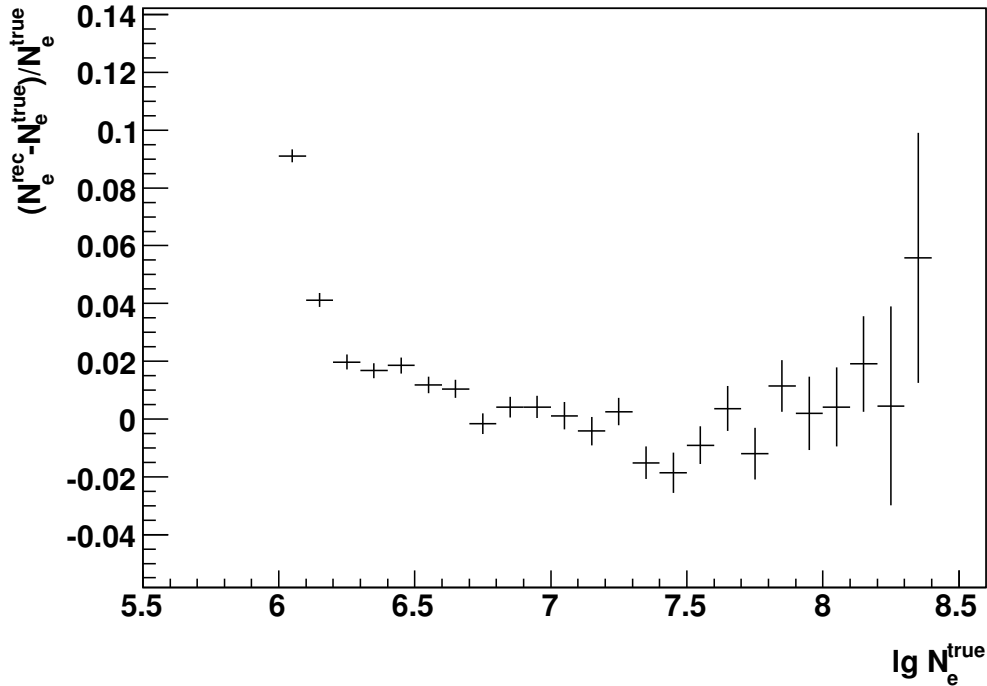


Figure 4.8: Reconstruction uncertainties in electron size subject to true electron size. Marker represent mean values; error bars depict the statistical error on the mean value.

At the end of the range the statistics is just too small for reliable statements.

## 4.4 Data Sample

For the analysis described in this work data from the KASCADE-Grande experiment of the time period from 2003-12-20 up to 2011-02-22 are used, corresponding to a time period of 2622 days. The here described data are used in this as well as the next two chapters. In Figure 4.9 the time differences of every subsequent two events are histogrammed. This plot is the starting point for the determination of the measurement time. Therein are all events included neglecting any cut for quality. The only prerequisite the events have to fulfill is that the detector had to be in a status with all the 18 trigger clusters (or trigger hexagons, videte Section 3.1) flagged as active. The range starts at 0 seconds and continues to two minutes which is adequate for containing all events registered by the detector. Having a mean event rate of roughly 4 Hz an average time difference of 0.25 s can be expected. In Figure 4.9 it can be seen that the tail of the distribution starts already at approximately 30 s. Thus events with a time

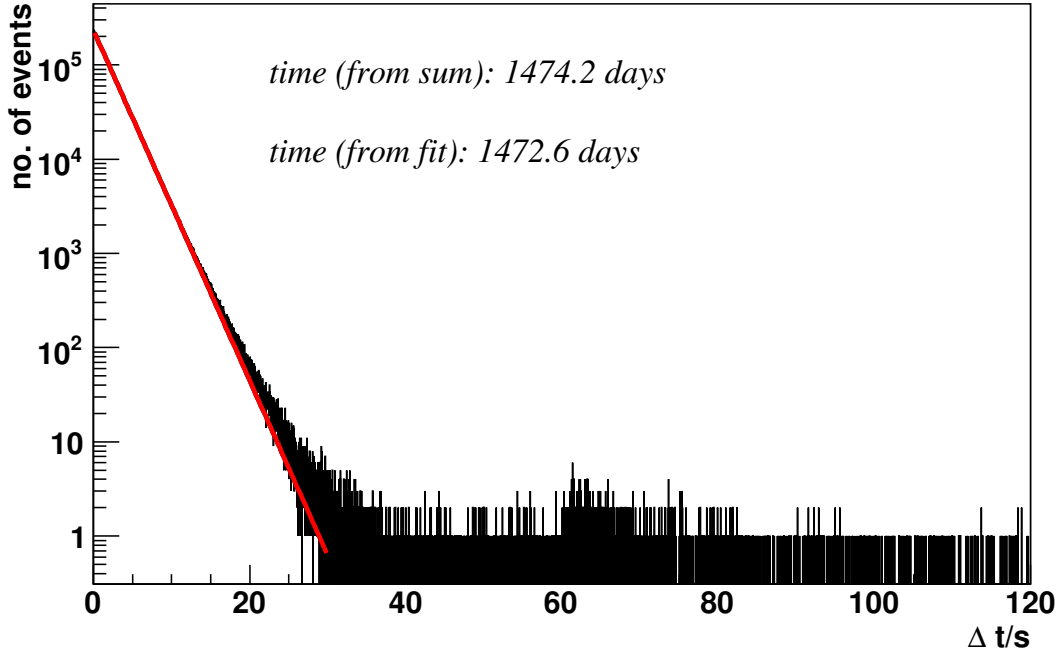


Figure 4.9: The time differences of each two subsequent events for the whole data set used in the analysis.

difference of more than 30 s are really rare in the data set.

Two methods lead to the total time in which the experiment measured every air shower event. The first order approximation is just summing up all the time differences to infer the total time  $T_{sum}$ . This natural way of summing up all existing time differences leads to a total measurement time of 1474 days. A more sophisticated way is the adjustment of an exponential function to data. In the exponent of the function one parameter is the total time of measurement. In the following the assumed correlation function which describes the frequency of the different time values:

$$N(t) = N_0 \cdot e^{-\lambda t}. \quad (4.3)$$

For the determination of the overall measurement time  $T_{fit}$  Equation 4.3 has to be multiplied by time  $t$  and afterwards integrated from zero to infinity which delivers:

$$T_{fit} = \frac{N_0}{\Delta x} \cdot \frac{1}{\lambda^2},$$

where  $\Delta x$  stands for the chosen bin width in Figure 4.9. The application of the described procedure gives a measurement time  $T_{fit}$  of 1473 days. Both methods give

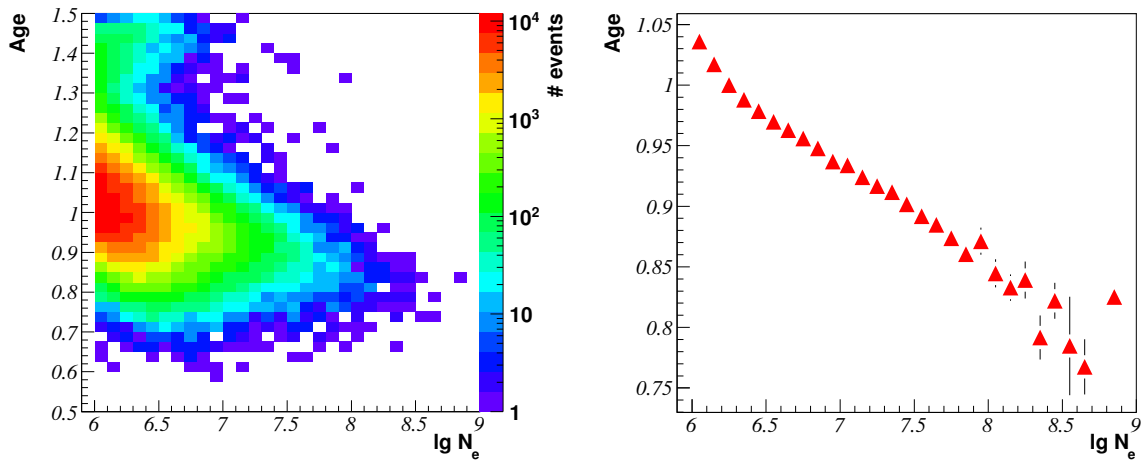


Figure 4.10: In both pictures the error bars represent the statistical errors and the underlying data are real and stem from measured air shower events up to an inclination of  $40^\circ$ . Left: The two-dimensional distribution of age versus electron size. Right: The mean age values subject to electron size.

compatible results. In the analysis for the flux normalization the value from the fit procedure is used. With a measurement time of 1473 days the mean duty cycle of the detector lies at 56 %. This ratio is caused by different time periods in which the detector did not work properly. During maintenance work, like the exchange of broken photomultipliers, the detector was not active. When parts of the detector fail during a measurement period the recorded data are not used for the analysis. A small fraction stems from the inactive time during the procedure of stopping and restarting the apparatus when the usual shift work is done twice a week. In addition the requirement of activeness of all stations (all trigger hexagons have to be active) reduces the active time. Once a year the calibration of the photomultipliers is done. During this time period of four weeks at least one Grande station does not measure. Often high voltage problems cause some photomultipliers in one station not to work properly. All these different reasons lead to the mentioned duty cycle.

In order to guarantee a perfectly well working detector different quality cuts are applied. The following criteria have to be fulfilled by every event in this analysis:

- fiducial area cut (shown in Figure 4.11)
- anka cut (comparison with a quality data bank to avoid events induced by the synchrotron radiation source ANKA on site of the detector)

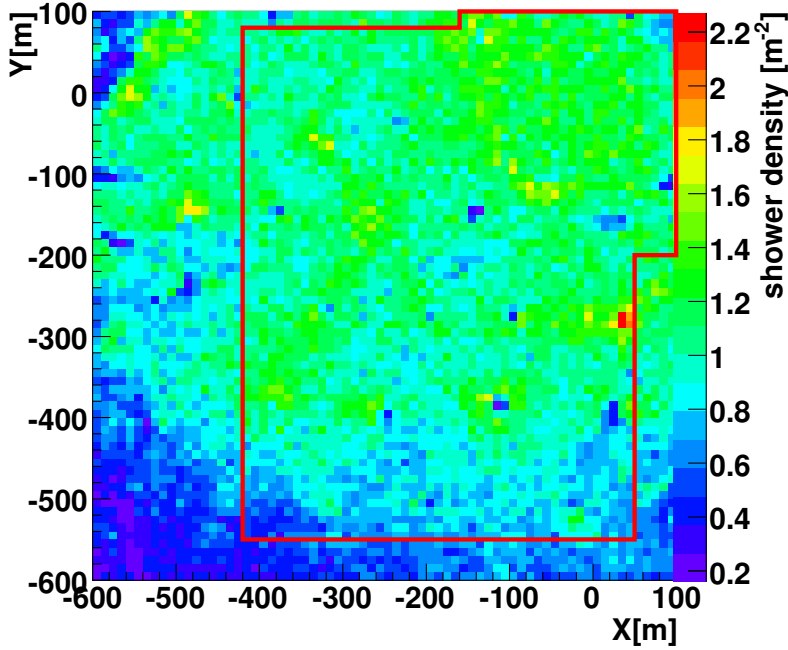


Figure 4.11: The mean shower density for the data sample underlying the analysis is shown. The red marked area denotes the fiducial area used in the analysis.

- all trigger hexagons have to be in an active status
- sevenfold trigger hexagon (only events which were triggered by a cluster which had in all seven stations an energy deposit)
- age cut ( $0.4 < Age < 1.4$ )
- size cut on level 1 ( $\lg N_{ch}^{level1} > \lg N_{ch}^{level3} - 0.5$ )

In Figure 4.10 the age value is depicted as a function of electron size. The reconstructed age or shape parameter  $s$  is a kind of measure for the shape of the lateral density function. Therefore it can give direct hints of problems in the NKG function adjustment. But for the here presented data no bad features can be identified. Although the literal meaning of the age is mostly vanished in Figure 4.10 (right part) the general behaviour can be recognized that the higher the size and the energy of an air shower the "younger" (smaller age value) it is.

In Figure 4.11 the mean shower density for the data sample is depicted, i. e. the number of events per area. For filling the two-dimensional histogram the shower core is taken as position information. Inside the area used for the analysis it mainly varies from  $0.8 \cdot \frac{1}{m^2}$  up to  $1.4 \cdot \frac{1}{m^2}$  which leads to a very low spread. The red line marks the fiducial area which contains the 510909 events used for the analysis. The overall distribution looks very homogenous and smooth in the whole fiducial area which is marked by the

red line. The special shape of the area is caused by the addition of the KASCADE area to the Grande one. Both areas themselves have a quadratic shape and the fusion of them results in the shown polygon.



# Chapter 5

## Constant Intensity Cut Method

One of the first descriptions of the main idea followed in this chapter can be found in the proceedings of the 8<sup>th</sup> International Cosmic Ray Conference in Jaipur in the year 1963 by Clark, Bradt and La Pointe [Cla63]. In this paper they are describing for the first time the idea how to correct air shower data stemming from different zenith angle directions for the attenuation suffered in the atmosphere. The main and crucial prerequisite for the application of the method of constant intensities is the total isotropy of cosmic rays, i. e. that the arrival directions of the incoming particles are total homogeneously distributed and no special direction with a varying flux can be distinguished. According to the current scientific knowledge this assumption holds in the considered energy range from  $10^{16}$ - $10^{18}$ eV. Special analyses of KASCADE-Grande data have confirmed the total isotropy of cosmic rays in the aforementioned energy range (vide [Ove07]). Just for the highest energies of cosmic rays certain anisotropies are detected (confer [Abr07]) and for the latter a more recent analysis has shown a weakening of the correlation of the arrival directions of ultra-high-energy cosmic rays and nearby extragalactic matter (see [Abr10a]). On basis of the total isotropy in the considered energy interval the registered flux values in different angular ranges can directly be related to one primary energy. The very steep energy spectrum of cosmic rays delivers a direct correlation between flux and energy, as a consequence one constant flux for different inclinations is stemming from the same primary energy and just the attenuation in the atmosphere causes the detection at different observable values for different zenith angles.

### 5.1 Zenith Angle Classification

The zenith angle of the incoming shower is besides the shower size one very important variable for this analysis. The zenith angle is the angle between the direction of the incoming particle and the normal direction of the observation plane.

In KASCADE-Grande events in the angular range from 0-40° can be registered with full efficiency almost over the whole measurement range in energy. In order to perform

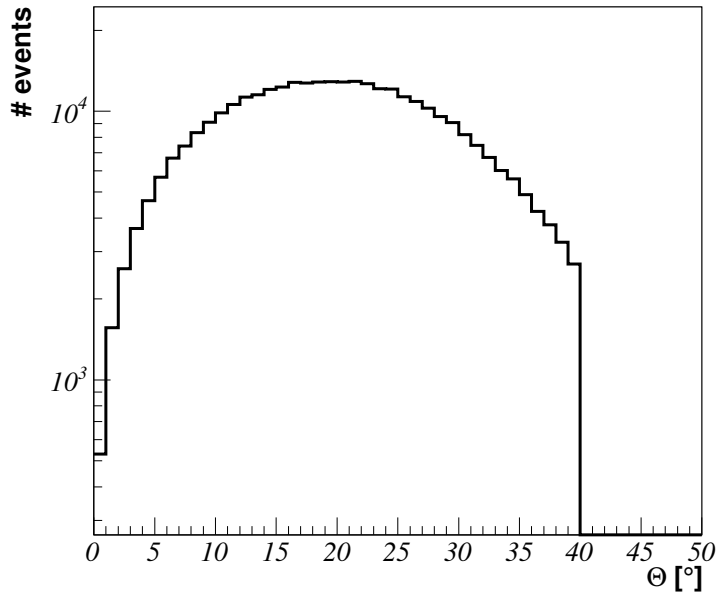


Figure 5.1: Distribution of zenith angles for all measured events which passed the quality criteria.

the method of constant intensities the detected events have to be classified in certain angle intervals (angle bins). On the one hand a high number of intervals increases the statistics in the determination of the attenuation, on the other hand the smaller the intervals the less the statistics in one bin. So, five angular ranges up to a zenith angle of  $40^\circ$  have found to be a good compromise. For the CIC method it is very helpful to have the same number of events in one interval, that leads to the constraint of same exposure for every angular interval. As the measurement time for the different angle bins is the same and the former is the only difference between exposure and acceptance five angular intervals with same acceptance have been chosen. The acceptance in one interval equals  $2\pi \cdot \int_{\Theta_i}^{\Theta_f} \sin \Theta \cos \Theta d\Theta = 0.260$ . In table 4.1 the resulting ranges are listed.

In Figure 5.1 the distribution of zenith angles for all events used in the analysis is shown. The increasing distribution at the beginning can be explained by the increase of solid angle of a conical shell when starting at 0, i.e. vertical impinging events. With growing zenith angle the effect of the diminishing effective detector area becomes dominant. At an angle of approximately  $21^\circ$  the distribution has its maximum.

## 5.2 Electron Number Spectra

The first step and the basis of the analysis are the determination of the differential electron number spectra. In Figure 5.2 the differential  $N_e$  spectra for the KASCADE-Grande data measured are shown. For more information on the data sample used see Section 4.4. In this section also the applied cuts for the determination of the data sample are described.

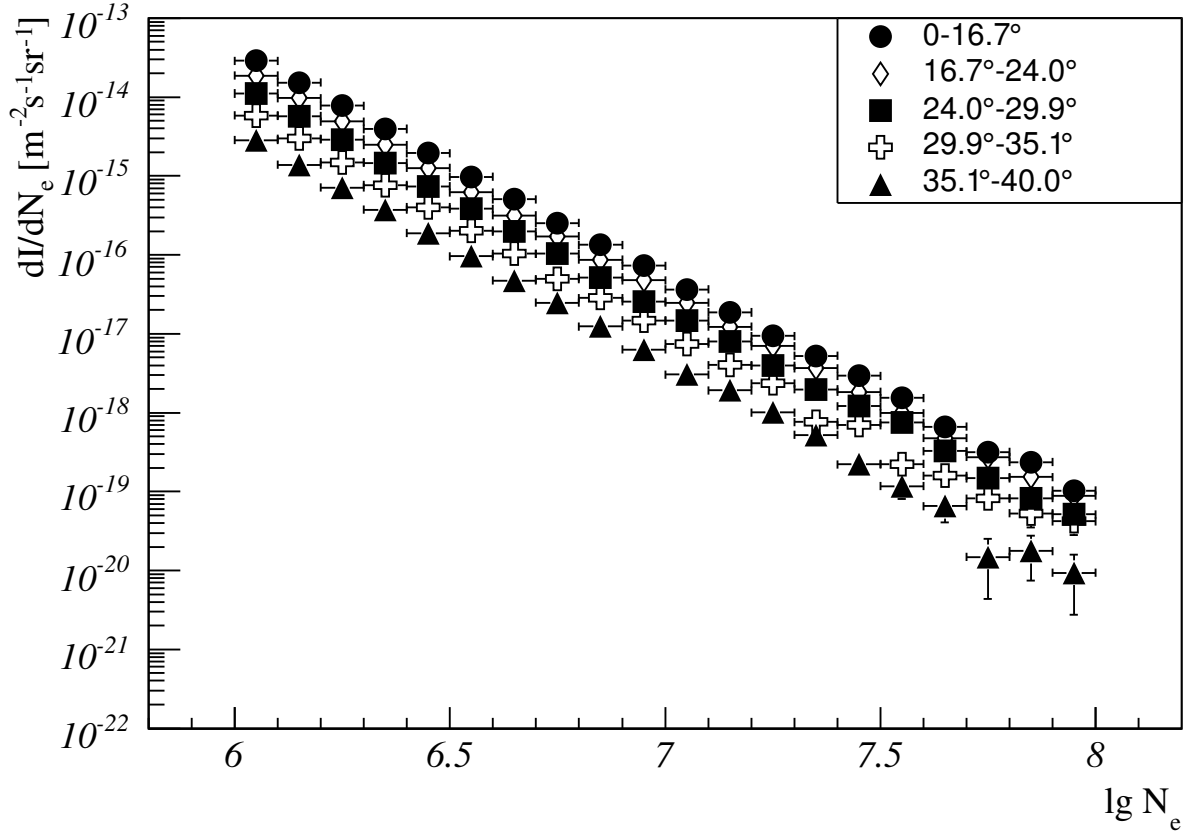


Figure 5.2: The KASCADE-Grande differential electron number spectra for different angle ranges. Plotted is the logarithmic differential cosmic ray flux subject to logarithmic electron number.

These graphs give detailed information on how many events can be detected in an interval of electron number per area per time and per solid angle for the different angle intervals. Shown in the depiction is the differential flux per area, solid angle and time as a function of the logarithmic electron number for five different angular ranges. It can be seen that the flux for one distinct range in electron number decreases with increasing zenith angle, this is just due to the higher amount of slant depth more inclined showers have to travel through, in other words the attenuation. The spectra from different angles all exhibit a perfect power law behavior without any significant features like an index change.

The next step in the analysis chain is the determination of the integrated spectra (confer Figure 5.3). Here subject to electron number the integrated flux is depicted, i. e. the flux for showers with an electron number higher than the function value. The points of the different graphs are connected with spline objects and so it is possible to determine an electron number value for every arbitrary value of integrated flux. Since the energy spectrum of cosmic rays is a steeply falling power law function a natural connection

between flux and energy is given, i. e. a certain flux value corresponds directly to one distinct energy value. So the fact that there are different integrated electron number spectra for different angular ranges solely inherits from the attenuation of the electron component in the atmosphere. To quantify the attenuation different evenly distributed constant flux values are chosen and for every flux value the corresponding size values stemming from different inclination ranges can be inferred.

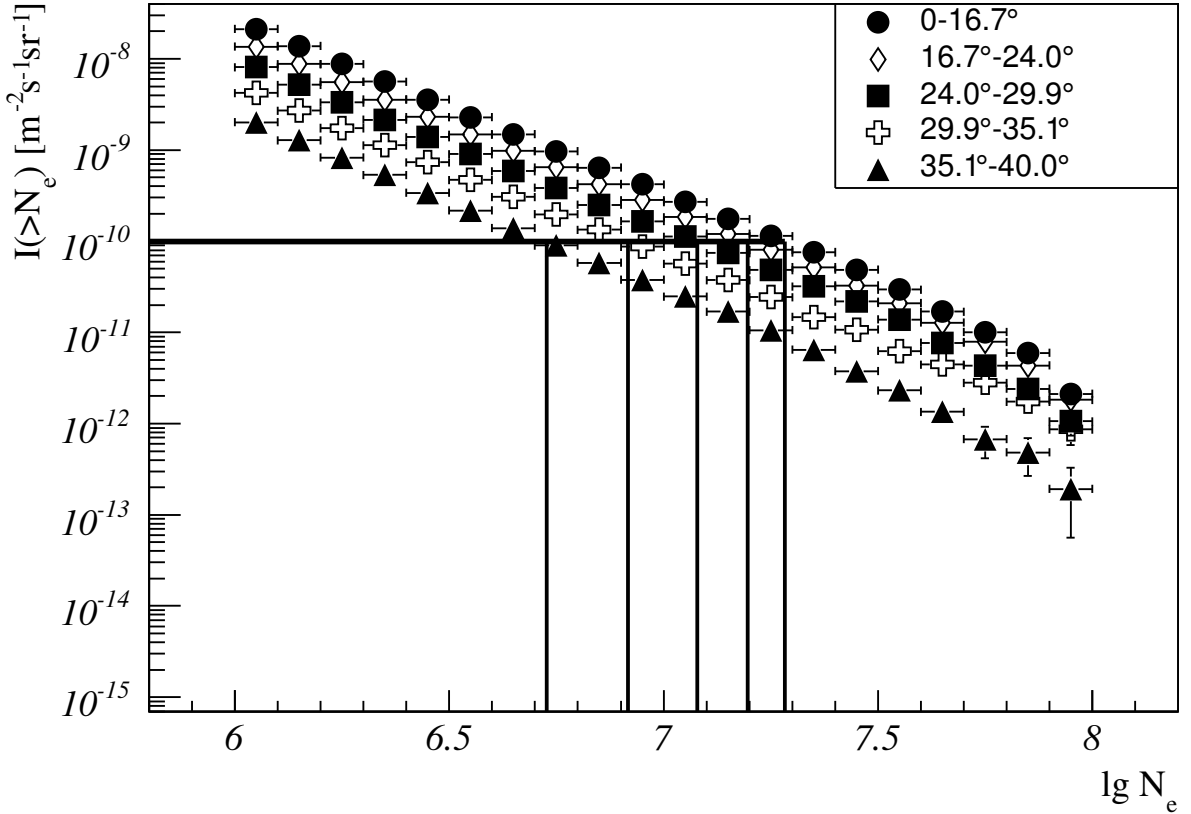


Figure 5.3: The integrated electron number spectra.

In Figure 5.4 the electron number as a function of the angular parameter  $\xi$  is depicted.  $\xi$  is chosen in a way to vanish at the most abundant angle and the quadratic trigonometric function is used to be directly proportional to the solid angle:

$$\xi = \cos^2 \Theta - \cos^2 21^\circ.$$

The zenith angle intervals are chosen with the same acceptance in each one, thus in the  $N_e(\xi)$  distribution (Figure 5.4) the data points have a uniform mutual distance because the  $\xi$ -variable is proportional to the solid angle. This fact eases the determination of the correct function which describes the attenuation. As the result of two counter playing effects the reference angle of  $21^\circ$  is the most frequently occurring inclination for all events. On the one hand with increasing zenith angle the circumscribed solid

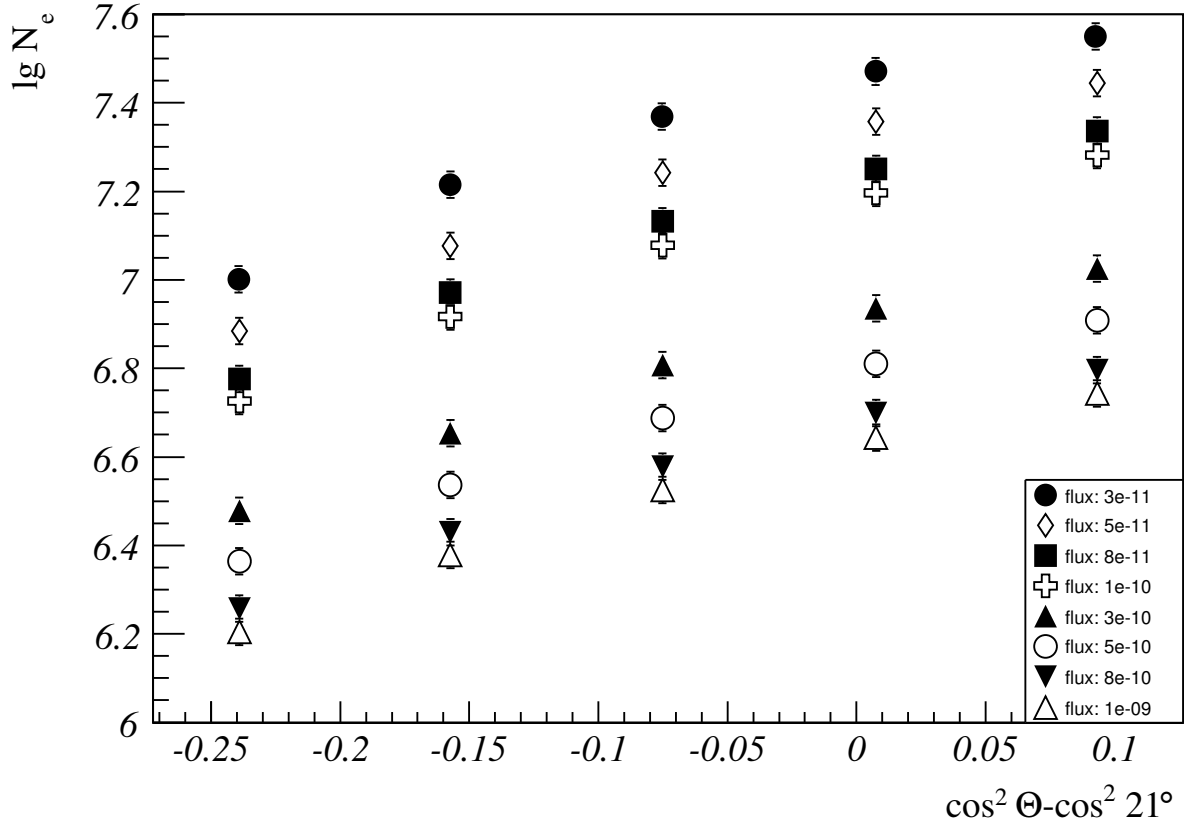


Figure 5.4: The attenuation values from data. Shown is the logarithmic electron number subject to the angle variable  $\xi$ .

angle of the cone which contains all the possible azimuth angles for a given zenith angle becomes bigger. On the other hand, the higher the zenith angle the smaller is the effective detector area seen by a virtual observer under this angle ( $A_{\text{eff}} = A \cdot \cos \Theta$ ). For eight evenly distributed flux values the value pairs  $(\xi, \lg N_e)$  can directly be taken from the integrated spectra. For interpolation purposes splines are used. In order to determine the attenuation the first step is a fit of a second order polynomial on every attenuation curve, in this way the corrected electron number  $\lg N_e^{21^\circ}$  for every attenuation curve can be calculated. The function applied has the following form:

$$\lg N_e = f(\xi, I) \quad (5.1)$$

$$= \lg N_e^{21^\circ}(I) \left(1 + p_0 \xi + p_1 \xi^2\right), \quad (5.2)$$

where  $I$  denotes the corresponding integrated flux value taken from Figure 5.3.

The corrected electron number is somehow universal concerning the zenith angle. It is the electron number an extensive air shower would have if it did arrive under a zenith angle of  $21^\circ$ . With the corrected electron number corresponding to all the different flux

values it is possible to perform a global fitting procedure which takes into account the curvature of all eight functions at once. With the help of a chi-square-minimisation eight functions corresponding to Equation 5.2 are adopted to the data points in Figure 5.4 at once and each single function describes one certain integrated flux value. The following term describes the object to be minimised:

$$\chi^2 = \sum_I \frac{(\lg N_e - f(\xi, I))^2}{(\sigma_{\lg N_e})^2 + \left(\frac{\partial f}{\partial \xi} \cdot \sigma_\xi\right)^2}, \quad (5.3)$$

which comprises all the datapoints in Figure 5.4.  $\sigma_{\lg N_e}$  and  $\sigma_\xi$  describe the errors of the mean values in the  $\lg N_e$ - $\xi$ -plane. The applied „global“ fitting procedure takes directly into account in one step the dependence of the electron number value from  $\xi$  and  $I$ . The minimisation procedure takes not only the uncertainty of the electron number into account, but also the one of the angle variable  $\xi$ . The distance of the error ellipses to the quadratic functions is decreased to the minimal value [Blo98]. The actual minimisation is done by the minuit program package <sup>†</sup> [Jam75]. The adjusted functions are depicted in Figure 5.5, where a direct comparison of the global functions with the adapted single curves is given. In the global fitting procedure a  $\chi^2$ -value of 0.4 p.d.o.f. is achieved. Just for the extreme integrated flux values there are differences between the two functions visible. The procedure applied delivers similar results as if one had taken one single curve with a medial integrated flux value. Table 5.1 gives the global parameter values of the second order polynomial fit. Due to the fact of similarity of the individual single curve fit functions in the considered flux range the composition does not change drastically. The latter is an important prerequisite for the application of a global fit procedure.

par.	value	error
$p_0$	0.1859	0.0104
$p_1$	- 0.3493	0.0514

Table 5.1: The values of the second order polynomial adjustment procedure depicted in Figure 5.5.

With the help of the parameters determined in the former section it is possible to calculate a corrected electron number  $\lg N_e^{21^\circ}$  for every single event. In Figure 5.6 the resulting electron number spectra are depicted. The black graphs show the spectra for every single angular range. It is obvious that they resemble perfect power laws with a compatible overlapping inside the statistical uncertainties. Therefore no drastic index change of the all particle energy spectrum can be expected. The only imag-

<sup>†</sup>contained in the ROOT function TMinuit

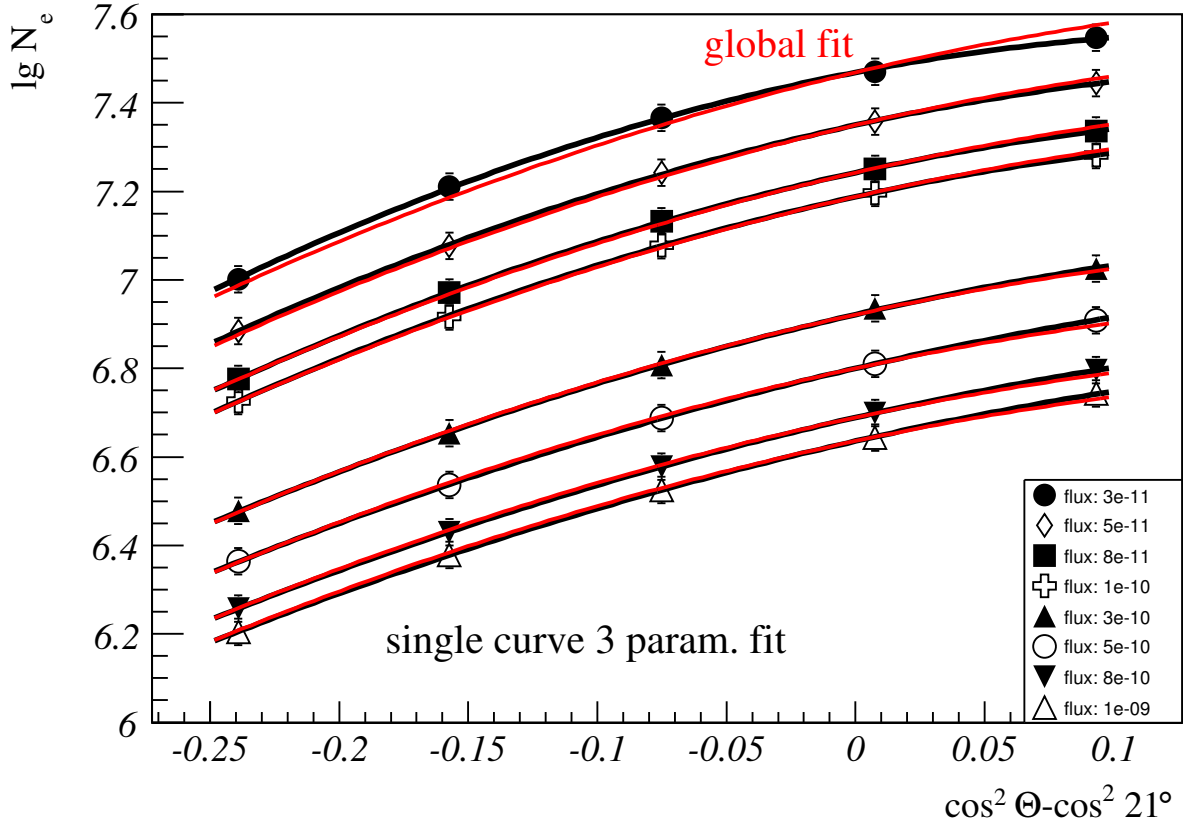


Figure 5.5: The used fit functions for the description of the attenuation.

inable scenario which is compatible with the electron number spectra would be the manifestation of index changes in the spectra of different mass groups which cancel out each other in the all particle spectrum. Or different indexes for the single mass spectra are also possible. Nevertheless one has to keep in mind that the binning in electron number itself introduces a certain bias. In every individual electron number bin a mixture of different elements is contained and one bin corresponds to a certain energy range for hydrogen-like primary particles. However the corresponding energy range for iron-like primary particles is higher and therefore, due to the steep spectrum, light elements dominate the electron number spectrum. So the muon number spectra are more sensitive concerning special features of the iron-like component because in bins of muon number the opposite behavior rules and so the iron-like component is dominating the course of the spectra. Up to a logarithmic electron number of about 6.5 a shift of the detector threshold can be seen for the highest inclinations. This feature just evolves because of the lack of events below the detector threshold which is shifted by the method to a higher electron number. Therefore the threshold of the method lies at 6.5 in logarithmic electron number, at least for inclinations higher than  $24^\circ$ . In the first five electron number bins the overall size spectrum is built by events

coming just from the lower angular bins in which the full efficiency can be guaranteed. Remarkable for higher logarithmic electron numbers than 7.5 is the advent of statistical fluctuations due to the small number of events at these high energies. But nevertheless in the overall combined spectrum these fluctuations vanish and a smooth and reliable spectrum up to a logarithmic electron number of 8.5 can be reconstructed.

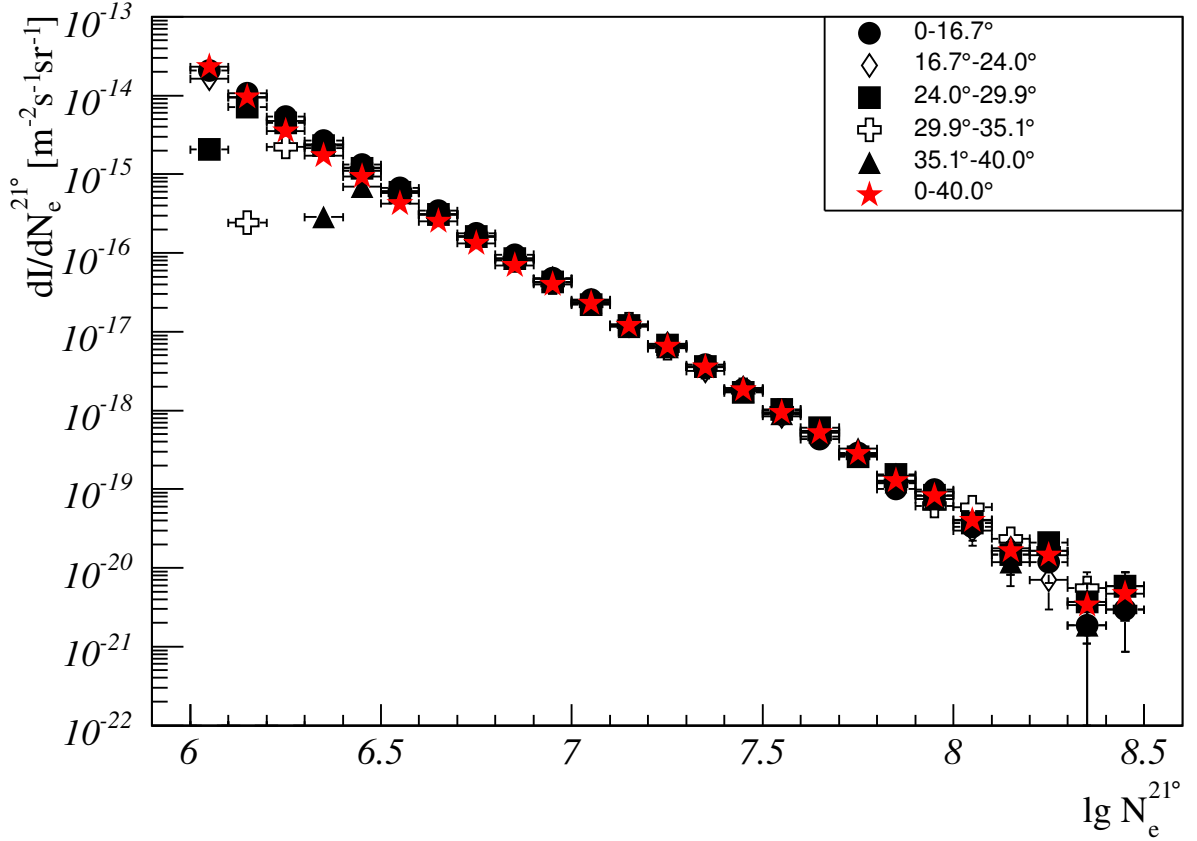


Figure 5.6: The corrected electron number spectra, shown are the results for the different zenith angle ranges as-well as one overall result.

### 5.3 Energy Conversion

The last step in getting the energy spectrum is the determination of a conversion function, i. e. the relation between electron number and energy. The easiest way is using the linear correlation between mean values in simulations. By applying these functions on data it is possible to reconstruct the energy. Two main shortcomings of this method are the dependence on the hadronic interaction model used to perform the Monte-Carlo simulations and the need for choosing a composition in advance for the resulting conversion. The hadronic interaction model mainly influences the description

of attenuation in the simulations. The simulation data used to derive the results shown in this chapter refer to the same sets of simulations as described in chapter 4.

### 5.3.1 QGSjetII

In Figure 5.7 the logarithmic true energy subject to the logarithmic reconstructed electron number is depicted. Shown are the mean values of the distributions in every electron number bin. The error bars represent the statistical errors. The iron curve lies above the values for hydrogen which is expected because at the same primary energy an iron shower starts its evolution in the atmosphere earlier than an hydrogen one. The latter fact leads to a smaller number of electrons which can reach the ground for iron. Or vice versa, an iron shower needs a higher energy for the production of the same number of electrons at detector level than a hydrogen induced air shower. Due to the fact that the reconstructed electron number from Monte Carlo simulations is plotted against the energy, any possible systematic uncertainties subject to energy in the reconstructed size are taken into account. The data's angle range for the conversion is in compliance with the range in which the reference angle lies, i. e. data are taken from  $16.7^\circ$  to  $24.0^\circ$  in zenith.

By applying a first order polynomial fit a direct relation can be inferred respectively for a pure hydrogen and iron composition, as well as for a mixed composition consisting of the five primary particle types Hydrogen, Helium, Carbon, Silicon and Iron in equal proportions. The fit range is chosen in order to keep a certain distance from the detector threshold for low electron numbers, and to avoid running in regions with low statistics for high electron numbers. The fit is performed in an electron number intervall between  $10^6$  and  $10^7.5$ . The fitted functions are depicted in Figure 5.7. The function is of the form:

$$\lg E = p_0 + p_1 \cdot \lg N_e^{rec}.$$

The resulting values for the conversion functions are listed in table 5.2. These functions can then be applied to the corrected electron number of every event and in this way the energy of the primary cosmic ray particle is reconstructed.

### 5.3.2 EPOS

In this subsection the results for the energy conversion functions on basis of the alternative interaction model EPOS are discussed. In the whole analysis chain the only place where the simulation's interaction model play a role is the transition from shower size to energy. Thus in this subsection the energy conversion with the help of simulations based on EPOS is given. For the simulations performed with CORSIKA the low and high energy interaction models employed are FLUKA 2008.3 and EPOS 1.99. The statistics amounts to 1285100 events in total distributed to the usual five primary

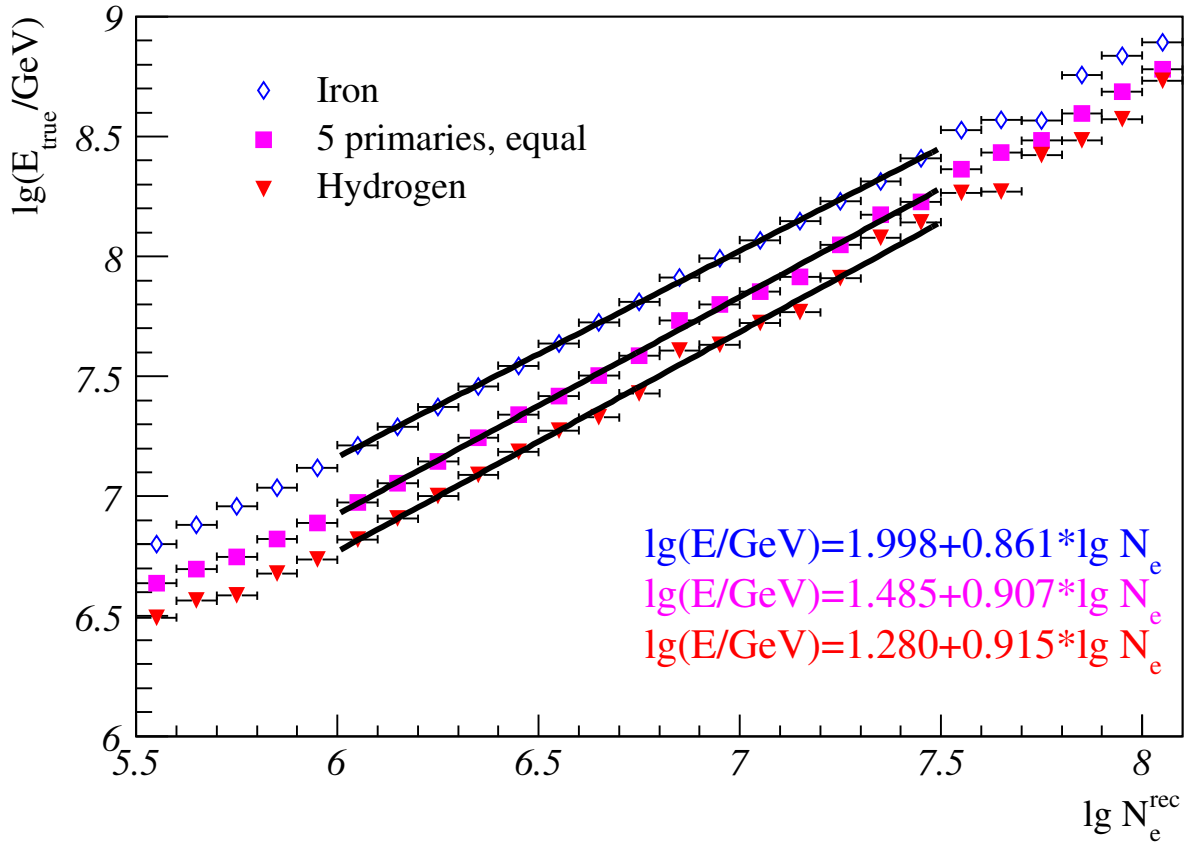


Figure 5.7: The primary particle's true energy subject to reconstructed electron number, depicted for different composition assumptions. The graphs are based on CORSIKA simulations with QGSjetII as high-energy interaction model.

particle types. The energy spectrum of the simulation set is proportional to a  $E^{-2}$  power law. The energy conversion relation for different mixtures of primary particle types is depicted in Figure 5.8. In Table 5.3 the values of the first order polynomial fit are listed. It is obvious that the values for EPOS are in general slightly higher than those for QGSjetII both in the y axis intercept as well as the slope of the energy conversion function. This means that on basis of the EPOS conversion the same shower size is linked with a slightly higher energy. So the eventual energy spectrum is shifted towards higher energies with respect to the QGSjetII spectrum (confer chapter 6). Or alternatively said, for the same energy the measured intensity is shifted to slightly higher values when using the EPOS electron number energy conversion relation.

composition	par. no.	value	error
Hydrogen	0	1.280	0.052
	1	0.915	0.008
Iron	0	1.998	0.027
	1	0.861	0.004
Mixture	0	1.485	0.027
	1	0.907	0.004

Table 5.2: The values of the first order polynomial adjustment procedure depicted in Figure 5.7. The given parameters rely on the QGSjetII simulation sets weighted to a  $E^{-3}$  spectrum.

## 5.4 Sources of Uncertainties

There are various sources for systematic uncertainties in the analysis chain. The different influences are listed below. A depiction of the overall systematic uncertainties

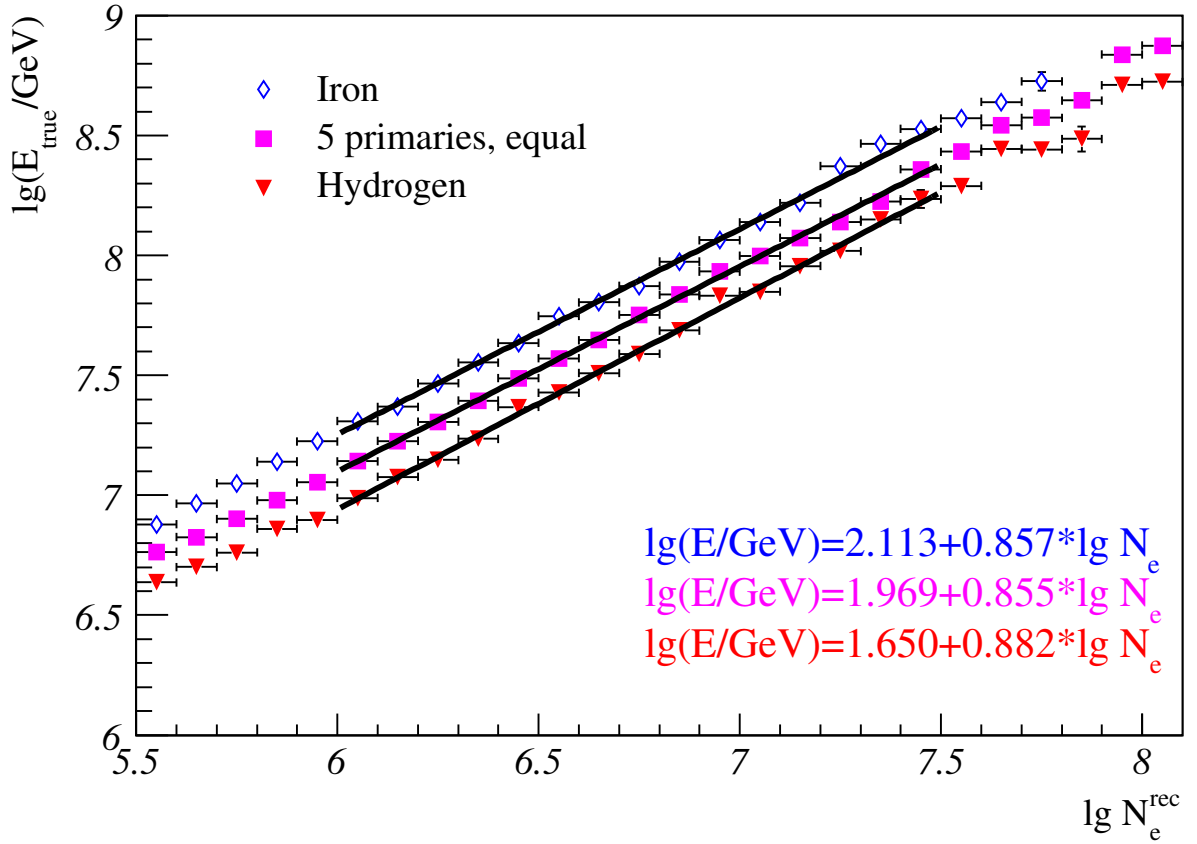


Figure 5.8: The conversion values from simulations with EPOS 1.99 as high-energy interaction model for three different composition assumptions. The error bars describe the statistical uncertainties.

composition	par. no.	value	error
Hydrogen	0	1.650	0.062
	1	0.882	0.009
Iron	0	2.113	0.044
	1	0.857	0.007
Mixture	0	1.969	0.036
	1	0.855	0.006

Table 5.3: The values of the first order polynomial adjustment procedure on the basis of EPOS simulations depicted in Figure 5.8.

can be found in Figure 6.1. In these graph's error bands all the different sources for uncertainties are compiled, i. e. quadratically summed up. In Table 5.4 the individual values for the relative systematic uncertainty at an energy of  $10^{17}$  eV for all the different sources are given.

systematic uncertainty	Hydrogen	Iron
energy conversion fit	1%	1%
attenuation fit	1%	1%
spectral index in MC	17%	4%
attenuation in MC	50%	50%
total	55%	52%

Table 5.4: The values of the systematic uncertainty at an energy of  $10^{17}$  eV for all the different sources.

### 5.4.1 Energy resolution

The intrinsic energy resolution resulting from the method itself is depicted in Figure 5.9. The relative logarithmic energy deviation subject to the true primary particle's energy gives a measure for the precision of the energy reconstruction. As expected the resolution is much worse for hydrogen than for iron which can be explained by the larger shower fluctuations. For hydrogen primary particles the logarithmic energy resolution equals approximately  $\approx 2\%$ . For iron primary particles the resolution is better ( $\approx 1\%$ ). Over the whole energy range the relative logarithmic energy deviation varies from 1 to 2.5 % and results from an energy overestimation which weakens with increasing primary particle's energy. In Figure 5.9 on the right-hand side the energy deviation for a mixed composition is drawn. The resolution equals  $\approx 2\%$ . At the

beginning of the energy range a slight underestimation of  $\approx 1\%$  can be stated. With growing energy the underestimation diminishes. The energy resolution for EPOS as high-energy interaction model is of the same order of magnitude as the one presented in this section.

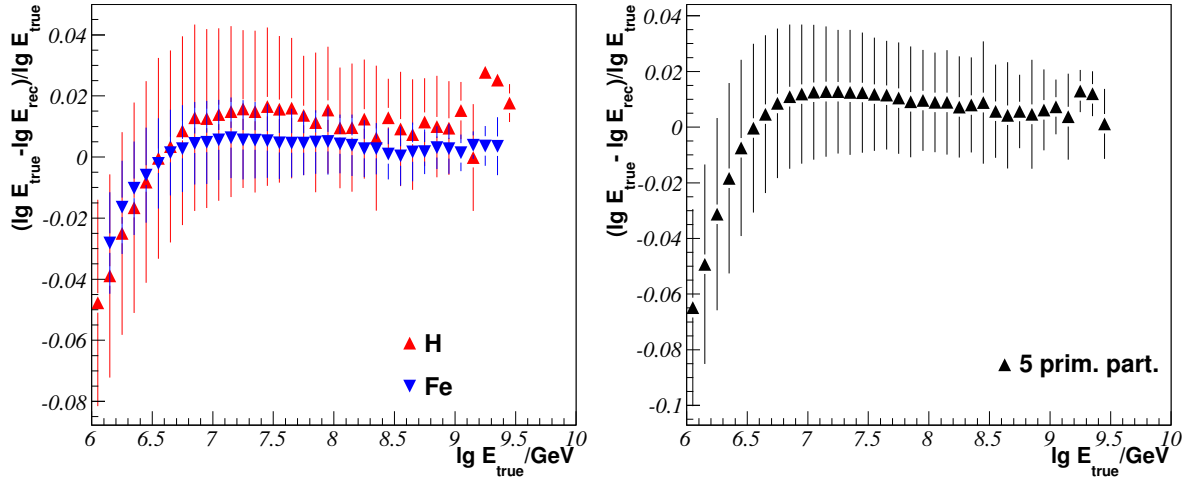


Figure 5.9: Both pictures result from the standard simulations with QGSjetII as interaction model in all angle bins. Depicted is in both cases the logarithmic relative energy deviation subject to the true particle energy. Error bars depict spread of the distributions. Left: For pure hydrogen and iron composition. Right: Mixed composition consisting of five primary particle types in equal proportion.

### 5.4.2 Composition

The assumption of a certain composition for the derivation of the energy conversion formula is the biggest error source of all. The maximal difference in flux can be estimated to 75% (confer Figure 6.2). But this is really the value for the two extreme assumptions of a pure iron or hydrogen data sample which is reconstructed with the wrong conversion formula. In reality there is a mixture of different primary particle types which lowers the influence. Additionally with the Y-cut method the type of particle can be estimated and the corresponding energy conversion formula can be chosen which reduces the influence of the composition assumption as well.

### 5.4.3 Spectrum

A Variation of the spectral index used in the simulations is done for the examination of the spectral index's influence on the reconstructed energy flux. Usually simulations are produced with  $\gamma = 2$  to achieve a reasonable computing time. When using the

simulations for the analysis the spectral index is changed to  $\gamma = 3$  by a weighting procedure with an energy dependent factor. By a variation of the index from  $\gamma = 2.5$  to  $\gamma = 3.5$  the influence of the assumed spectrum's shape can be estimated. This means that in the here presented analysis every value of  $\gamma$  corresponds to one distinct energy conversion formula. The considered range of the spectral index is rather big what results in a robust and conservative estimation of the influence of the spectral shape in the simulations used. The simulated spectrum's slope and with it the appropriate treatment of shower fluctuations is the second largest component of the total systematic uncertainty. The difference in the two spectra for the extreme spectral indexes is included in Figure 6.1.

#### 5.4.4 Interaction model

For the determination of the influence of the interaction model used a direct comparison of the energy conversion functions can be done. In the final energy spectrum there is a certain shift in flux which only refers to the interaction model. In Figure 6.3 the spectra based on QGSjetII and EPOS are depicted. This direct comparison shows that the choice of the high-energy interaction model plays a key role. This uncertainty is not included in the error band shown in Figure 6.1.

#### 5.4.5 Fit errors

In the analysis chain there are two times results of fitting procedures which determine the final result. Both fits introduce an additional systematic uncertainty stemming from the fit's errors. First the relation which describes the attenuation of the electron number introduces a systematic uncertainty. Second the application of the energy conversion function is also defective. Both errors are taken into account in the final energy spectrum. These uncertainties are included by a Gauss error propagation calculation in the depiction of the systematic uncertainties in Figure 6.1.

#### 5.4.6 Attenuation in simulations

The analysis relies on the correct treatment of the electron attenuation in Monte-Carlo simulations. The experimental data are all corrected to a zenith angle of  $21^\circ$ . Therefore for the energy calibration simulations are used distributed around this correction angle. If the simulation's description of the attenuation does not match reality a big uncertainty is introduced. For taking into account the effect in the analysis the correction angle was altered to  $10^\circ$  and to  $30^\circ$ . The difference in the resulting energy spectra for those two cases is contained as uncertainty in Figure 6.1. This part gives the biggest contribution to the overall uncertainty.

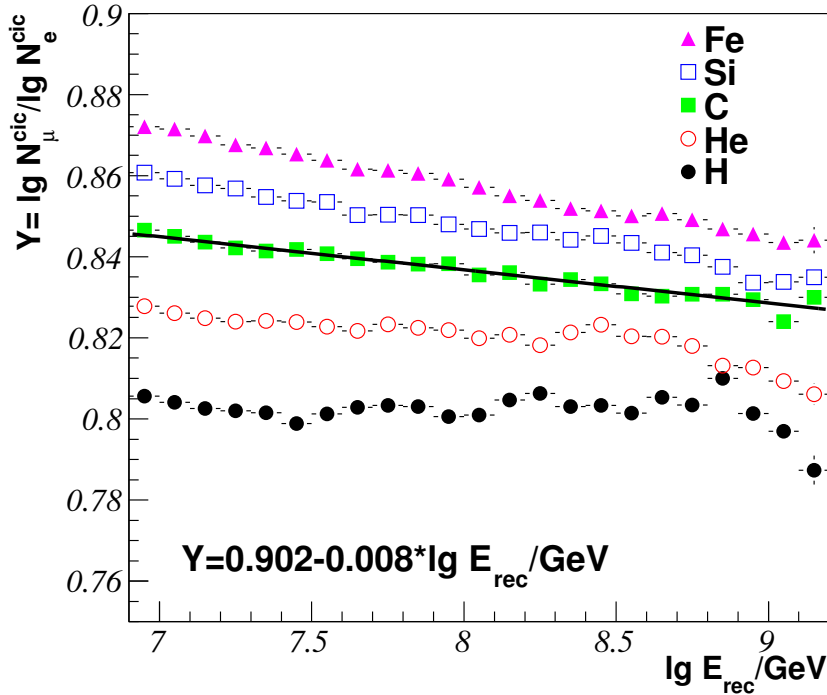


Figure 5.10: Distribution of Y-values for QGSjetII simulations for five different primary particle types. Contained are simulations from 0 to 40° zenith angle.

## 5.5 Composition, Y-Cut Method

So far, in the described analysis the composition is not determined. For the energy conversion there is just one distinct kind of primary particle assumed. But in reality we measure a mixture of different nuclei. For the distinction of the different impinging particle types one has to take into account additional parameters. One possibility for this distinction is the ratio of muon to electron number, which delivers a very natural estimator for the primary particle mass. More detailed descriptions of this method can be found in [Gai78] and [Ant99]. In general, a more light cosmic ray starts its shower development later in the Earth's atmosphere than a heavy one. Thus for a light primary particle the evolution of the electromagnetic component of the particle cascade starts closer to the observation level and therefore it is not as attenuated as for heavy primary particles which start the fragmentation much earlier. In addition, a heavier particle consists of more nucleons and undergoes more hadronic reactions resulting in a higher muon number at ground. To perform this primary particle type distinction in the data analysis the Y value is depicted in Figure 5.10 for the already described standard simulation set with QGSjetII as interaction model and for simulated events with a maximal zenith angle of 40°. In addition to take into account possible attenuation effects the ratio is calculated from the size values which are corrected by a CIC method. The method for the variable electron number is described in detail at the beginning of this chapter. Exactly the same analysis was also performed for the observable muon number. Details of the muon constant intensity cut method can be

found in the Appendix (Figures B.1-B.4). In table 5.5 the final values for the description of the muon number attenuation are given. The given parameters correspond to the same type of correlation as in Equation 5.2 just with the difference of muon number instead of electron number.

par.	value	error
$p_0$	0.0219	0.0115
$p_1$	- 0.1207	0.0567

Table 5.5: The values of the second order polynomial adjustment procedure of the attenuation adjustment for muon number.

For the separation of light from heavy particles a fit to the carbon simulations has been performed. Carbon represents the medium heavy mass group and is therefore the optimal choice for distinguishing between light and heavy. In Figure 5.10 the formula for the straight line fit is contained. It directly gives an energy dependent cut for the identification of the primary particle type. Its application on measured data is explained in Section 6.4. Only for very high energies a higher contamination of the light part with heavier particles is indicated but at these energies the statistics is very low and all energies well above  $10^{18}$  eV are not expected to be detected by the KASCADE-Grande detector.

# Chapter 6

## Energy Spectra

In this Chapter the results of the application on data of the method of constant intensities are shown. The general description of the KASCADE-Grande data set underlying the analysis is given in Section 4.4. Inferred are the all-particle energy spectrum as well as an energy spectrum separately for more heavy-like and light-like primary particles. There is also a distinction given for the most dominating input variable in the Monte Carlo simulations used for the analysis, the high-energy interaction model. In this thesis the energy spectra for QGSjetII as well as EPOS 1.99 are revealed. In the following section the application of the QGSjetII based energy conversion function on the corrected electron size spectrum, means on data, is shown. The energy spectrum evolves on an event by event basis when converting step by step electron size to corrected size and eventually to energy.

### 6.1 QGSjetII

In Figure 6.1 the energy spectrum on basis of the QGSjetII simulations is depicted. The error bands contain all the systematical uncertainties according to Section 5.4. On the ordinate the differential flux value is plotted, i. e. the number of particles per squared meter, second, steradian, and GeV. The abscissa gives the energy in GeV of the primary air shower inducing particle. Due to the fact that the energy spectrum is a very steep power law usually flux is multiplied by a certain power of energy which flattens the spectrum and facilitates the recognition of structures deviating from a single power law. The errorbars in Figure 6.1 represent the statistical uncertainties. For the transition to primary particle energy the correlations given in Table 5.2 are employed. The two different spectra shown correspond to different assumptions of composition in advance. The highest and lowest fluxes relate to a pure iron respectively hydrogen composition concerning the choice of the conversion function. The difference in flux comparing the iron with the hydrogen spectrum is at an energy of  $10^{17}$  eV about 50%. This directly shows the strong composition dependence of the method. As expected the iron spectrum lies above the hydrogen one. This is

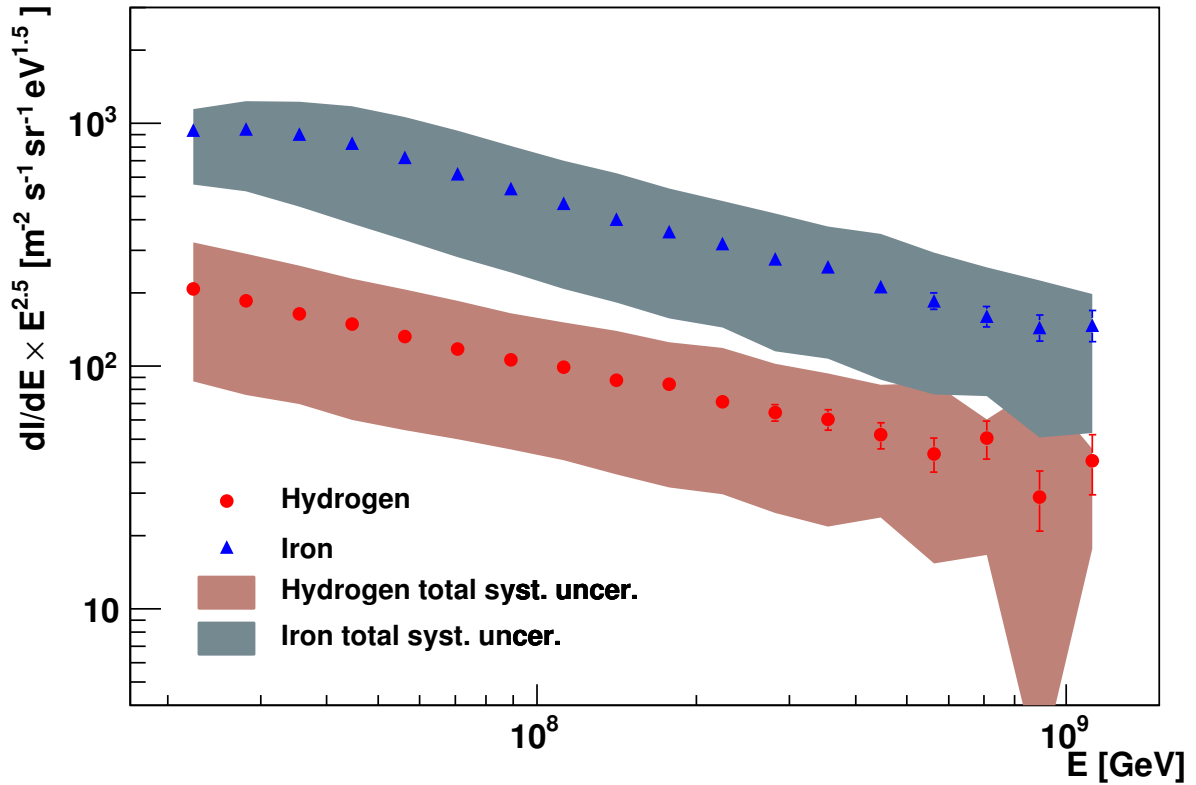


Figure 6.1: Energy spectrum for the QGSjetII conversion function, shown are the extreme composition assumptions. Error bars depict statistical uncertainties, error bands symbolize the systematic uncertainties.

directly caused by the energy conversion function. For a given electron number a higher energy is reconstructed for iron. This directly shifts the iron spectrum towards higher energies and causes also slight threshold effects for the first two data points. Figure 6.2 shows the reconstructed energy spectra for three different composition assumptions together with the results of various cosmic ray experiments. The extreme composition assumptions are not likely to be realistic in the explored energy region according to the current astroparticle physics knowledge. In reality a mixture of light and heavy components with varying ratio is detected. Therefore the third spectrum is the result of a mixture of five elements in equal parts in the simulations for the determination of the conversion function. Its course lies between the hydrogen and iron spectra. The heaviest composition assumption seems to be the most compatible spectrum when comparing with the results of other experiments. But this strongly depends on the observables used for the derivation of the spectrum (compare [Art10]). The latter fact implies a very high fraction of heavy elements throughout the whole energy range. All spectra themselves show a very smooth behaviour, and as can be seen in Figure 6.1 no significant structures can be observed. Just for the highest ener-

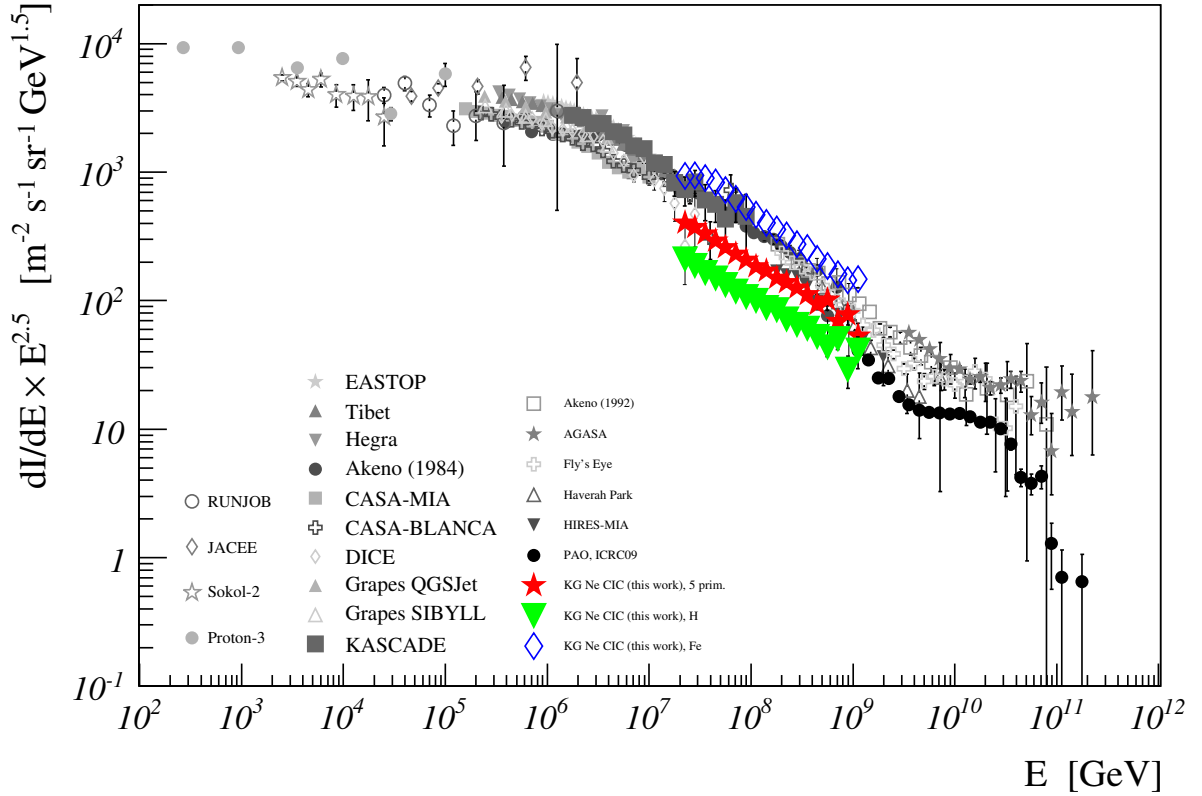


Figure 6.2: Energy spectrum for the QGSjetII conversion function, shown are different composition assumptions. The results from various cosmic ray experiments are also plotted.

gies certain deviations become visible but they are directly caused by the low statistics.

## 6.2 EPOS

In Section 5.3.2 the derivation of the energy conversion function on basis of EPOS simulations is explained. In this section the result of the data analysis with the EPOS function is given. In Figure 6.3 the corresponding energy spectrum is depicted. Shown are two different composition assumptions together with the result for QGSjetII. In general the EPOS result just seems to be shifted towards higher flux values with respect to the QGSjetII result, e.g. at an energy of  $10^{17}$  eV about a factor of 2. This fact can directly be understood when comparing the parameters for the two different energy conversion functions. Interpreting these functions it can be said that the same corrected electron number is connected with a higher energy of the primary particle. Or seen from the point of view of the incoming particle, it can be stated that EPOS produces for a nucleus with a certain energy less electrons than QGSjetII. Neglecting the flux

shift the general course of the spectra is not different from the one for the QGSjetII conversion function and exhibits the same features.

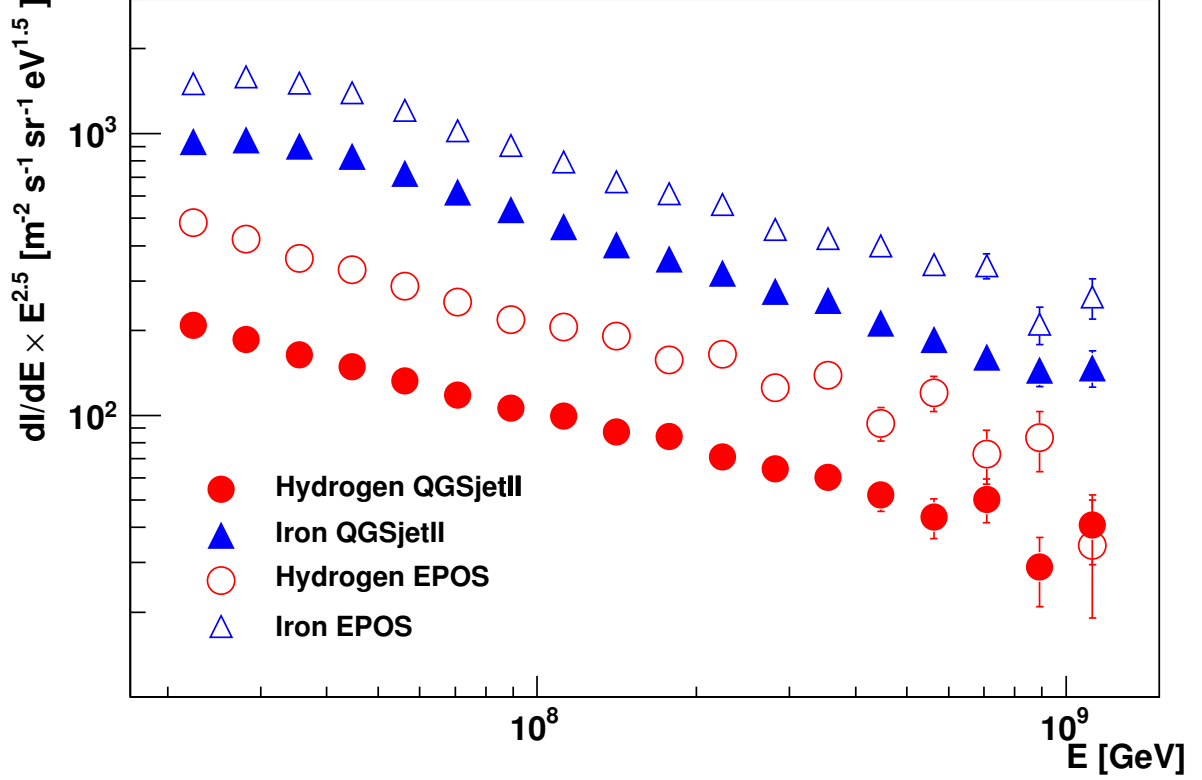


Figure 6.3: Energy spectrum for the EPOS conversion function, shown are different composition assumptions together with the QGSjetII spectra.

### 6.3 Deconvolution

So far, for the determination of the energy spectrum mean values were used. Thus the energy dependent shower fluctuations were smoothed and distributed evenly on the whole energy range. So with the presented methods the investigation of smaller structures in the spectra is not possible. A more sophisticated way to connect the shower size with the primary particle's energy is a deconvolution. By the here presented method the shower fluctuations can be taken into account. The reconstructed flux vector can be thought as the product of a folding of a response matrix with the true energy flux vector. In equation 6.1 the general dependence is written. The  $i^{th}$  component of the  $N_e$  flux vector can be understood as:

$$\sum_j N_e^{rec}(E_{true})_{ij} \cdot E_j = N_{e,i}, \quad (6.1)$$

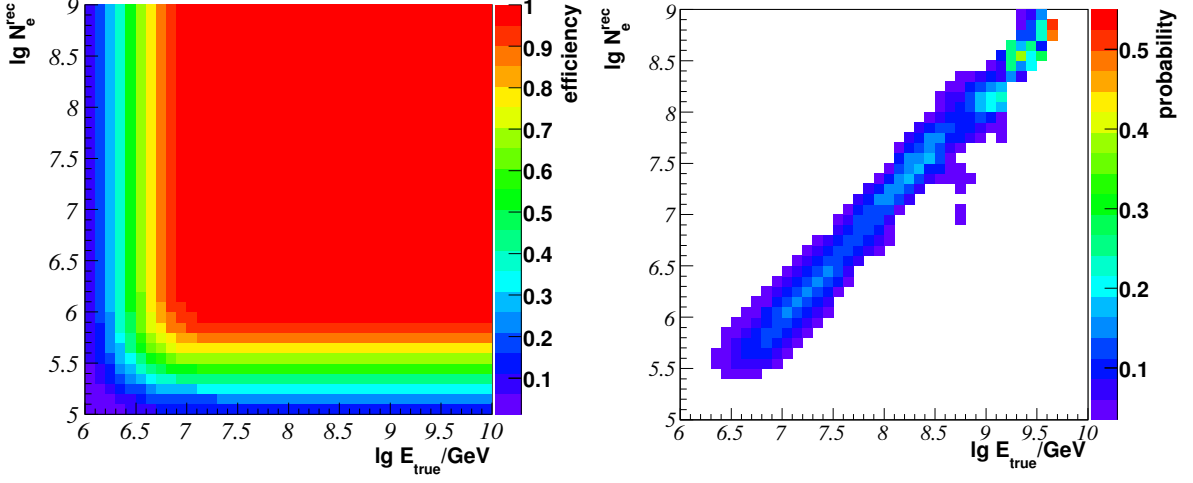


Figure 6.4: Basis are the standard simulation sets with QGSjetII in the second angle bin for hydrogen as primary particle. Left: The two-dimensional fitted efficiency function in the electron size energy plane. Right: The electron size energy conversion matrix.

with  $N_e^{\text{rec}}(E_{\text{true}})$  being the energy size conversion matrix and  $E$  the sought-after true energy flux vector. The only way to determine this response matrix for measured data is the use of extended Monte Carlo simulations. The data shown in Figure 6.4 are based on the standard simulation set. On the left side the two dimensional efficiency function for hydrogen induced air showers is shown. The resolution of the depiction is adopted to the bin width of the energy size relation function. This function directly gives the information beginning from which energies, alternatively electron numbers, the KASCADE-Grande detector works at 100% efficiency. Shown is a two dimensional Gauss error function which is adjusted to the simulated data. Simulations are taken for zenith angles in the angular bin which contains the correction angle for the constant intensity method, i.e.  $16.7^\circ < \Theta < 24.0^\circ$ . On the right side of Figure 6.4 the energy size matrix is shown again for a pure hydrogen composition. The displayed distribution is already improved in order to use it directly as response matrix for the deconvolution. This enhancement means that the whole distribution is smoothed by a Gaussian fit function method and afterwards it is normalized. Normalized in a way that each sum of the probabilities along every column gives 1. By this procedure it is guaranteed keeping in mind Equation 6.1 that the whole flux from every single energy bin of the true energy spectrum is distributed to the individual electron numbers. So the matrix in Figure 6.4 directly mirrors the probabilistic relation between the true energy and reconstructed electron number. In detail, every column gives the probability density function for the different energy bins concerning the conversion from primary particle's energy to a measured electron number on ground. The next step which is already

included in the shown response function is the folding of the efficiency. To take into account the detector's properties the two dimensional efficiency function is forward folded with the smoothed response matrix and the result is shown in Figure 6.4 (right part). For small energies it can be seen that the requirement of the normalization is not fulfilled. That's directly the impact of the efficiency function. The corresponding plots for a pure iron composition and the mixed composition can be found in Appendix C.

So with the help of the described conversion matrix an unfolding procedure can be

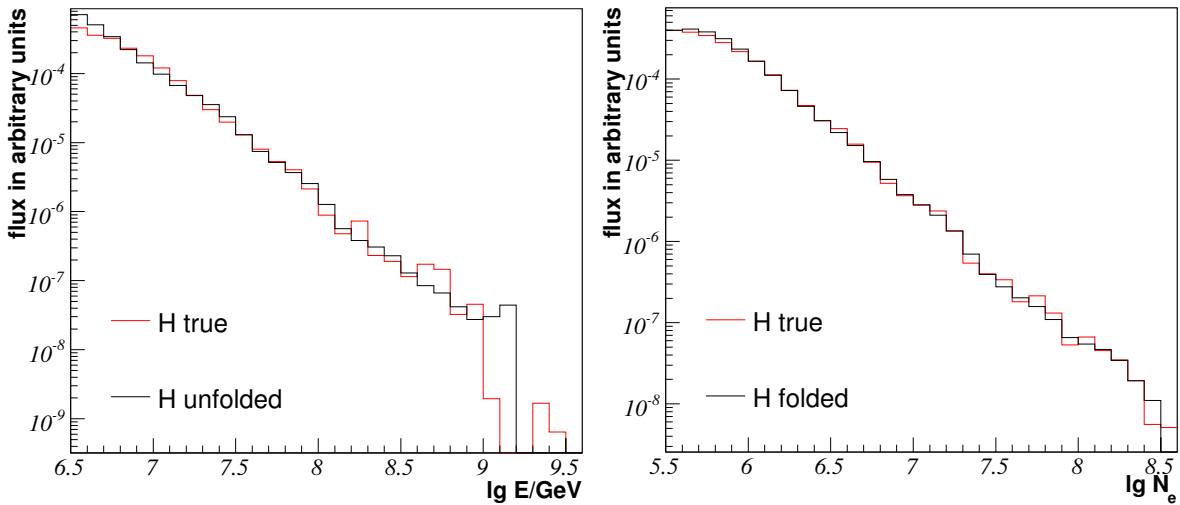


Figure 6.5: Both pictures result from the standard simulations with QGSjetII as interaction model in the second angle bin, only hydrogen induced showers are used. Left: The comparison of true and unfolded energy spectrum. Right: True and forward folded electron size spectra.

performed using the gold algorithm [Gol64]. For the here described method the number of iterations has been determined by reducing the differences between the reconstructed and true spectra for simulations. It lies between 5 and 10 depending on the assumed composition.

In Figure 6.5 the test of the method on simulated spectra can be seen. On the left side the true simulated and unfolded energy spectrum for hydrogen is depicted. In general there is a good compatibility between the two spectra. Just for high energies the differences become bigger which is related to the decreasing statistics. At the beginning of the energy range a slight overestimation of the deconvoluted spectrum can be seen. This could be a hint of some shortcomings in the description of the detector efficiency. In order to cross check the procedure the reconstructed energy spectrum is forward folded with the response matrix. As result an electron number spectrum is obtained. The latter is depicted on the right side of Figure 6.5 together with the original electron

number spectrum which was the basis for the reconstruction procedure. Both spectra agree perfectly well and concerning simulations the whole method works without any deficiencies. The corresponding graphs for an alternate composition assumption can be seen in Appendix C. The next step is the application of this unfolding conversion procedure to the measured and constant intensity corrected electron number spectrum from real data.

Due to the nonlinearity of the deconvolution procedure the reconstruction of measured

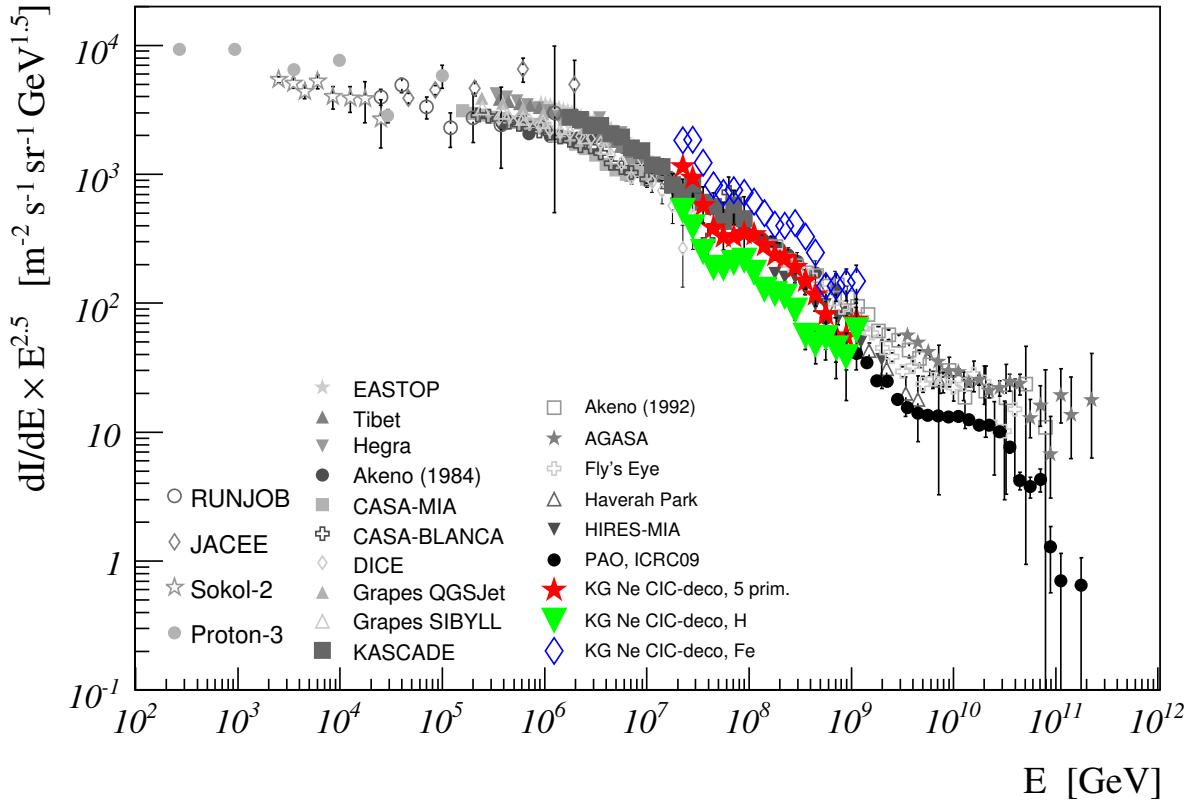


Figure 6.6: Deconvoluted energy spectrum for the QGSjetII response matrices, shown are different composition assumptions, based on data from the second angular bin. Error bars represent statistical uncertainties. The results from various cosmic ray experiments are also plotted.

data is only feasible for a small angular range without severe threshold problems. In this work data from the second angular bin are reconstructed with the described deconvolution procedure in order to guarantee a comparability with the linear energy conversion. In detail the reconstruction can be divided in several steps. The first one is the correction of electron number in the second angle intervall. All these corrected electron numbers build the corrected electron size spectrum for events from  $16.7^\circ$  to  $24.0^\circ$  zenith angle. Afterwards the deconvolution is applied to the raw electron size

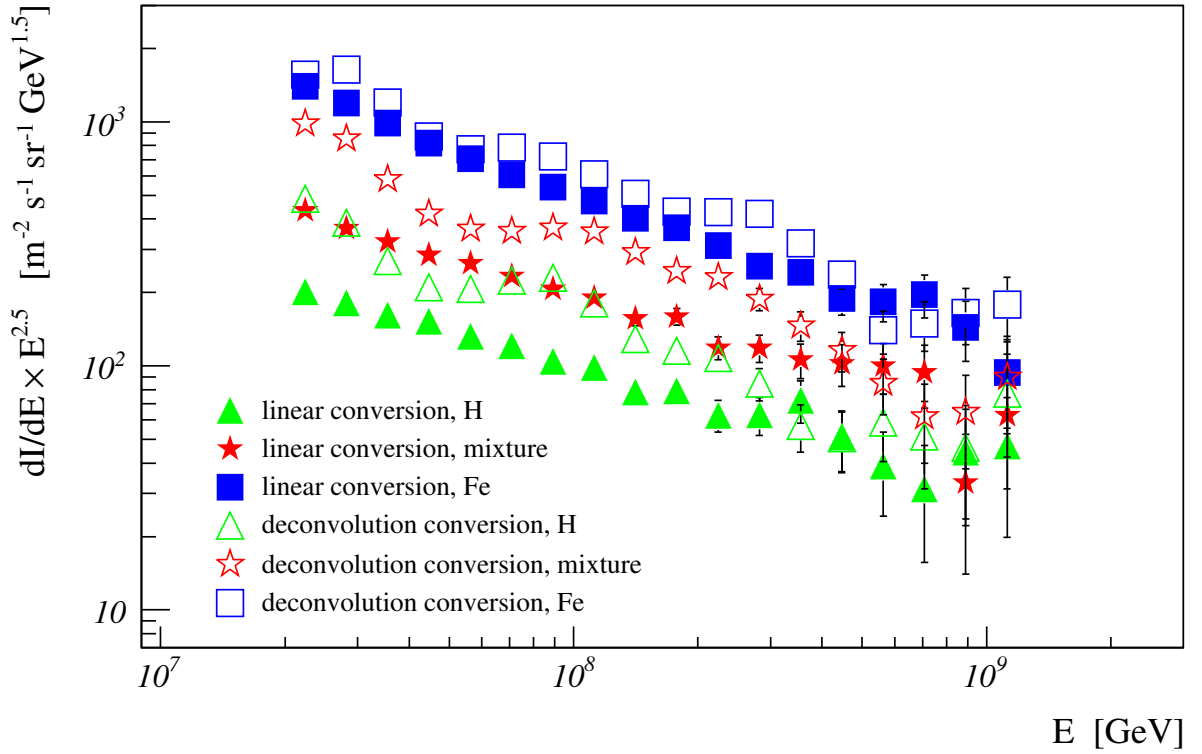


Figure 6.7: Deconvoluted energy spectra for the QGSjetII response matrices in comparison with the spectra for the linear conversion function, both resulting from data of the second angular bin. Error bars represent statistical uncertainties.

spectrum, i. e. the spectrum used is not normalized. With the gold algorithm and the iteration depths stemming from simulations the energy spectra can be reconstructed. Depending on the energy electron number transition matrix (confer Figure 6.4) used spectra for different assumptions of composition are reconstructed. In Figure 6.6 the inferred spectra for hydrogen, iron and a mixture of five elements are shown. By the choice of a certain type of primary particle, every air shower event is reconstructed as if it was the assumed element. So a changing composition in reality introduces an additional uncertainty on the spectrum. However the extreme assumptions shown build the limits for the true spectrum, i. e. the true flux values have to lie in between those values for hydrogen and iron. A remarkable feature of all three spectra is the kink-like structure just before  $10^{17}$  eV. It appears independent of the assumed primary particle type and therefore seems to be a feature of the primary spectrum.

In Figure 6.7 a compilation of the deconvoluted and linearly converted spectra for the second angle interval is shown. The general feature of averaging of the method of linear conversion from electron number to energy is clearly visible. By the method of unfolding the energy dependent shower fluctuations effect the result. The most obvious

feature in all spectra is the structure at around  $10^{17}$  eV which is clearly visible in this depiction. For iron primary particles the shower fluctuations have the weakest effect on the spectrum.

## 6.4 Y-Cut

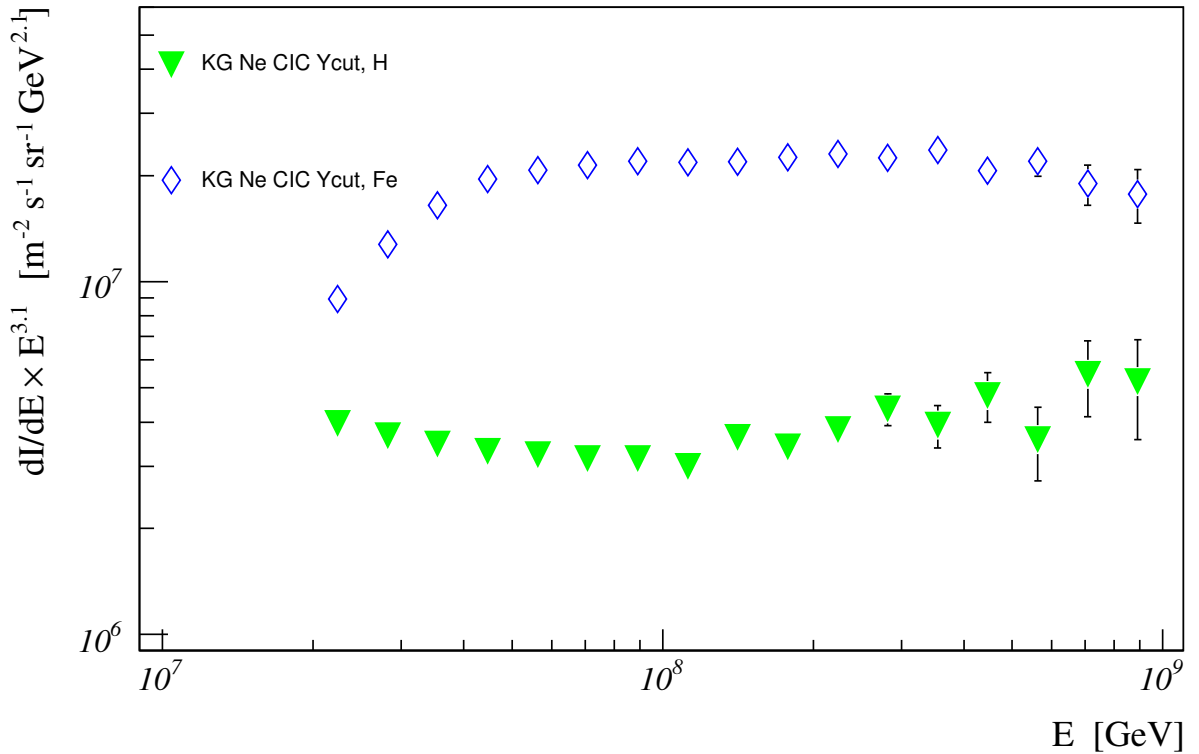


Figure 6.8: Energy spectra for electron-rich and electron-poor data samples, reconstructed with the corresponding energy calibration functions based on QGSjetII simulations.

In Section 5.5 a method is described for the distinction between an electron poor (heavy) and an electron rich (light) component of cosmic rays. The result of this method's application on data can be seen in Figure 6.8. Here the Y-value has been used for the separation of the different mass groups. In the following for every group a dedicated energy conversion function has been employed. Apparently the heavy component is much more abundant over the whole energy range. This leads to the fact that at the highest energies the statistical errors for the iron spectrum are much smaller than for the hydrogen one. Especially the iron spectrum can be thought as composed of two power laws with a kink at an energy of about  $6 - 7 \cdot 10^{16}$  eV. On the basis of Figure 6.8 the question on the detailed shape can not be unambiguously

answered. The general behavior of the spectra is in good agreement with the findings in [Ape11]. The index change for the electron-poor component found in this thesis is at a slightly lower energy than in the aforementioned paper. One reason for this could be the reconstruction of the energy spectrum just on basis of electron number. Whereas in [Ape11] the spectra are reconstructed with a method which is based on electron and muon number. So it seems that the lack of the muon information shifts the spectra slightly towards lower energies.

### 6.4.1 Comparison with deconvolution analysis results

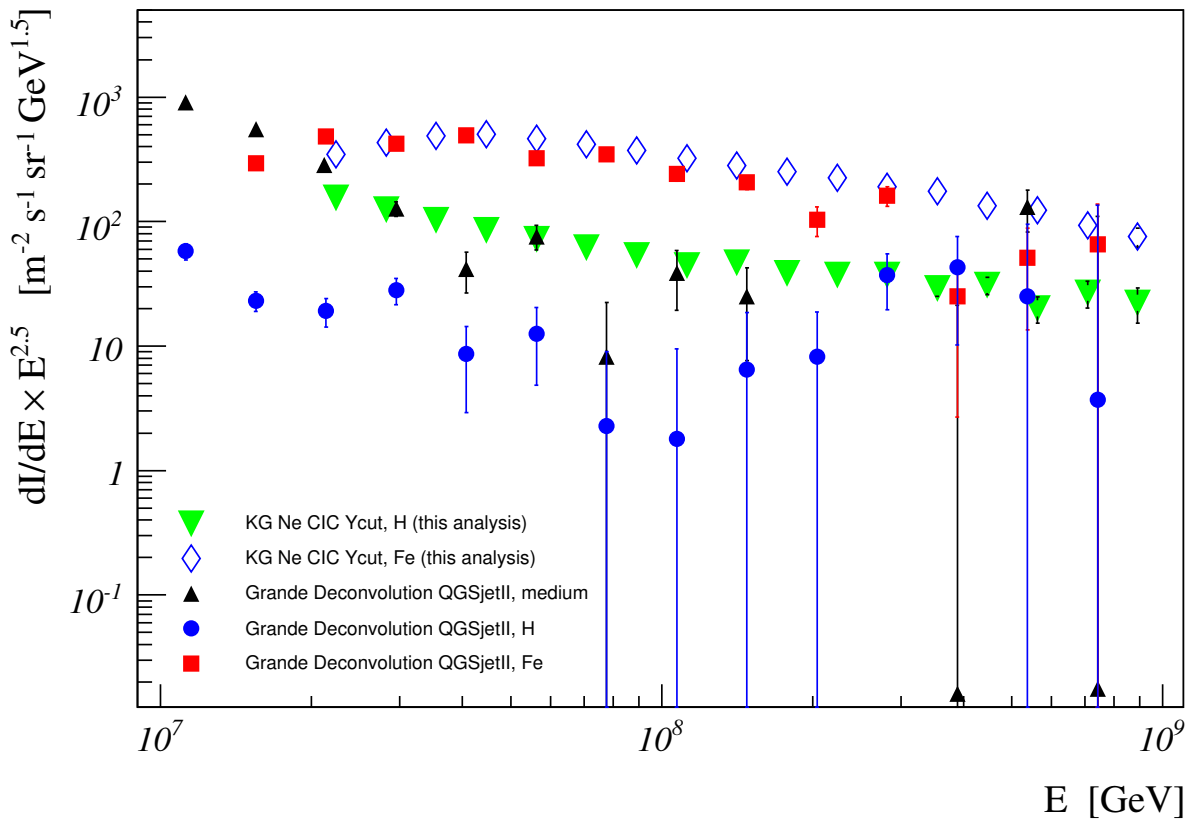


Figure 6.9: Energy spectra for electron-rich and electron-poor data samples, reconstructed with the corresponding energy calibration functions based on QGSjetII simulations in comparison with the results of the deconvolution analysis [Fin11].

The KASCADE experiment has shown that the kink in the energy spectrum is caused by the index change of the light component (confer Section 2.1). This result was based on the deconvolution analysis of KASCADE data. This special type of analysis is at the moment the only way to infer many spectra corresponding to different mass groups. The mass resolution of most other methods is just good enough for the reconstruction

of a light-like and heavy-like energy spectrum (respectively electron-rich and electron-poor). Hence the spectra of this analysis (Figure 6.8) are compared with the results of the current deconvolution analysis of KASCADE-Grande data in Figure 6.9. The energy spectrum of the deconvolution analysis begins already at smaller energies because in the unfolding analysis are events just up to a zenith angle of  $18^\circ$  taken into account and in addition a different energy binning was used (for details vide [Fin11]). As in the chapter 5 described in this thesis all experimental data from events with a zenith angle of maximal  $40^\circ$  are analysed. The spectra start at slightly higher energies due to the shift in the full efficiency for the detector. In general, it can be stated that the two results are inside the region given by the uncertainties completely compatible. It seems that the iron result from the deconvolution analysis directly matches the result for the heavy component from this analysis. Both spectra are compatible to a possible iron knee at an energy of approximately  $7 \cdot 10^{16}$  eV. The flux values of the light spectrum of this analysis are consistent with the sum of the two lighter spectra of the deconvolution analysis. So the two analyses are absolutely consistent.



# Chapter 7

## The Pierre Auger Observatory

The method presented in this work for the reconstruction of the cosmic ray energy spectrum shows certain deficiencies. Especially the dependence on high-energy hadronic interaction models is a dominant factor of uncertainty. To circumvent this dependence fluorescence data from the Pierre Auger Observatory can be used to calibrate the KASCADE-Grande electron number spectrum. Fluorescence measurements have the advantage of not relying on shower simulations for the energy assignment. In addition, with data from HEAT an overlapp region in energy with KASCADE-Grande enables the application of an energy conversion function which contains the cosmic ray composition. In this chapter the Pierre Auger Observatory is briefly described. It is currently the largest detector for ultra-high-energy cosmic rays. Its unique hybrid detection technique allows for very precise measurements of cosmic rays. In addition the HEAT extension enlarges the measurement range down to approximately  $10^{17}$  eV, creating an overlapp range in energy of one decade with the KASCADE-Grande experiment.

### 7.1 Pierre Auger Observatory

The Pierre Auger detector is the currently largest cosmic ray detector in the world [Abr04]. Its operation is done by an international collaboration of physicists from eighteen countries. It is located in Argentina roughly 400 km to the South of Mendoza in the Pampa Amarilla near the city of Malargüe. The whole detector is covering an area of about  $3000 \text{ km}^2$ , even a fifth bigger than the smallest area state in Germany.

By combining a ground array of water cerenkov detectors with four fluorescence telescope stations unique detection possibilities are achieved. In addition, the area covered by the surface detector is overlooked by four fluorescence detector stations each housing six fluorescence telescopes.

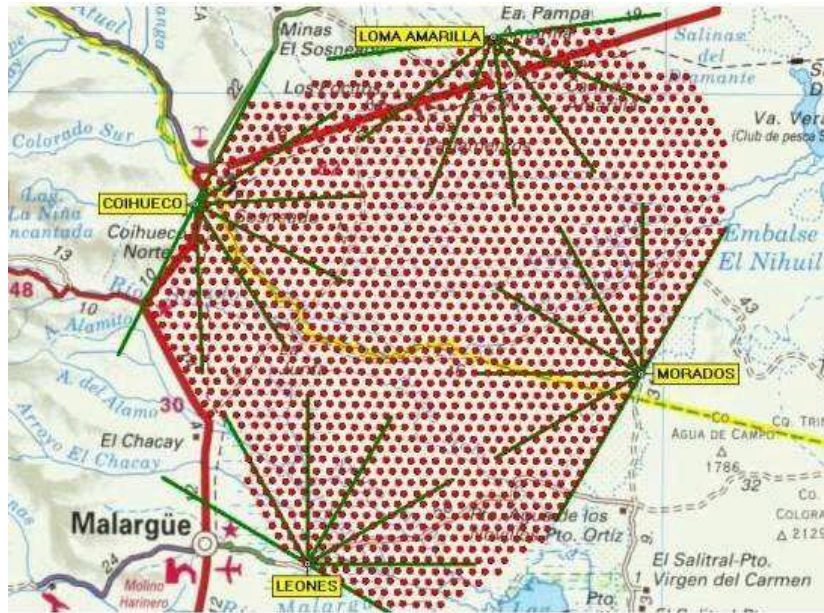


Figure 7.1: The distribution of the Auger detector stations in the Pampa Amarilla. The red dots represent the surface detector stations overlooked by the four fluorescence telescope stations from the border of the array.

### 7.1.1 Surface Detector

The array of particle detectors of the observatory [All08] consists of 1600 Water Cerenkov stations distributed on an area of  $3000 \text{ km}^2$ . In Figure 7.1 the arrangement of the surface detector stations is depicted. The mean mutual distance of each two surface detector stations is  $\approx 1.5 \text{ km}$  and they are arranged on a triangular grid. One station is built by a tank containing 12 tons of purified water which is monitored by three photomultipliers. The stations are completely self-sufficient. Power supply is provided by a solar panel and the collected data is transferred wirelessly to the central campus in Malargüe. The great advantage of the surface detector with respect to the fluorescence telescopes is its 100% duty cycle. The surface detector is operating with full efficiency above an energy of  $3 \cdot 10^{18} \text{ eV}$ .

### 7.1.2 Fluorescence Detector

There are 4 fluorescence telescope stations surrounding the surface detector array each one consisting of 6 actual telescopes [Abr10b]. One telescope is monitoring the air above the area in a field of view from  $0$  to  $30^\circ$  inclination and detects directly the produced fluorescence light stemming from the nitrogen molecules which were excited by the air shower electrons. The light makes its path through the optical lens of a telescope and is finally focused to a photomultiplier camera by a mirror made of anodised aluminum.

The whole telescope buildings are remotely controlled from the central campus station, i. e. the shutters, power sockets etc. can be steered from the control room in Malargüe.

## 7.2 HEAT

The **H**igh **E**levation **A**uger **T**elescopes [Mat11] are the extension to low energies of the Pierre Auger Observatory. By the additional three fluorescence telescopes at the Coihueco site the energy threshold of the observatory is lowered by approximately one decade to  $\approx 10^{17}$  eV. The special design of HEAT allows for the detection of air showers stemming from cosmic rays with lower energy. Every HEAT telescope is installed in a steel container which is pivot-mounted (confer Figure 7.2) and can be elevated from 0 to  $29^\circ$ . So the field of view of the telescopes ranges from  $29$  to  $59^\circ$  in upward mode and directly complements the measurement range of the Coihueco telescope station towards regions higher up in the atmosphere.

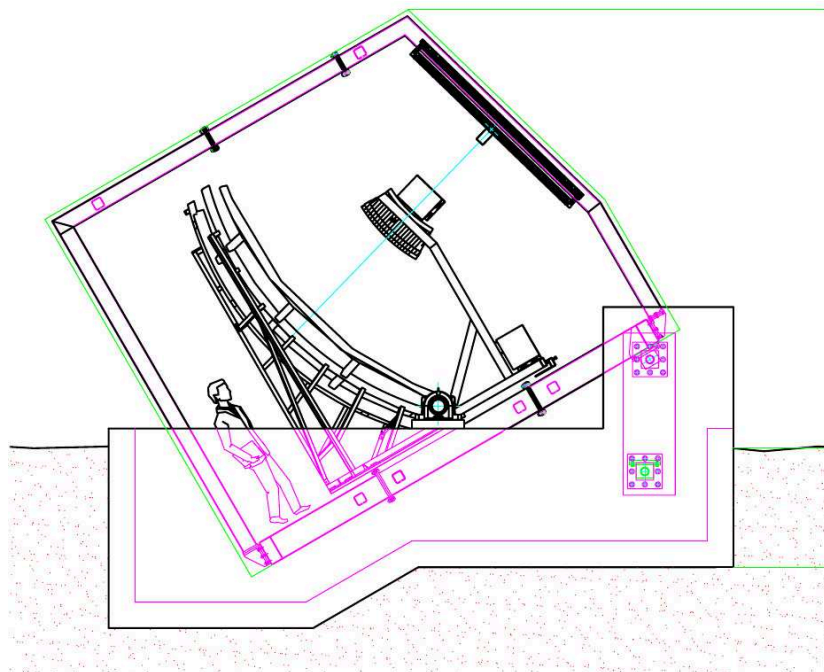


Figure 7.2: Sketch of the HEAT detector station in upward mode.

Figure 7.3 shows the field of view of the HEAT telescopes in downward and upward mode. In addition a schematical longitudinal shower profile is included in the sketch. For this special event the shower maximum in the longitudinal distribution is only in the measurement range for the upward mode of the telescopes.

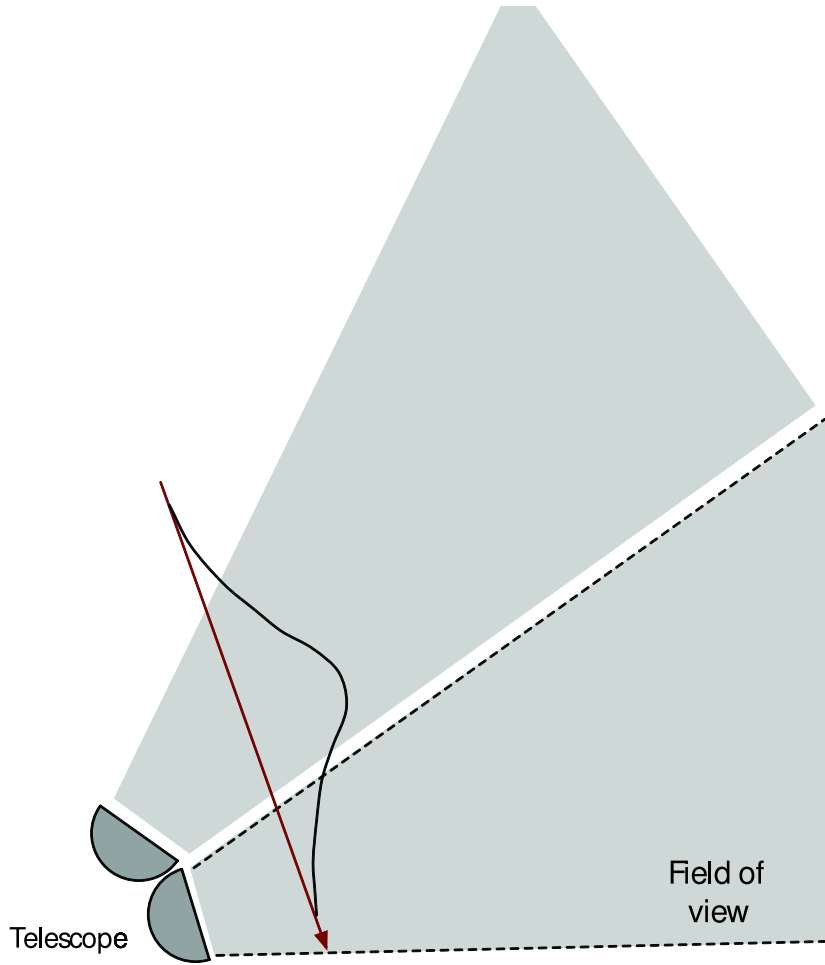


Figure 7.3: The field of view of the HEAT detector in upward and downward mode.

### 7.2.1 Reconstruction

Details for the reconstruction can be found in [Ung08]. In the following a brief overview is given. The image in the camera together with the detector position is used to define the shower detector plane. Afterwards by application of a  $\chi^2$  minimization to the timing information the actual shower axis lying in the shower detector plane can be determined. When the shower geometry is reconstructed the next step is the determination of a light profile. This is done by a calculation from the ADC-signal over time traces of the photomultipliers. An example for a longitudinal light profile is given in the left part of Figure 7.4. By a complex algorithm the longitudinal energy deposit profile is calculated from the longitudinal light profile. The right part of Figure 7.4 shows the energy deposit profile for an arbitrary fluorescence detector event together with a fitted Gaisser-Hillas function. The general reconstruction chain for HEAT fluorescence events is almost the same as for the usual fluorescence telescopes. The whole

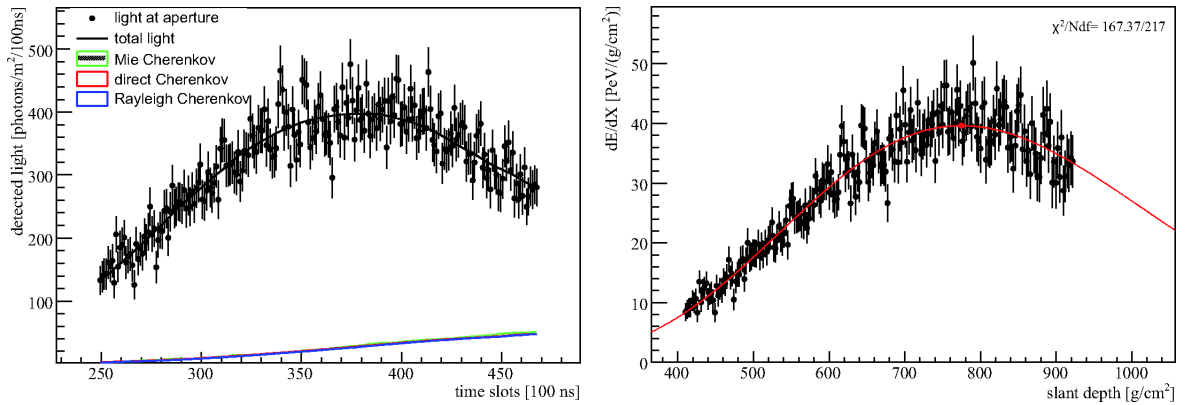


Figure 7.4: Typical fluorescence events. Left: Longitudinal light profile. Right: Longitudinal energy deposit profile (taken from [Mar08]).

procedure is embedded in the Offline code. Special adjustments that had to be made in the Offline code concerning HEAT features are described in [Fal10]. In Addition first tentative data are presented in the latter paper.



# Chapter 8

## Cross Calibration

In this chapter the process of cross calibration of the fluorescence data of HEAT with the KASCADE-Grande data is described. The general advantage of the method is the independence from composition assumptions. So far in the reconstruction of the all-particle energy spectrum with the constant intensity cut method as described in chapter 5, for the transition from size to energy a certain composition has to be assumed. In particular for the selection of the simulations on whose basis the energy conversion function is determined. This composition assumption is the biggest source for systematic uncertainties in the whole reconstruction procedure. By the application of HEAT data for the energy calibration this caveat can be eliminated. With the constraint of complete isotropy it is obvious that there is the same composition in cosmic rays for the Pierre Auger Observatory as for the KASCADE-Grande detector. Thus the energy conversion function obtained with HEAT fluorescence data is also valid for KASCADE-Grande data and solves the problem of the mass dependence.

### 8.1 HEAT Electron Size

The main observables which are reconstructed by the fluorescence telescopes are the longitudinal energy deposit and light profiles. In KASCADE-Grande the main observables are numbers of electrons and muons at observation level. The main goal of this section is to provide an electron size like observable which can easily be determined by the HEAT detector. By the application of a mean energy deposit per particle ( $\langle \alpha \rangle$ ) the longitudinal energy deposit profile can be converted in a longitudinal electron profile. For the here presented work a value of  $\langle \alpha \rangle = 2.56 \frac{\text{MeV}}{\text{g}\cdot\text{cm}^2}$  is always applied. The latter value follows directly at the shower maximum from the analytical expression given in [Ner06]. The cut energy underlying the simulations corresponds to 1 MeV, this means that electrons with lower energies are not further taken into account in the simulation process. A comprehensive overview on the choice of the mean energy deposit per particle is given in an article by Nerling [Ner06]. Therein the universal function of mean ionisation loss rate  $\alpha_{eff}$  subject to shower age on the basis

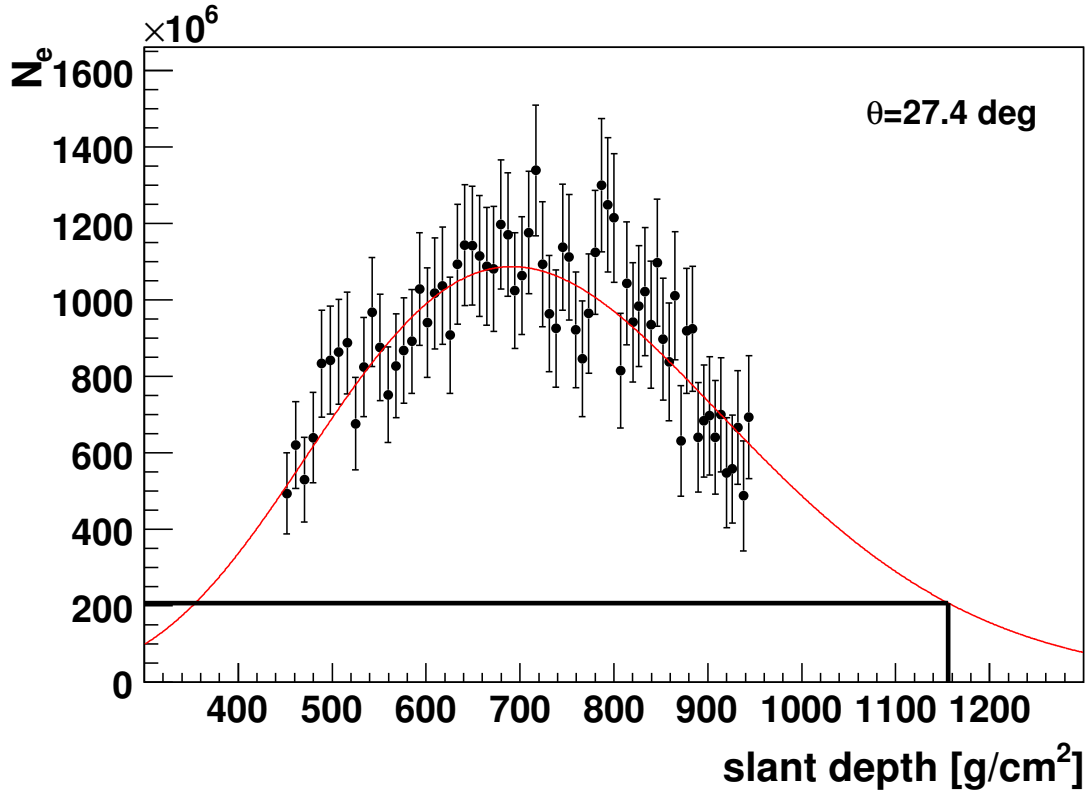


Figure 8.1: Longitudinal electron size profile for an arbitrary auger event. The plotted function is the Gaisser-Hillas fit.

of CORSIKA simulations is given. Again like for the energy deposit the best fitting function is a Gaisser-Hillas function. Now it is possible to read out the electron size at the corresponding Karlsruhe shower depth just by evaluation of the Gaisser-Hillas function at a column depth of  $1023 \frac{\text{g}}{\text{cm}^2} \cdot 1/\cos \Theta$ , where  $\Theta$  denotes the zenith angle of the air shower event.

The described method for the determination of an electron number for a fluorescence detector event is visualized in Figure 8.1. In this figure the longitudinal electron number profile for an arbitrary chosen measured fluorescence detector event is shown together with the applied Gaisser-Hillas fit. The horizontal line symbolises the evaluation of the fit function at the corresponding shower depth of the KASCADE-Grande experiment. So this special event would have been measured in Karlsruhe with an electron number of  $2 \cdot 10^8$ . This method introduces a slight uncertainty due to the fact that data in the tail of the distribution is used and has therefore to be considered as extrapolation. But it is the only way for a connection between fluorescence measurements at these high altitudes with particle detector measurements at almost sea level.

## 8.2 Atmospheric Influence

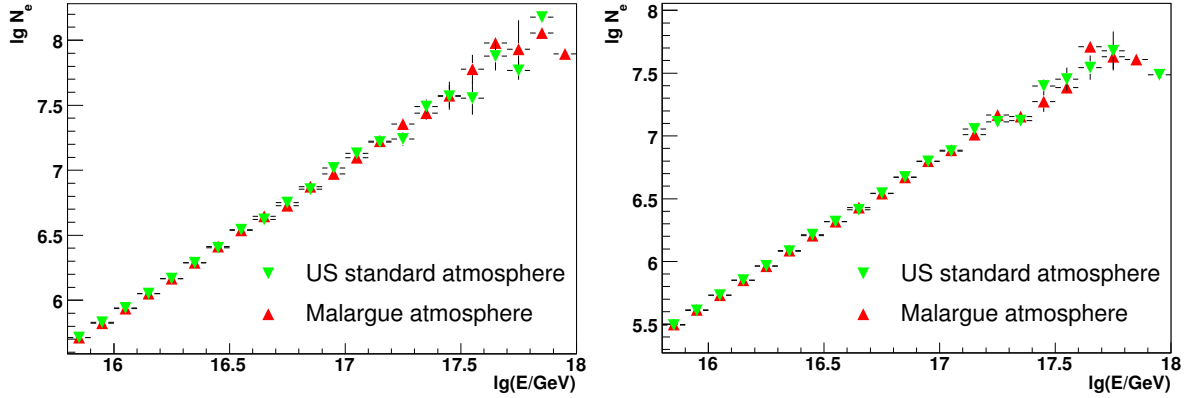


Figure 8.2: Electron size as function of energy for two different atmospheric models from Conex simulations. On the left-hand side for hydrogen, on the right-hand side for iron primary particles.

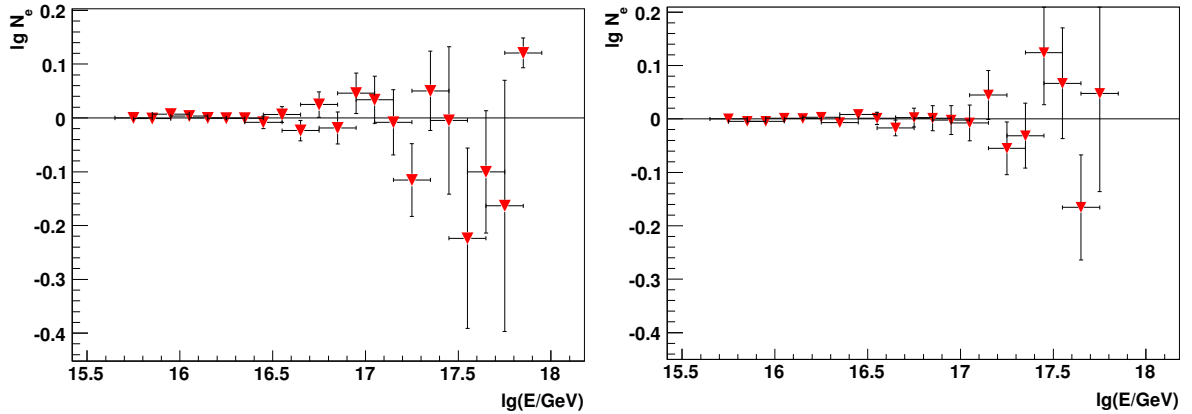


Figure 8.3: Residuals for Conex simulations electron size as function of energy for two different atmospheric models. On the left-hand side for hydrogen, on the right-hand side for iron primary particles.

One aspect which could lead to severe differences when directly comparing measurements in Malargüe and Karlsruhe could result from the different atmospheric conditions. In Malargüe the climate is much less humid than in the south west of Germany. In contrast to the typical german climatic conditions in the middle west of argentina there is a more desert like average behaviour of the weather. For investigating these problems a set of Conex [Ber07] simulations has been produced with the implementation of different atmospheric models. Conex is a shower simulation program with a dimensional semi analytic approach, that's the reason for the low consumption of cpu resources. Therefore it's possible to simulate a set with sufficient statistics on an

acceptable time scale. In the produced simulations there exist each two sets with 50000 events for hydrogen and iron induced air showers. For every set the primary particle's energy lies in the intervall of  $6.3 \cdot 10^{15} - 1 \cdot 10^{18}$  eV following an energy spectrum which is proportional to a power law with an index of  $\gamma = 3$ . The zenith angles are uniformly distributed between 0 and  $40^\circ$ . For every primary particle type there exist two sets with two alternating atmospheric parametrisations. For the Karlsruhe atmosphere the usually already implemented US standard atmosphere was used. In contrast to describe the atmospheric conditions in Argentina a parametrisation by Keilhauer [Kei04] was implemented in Conex. The latter parametrisation for the different atmospheric layers is based upon balloon measurements which were directly performed at site of the Pierre Auger Observatory. For the simulated data the energy conversion data are compared for the two different atmospheres. In Figure 8.2 the electron size as a function of energy is depicted for hydrogen (left) and for iron primary particles, in each case the corresponding atmosphere parametrisation is noted in the graph's legend. For the variable electron size the value for a slant depth of  $1096 \frac{g}{cm^2}$  was taken by evaluation of the longitudinal function given by Conex. The used energy was the EAS's true energy and no further detector simulation was applied. In Figure 8.2 can be recognized that there is no obvious difference for the course of the different functions. Just slight variations at the high energy border can be seen. At these energies the statistics is very low and therefore the data are not very robust.

Neither for the lightest nor for the heaviest particles any severe problems can be stated concerning the aspect of different atmospheres. Especially when looking at Figure 8.3, which shows the difference between each two simulation sets with different atmospheric parameters, the non-existence of any severe differences can be confirmed. The plotted residuals are totally compatible with the zero hypothesis. So from this point of view there are no objections to cross calibrating the data from these two experiments.

### 8.3 Cross Calibration

For the calibration of KASCADE-Grande data in every HEAT event the electron size at a slant depth corresponding to a shower arriving at the KASCADE-Grande detector under the reference angle of  $21^\circ$  is chosen as described in Section 8.1. So all electron size values in Figure 8.4 are extrapolated at an atmospheric depth of

$$X_{21^\circ}^{KG} = 1023 \frac{g}{cm^2} \cdot \sec 21^\circ = 1096 \frac{g}{cm^2}.$$

The function adapted to every longitudinal profile is called Gaisser-Hillas function and has the following form:

$$\lg N_e(X) = N_{e,max} \left( \frac{X - X_1}{X_{max} - X_1} \right)^{\frac{X_{max} - X_1}{\lambda}} e^{\left( \frac{X_{max} - X}{\lambda} \right)}. \quad (8.1)$$

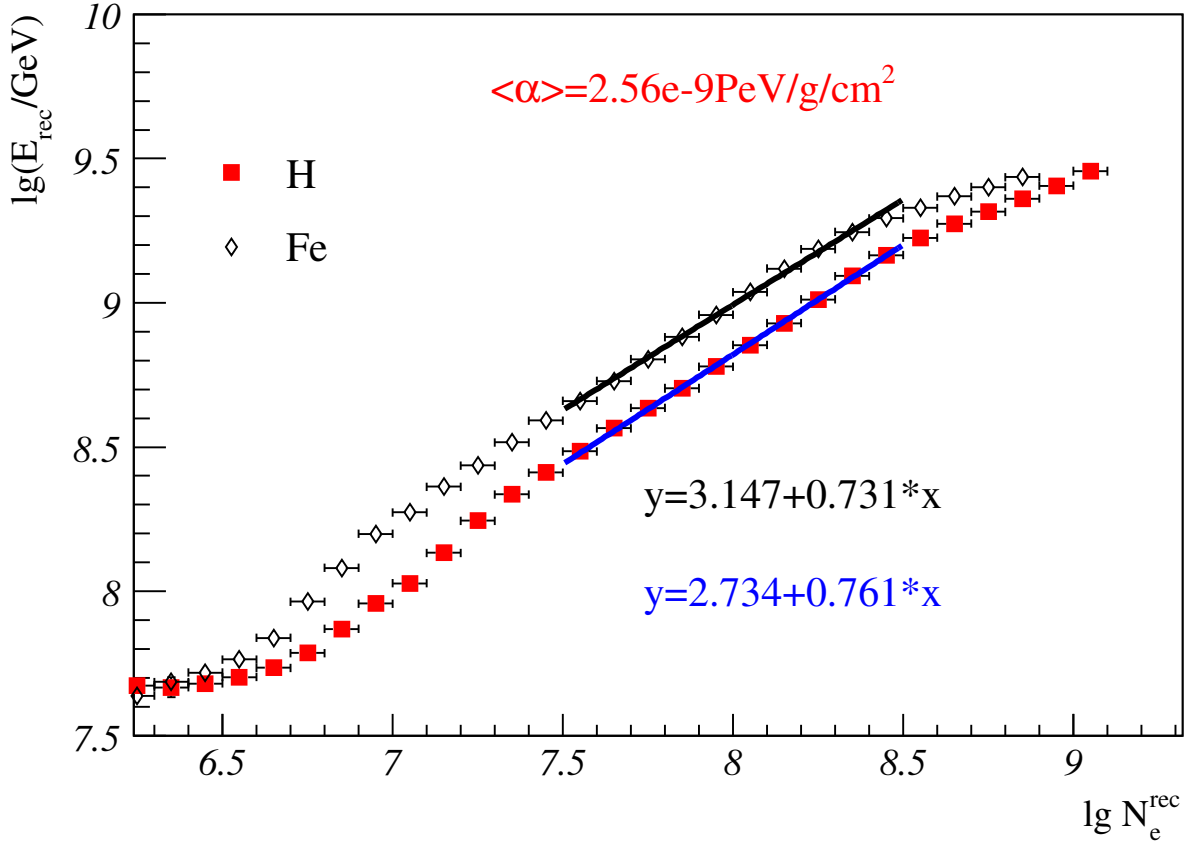


Figure 8.4: Energy conversion functions from HEAT simulations.

In this equation  $X_{max}$  is the column depth at which the longitudinal shower profile has its maximum,  $X_1$  is the depth of first interaction and  $\lambda$  is an effective radiation length ( $\approx 70 \frac{\text{g}}{\text{cm}^2}$ ).

In the following, Conex simulations for hydrogen and iron primary particles with afterwards applied detector simulations of HEAT embedded in the Offline code are used for the determination of a electron number - energy conversion relation. The simulations used range from an energy of  $5 \cdot 10^{16}$  to  $5 \cdot 10^{18}$  eV and follow a spectrum with index  $\gamma = 2$ . In Figure 8.4 the reconstructed energy as function of extrapolated number of electrons is shown for the assumption of a pure hydrogen respectively iron composition. A linear relation is assumed and determined by a fit in the intermediate energy range (for parameters see Figure 8.4).

This relation is applied to KASCADE-Grande data of the corrected electron number spectrum (Figure 5.6) in order to reconstruct an energy spectrum. The result is shown in Figure 8.5. The first two points of the spectra show clear threshold effects, i. e. the spectra run in an energy range where the detector does not work at full efficiency. It can be stated that the general order of magnitude is the right one, so the method works.

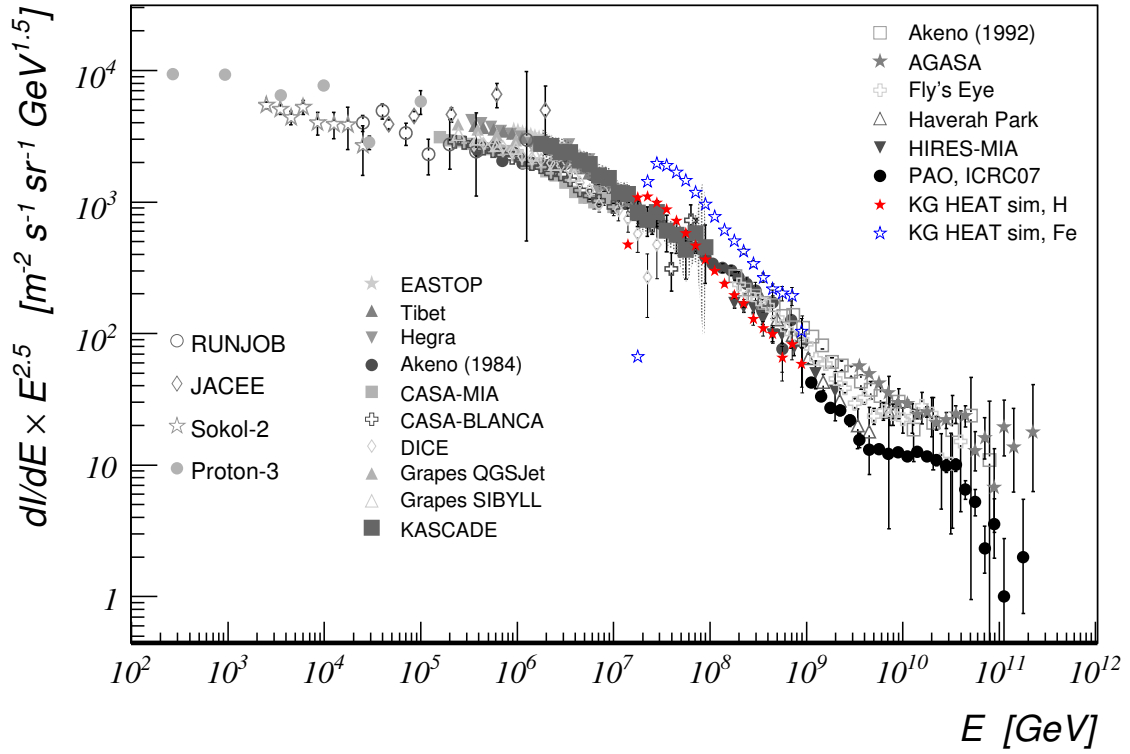


Figure 8.5: Energy spectrum with KASCADE-Grande data converted by HEAT simulations energy size relation function.

However the slopes of the reconstructed spectra seem not to be the same as for the results of the other experiments. Probably this is induced by a not perfect simulation of the HEAT telescopes. In the near future the presented method for cross calibrating KASCADE-Grande with HEAT data can be accomplished with a high statistics and quality measured data sample from the HEAT telescopes. In addition, further improvements like a deconvolution analysis are conceivable. In addition, further investigations of the threshold regions and effects of the extrapolations in determination of the electron number like observable will be necessary.

# Chapter 9

## Conclusion

The precise measurement of the cosmic ray energy spectrum and composition is an important key for the validation of models of cosmic ray sources and propagation. Especially the energy range between  $10^{16}$  and  $10^{18}$  eV, just after the knee and before the advent of the extragalactic component, is an interesting range in which new physical features are expected (like a knee of the heavy component). This work has provided a precise reconstruction of the energy spectrum of cosmic rays in the energy range of  $10^{16} - 10^{18}$  eV. Basis for the analysis have been data measured by the KASCADE-Grande experiment which have been processed with KRETA version 1.1901. It has been shown that the KASCADE-Grande data are understood with unprecedented precision. The relative uncertainty in the determination of electron number is smaller than 2% over a wide range in zenith angle. This shows that the reconstruction software KRETA v1.1901 which has been used the first time in this work, delivers very accurate air shower parameters.

The extensive air showers are reconstructed by the KASCADE-Grande detector with a core resolution of  $\approx 5$  m, a zenith angle resolution of  $\approx 0.5^\circ$ , a logarithmic electron number resolution of 0.07, and a logarithmic muon number resolution of 0.06. In this thesis, KASCADE-Grande data taken from December 2003 until February 2011 have been analysed. By a constant intensity cut method the electron number spectrum corrected to a zenith angle of  $21^\circ$  for extensive air showers in a zenith angle interval of  $0$  to  $40^\circ$  was determined. The electron number spectrum shows no significant structures. Different methods for the conversion to primary particle's energy have been developed. With the help of an unfolding procedure the energy spectrum for cosmic rays is reconstructed taking into account shower fluctuations. This spectrum shows a kink-like structure just below  $10^{17}$  eV. A method which uses the electron-muon ratio was applied to infer an electron-poor (heavy-like) and an electron-rich (light-like) energy spectrum. The spectrum of the heavy-like component shows a change of the power index at  $\approx 7 \cdot 10^{16}$  eV. These findings are compatible with other methods of reconstruction of the energy spectrum for KASCADE-Grande data [Ape11]. Especially the

features of the heavy-like component's energy spectrum favour the acceleration models with a rigidity dependent position of the maximal energy, like e. g. in supernova remnants. However, the change of the heavy-like component's energy spectrum is not as hard as for the hydrogen knee at  $\approx 2$  PeV [Ulr04]. This fact could be explained by the existence of another kind of sources inside our galaxy which produces also a rigidity dependent maximum acceleration energy but higher than the ones causing the hydrogen knee. These sources could be supernova remnants of type IIb for which Ptuskin et al. report a maximum energy of accelerated iron ions of 5 EeV [Ptu10]. But to solve these puzzles, it is necessary to measure the composition in this energy range with a more precise technique. One step towards a determination of energy spectra of cosmic rays which shows less sources for systematic uncertainties is the cross calibration of the KASCADE-Grande data with HEAT.

The proof of principle for such a cross calibration of the electron component of extensive air showers measured by KASCADE-Grande and the HEAT telescopes of the Pierre Auger Observatory has been provided. In near future, when there is a high quality data set from HEAT, interesting possibilities for ongoing analyses arise. Especially, the systematic uncertainties introduced by the composition dependence and the influence of the hadronic interaction model on the constant intensity cut method can be reduced by using measured cosmic ray data for the cross calibration.

# Appendix A

In this part of the appendix additional graphs are shown, mainly the higher zenith angles are covered. The corresponding pictures of the lateral density functions for the higher angle intervals can be seen in the following.

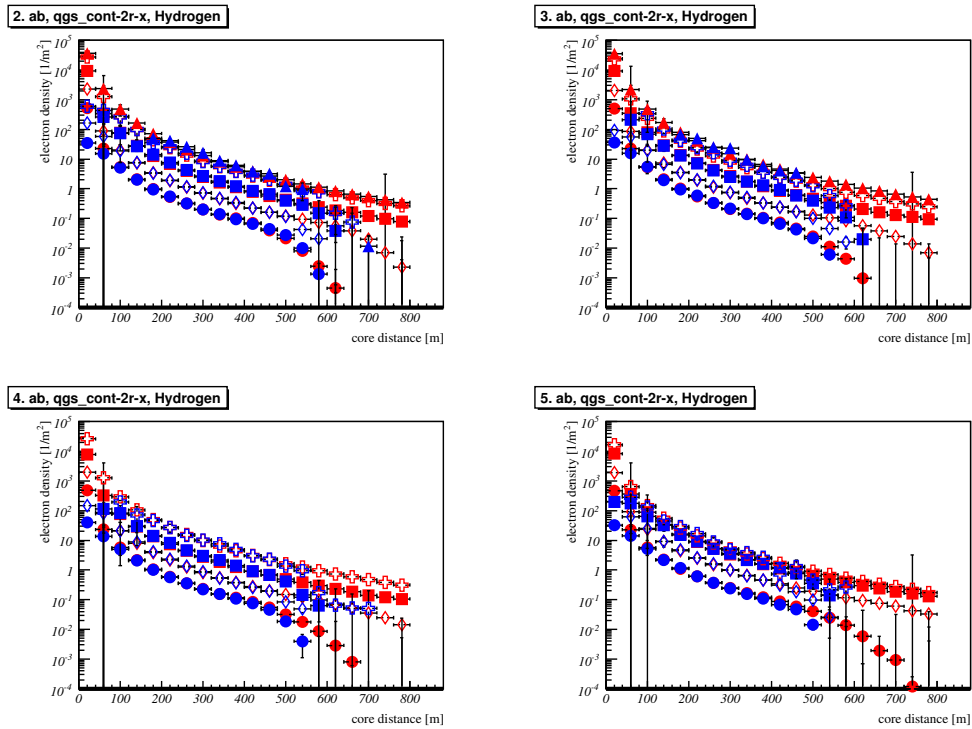


Figure A.1: Comparison of simulated true lateral density functions with full detector simulations. Shown are the results for pure Hydrogen initiated extensive air showers.

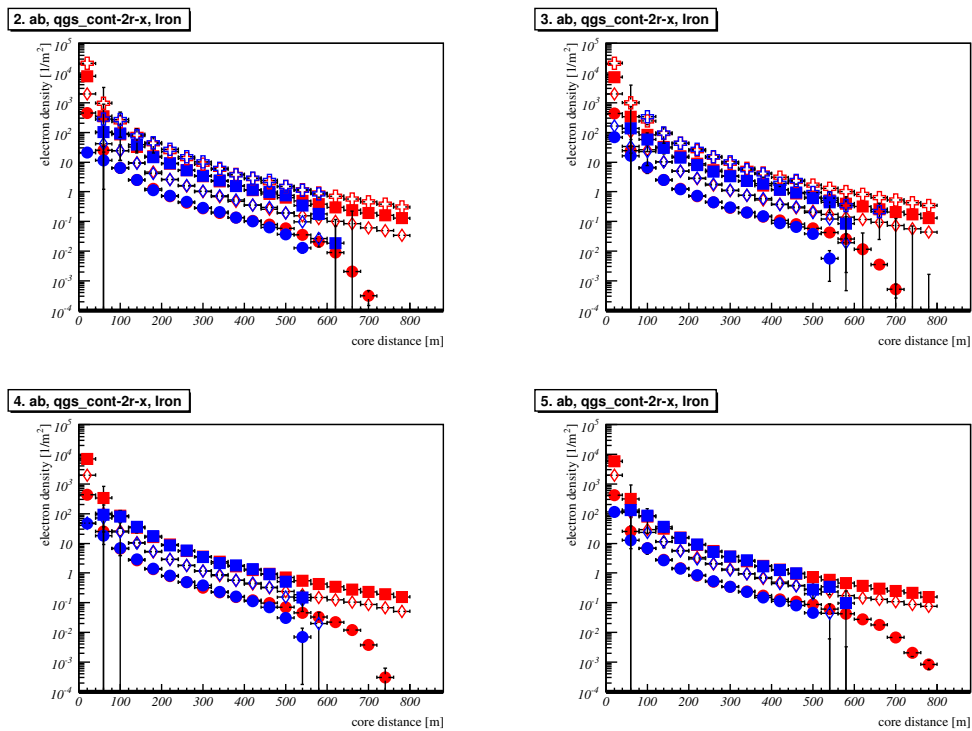


Figure A.2: Simulated true and reconstructed (full detector simulation) lateral density functions for the higher zenith angles.

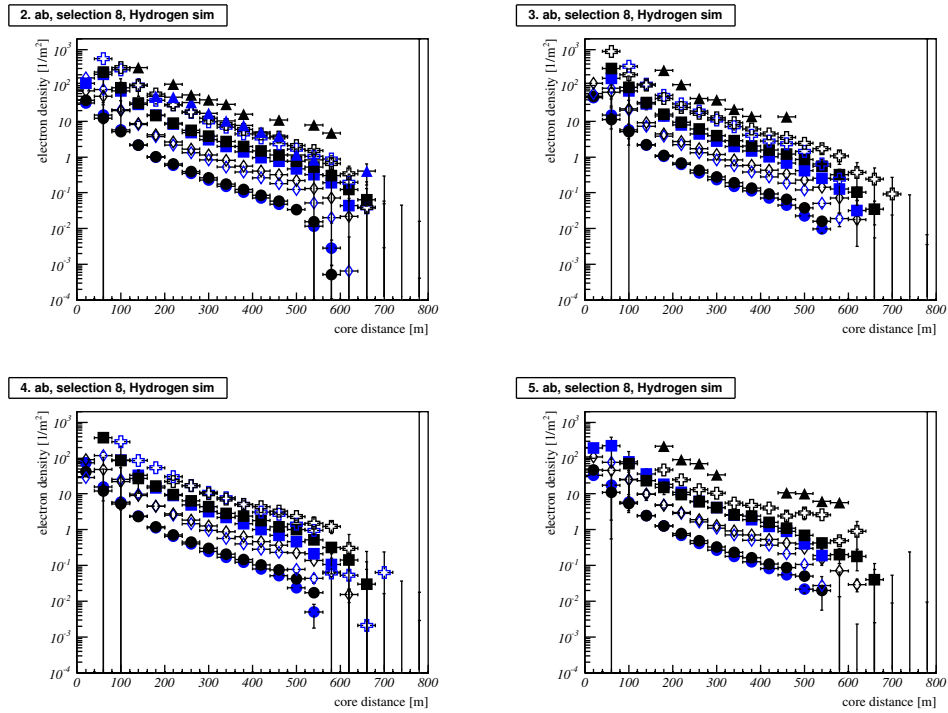


Figure A.3: The comparison of lateral density functions for data and Hydrogen simulations (QGSjetII) for higher shower inclinations.

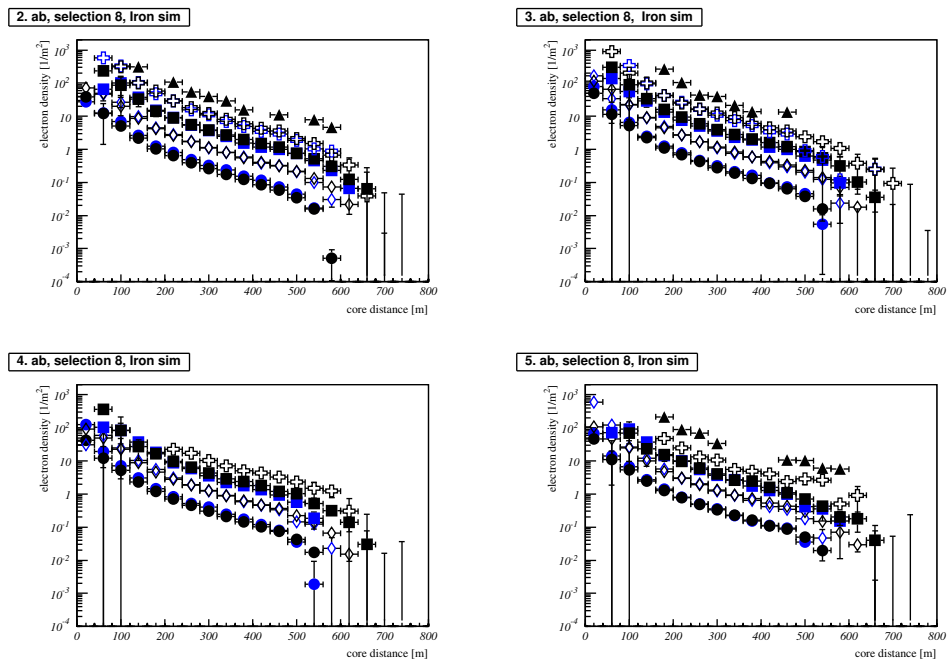


Figure A.4: Compilation of Iron simulations (QGSjetII) and data lateral density functions in the higher zenith angle intervals.

# Appendix B

In this part of the appendix the graphs for the muon size constant intensity cut method are given.

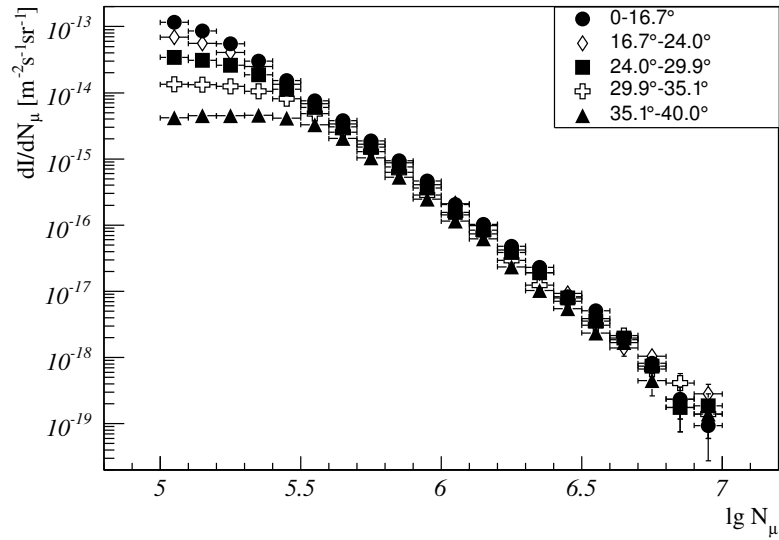


Figure B.1: The differential muon size spectra.

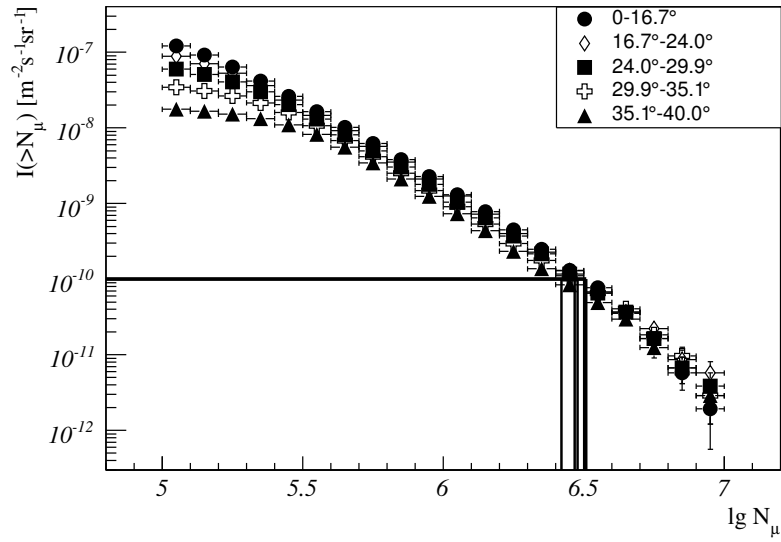


Figure B.2: The integrated muon size spectra.

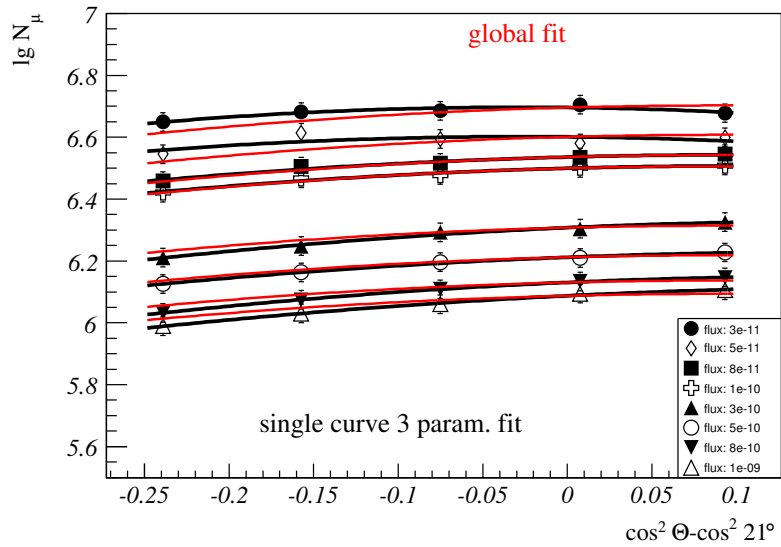


Figure B.3: Attenuation graphs for muon size. The curvature is less pronounced as for electron size due to the weaker attenuation (confer Figure 5.5).

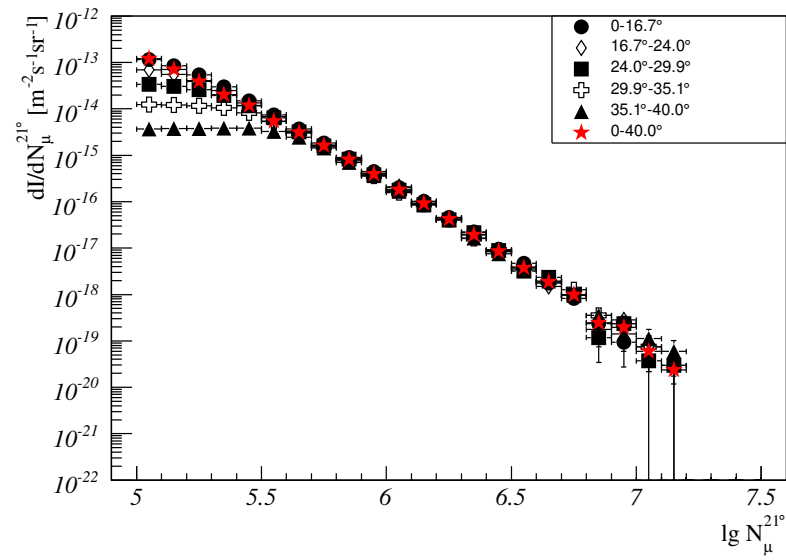


Figure B.4: The spectrum of the to  $21^\circ$  zenith angle corrected muon size.

# Appendix C

In the following the plots for the unfolding energy conversion for a mixed and a pure iron composition are shown.

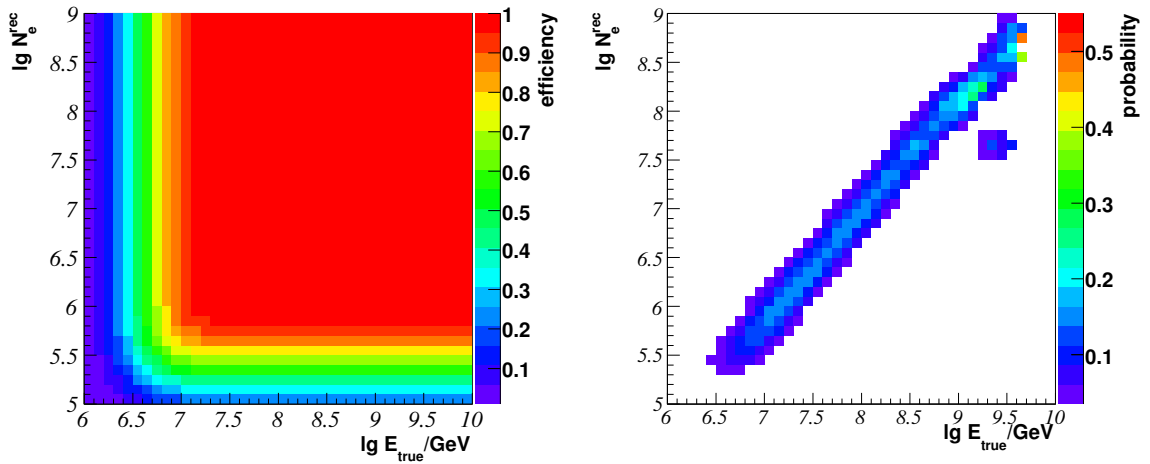


Figure C.1: Basis are the standard simulation sets with QGSjetII in the second angle bin for an even mixture of all five elements as primary particles. Left: The two-dimensional fitted efficiency function in the electron size energy plane. Right: The electron size energy conversion matrix.

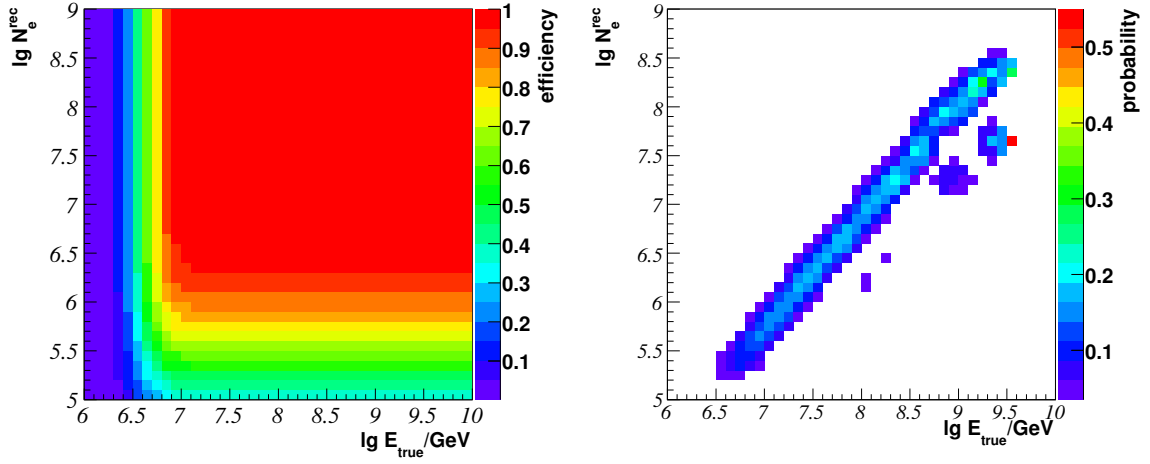


Figure C.2: Basis are the standard simulation sets with QGSjetII in the second angle bin for a iron as primary particles. Left: The two-dimensional fitted efficiency function in the electron size energy plane. Right: The electron size energy conversion matrix.

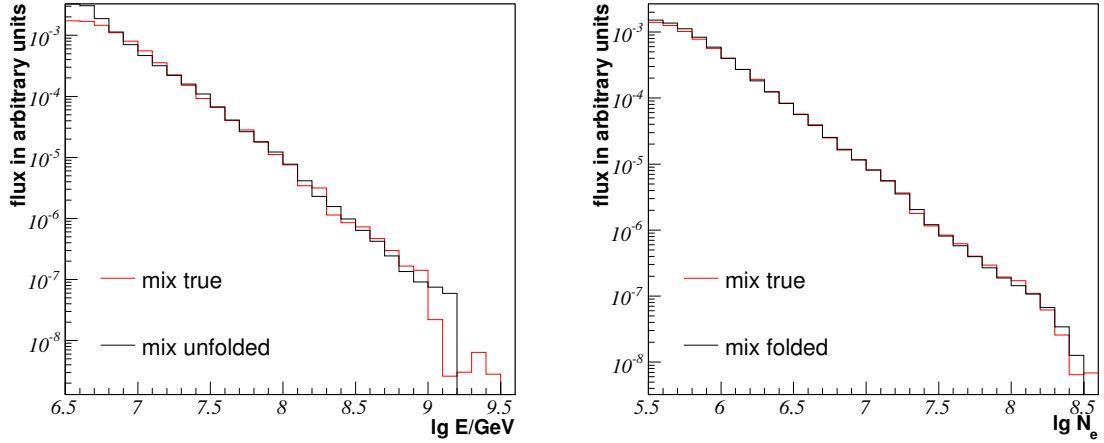


Figure C.3: Both pictures result from the standard simulations with QGSjetII as interaction model in the second angle bin, an even mixture of five elements is used. Left: The comparison of true and unfolded energy spectrum. Right: True and forward folded electron size spectra.

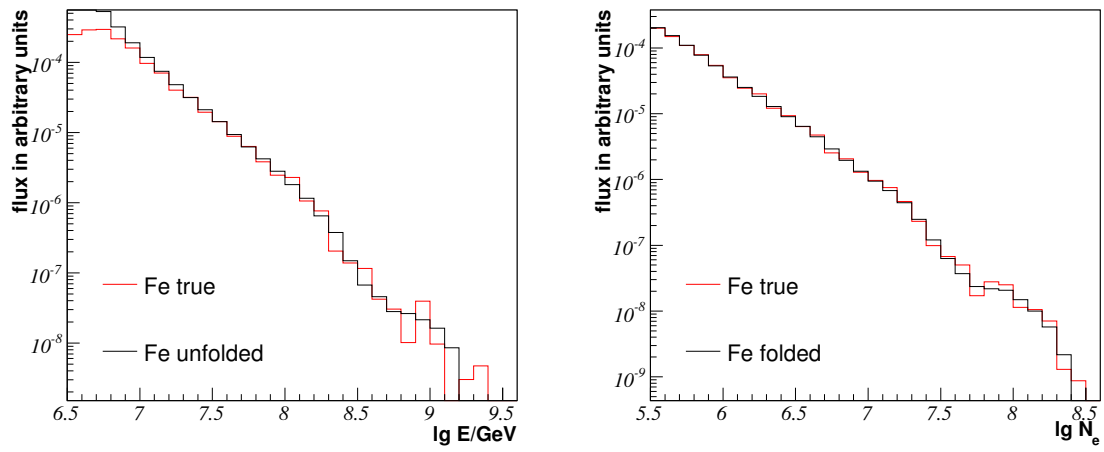


Figure C.4: Both pictures result from the standard simulations with QGSjetII as interaction model in the second angle bin, only iron induced showers are used. Left: The comparison of true and unfolded energy spectrum. Right: True and forward folded electron size spectra.



# Bibliography

- [Abr04] J. Abraham *et al.* [Pierre Auger Collaboration], “Properties and performance of the prototype instrument for the Pierre Auger Observatory”, *Nucl. Instr. and Methods* 523 (2004) 50.
- [Abr07] J. Abraham *et al.* (Pierre Auger Collaboration), “Correlation of the highest energy cosmic rays with nearby extragalactic objects”, *Science* 318 (2007) 938
- [Abr08] J. Abraham *et al.* [Pierre Auger Collaboration], “Upper limit on the cosmic-ray photon flux above  $10^{19}$  eV using the surface detector of the Pierre Auger Observatory”, *Astropart. Phys.* **29** (2008) 243 [arXiv:astro-ph/0712.1147].
- [Abr10a] P. Abreu *et al.* [Pierre Auger Observatory Collaboration], “Update on the correlation of the highest energy cosmic rays with nearby extragalactic matter”, *Astropart. Phys.* **34** (2010) 314
- [Abr10b] J. Abraham *et al.* [The Pierre Auger Collaboration], “The Fluorescence Detector of the Pierre Auger Observatory”, *Nucl. Instrum. Meth. A* **620** (2010) 227
- [Agl88] M. Aglietta *et al.*, *Nucl. Instr. and Meth. A* 277 (1988) 23
- [All08] Pierre Auger Collaboration, I. Allekotte *et al.*, “The Surface Detector System of the Pierre Auger Observatory”, *Nucl. Instr. and Methods A* 586 (2008) 409
- [All75] O. C. Allkofer, *Introduction to Cosmic Radiation*, Verlag Carl Thiemig, München 1975
- [Ant01] T. Antoni *et al.*, *Astropart. Phys.* 14 (2001) 245
- [Ant03] T. Antoni *et al.*, *Nucl. Instr. and Methods A* 513 (2003) 490
- [Ant99] T. Antoni *et al.*, *Nucl. Phys. B, Proc. Suppl.* 75 A (1999) 234

- [Ape05] W. D. Apel *et al.* [KASCADE Collaboration], “Comparison of measured and simulated lateral distributions for electrons and muons with KASCADE”, *Astropart. Phys.* **24** (2006) 467 [arXiv:astro-ph/0510810].
- [Ape11] W. D. Apel *et al.* [KASCADE Collaboration], “Kneelike Structure in the Spectrum of the Heavy Component of Cosmic Rays Observed with KASCADE-Grande”, *Phys. Rev. Lett.* **107** (2011) 171104
- [Art10] J. C. Arteaga *et al.* [KASCADE Collaboration], “The KASCADE-Grande experiment: measurements of the all-particle energy spectrum of cosmic rays”, [arXiv:astro-ph/1009.4716v1]
- [Aug39] P. Auger, P. Ehrenfest, R. Maze, J. Daudin, and R. A. Fréon, *Reviews of Modern Physics* 11 (1939) 288
- [Ber04] E. G. Berezhko, H. J. Völk, *Astron. & Astrophys.* 419 (2004) L27
- [Ber07] Bergmann T. and others, ”One-dimensional hybrid approach to extensive air shower simulation”, *Astropart. Phys.* 26 (2007) 420-432, astro-ph/0606564
- [Ber90] V. S. Berezinskiĭ, S. V. Bulanov, V. A. Dogiel, V. L. Ginzburg and V. S. Ptuskin, *Astrophysics of Cosmic Rays*, North-Holland, Amsterdam 1990
- [Bir95] D. J. Bird *et al.*, *Astrophys. J.* 441 (1995) 144
- [Blo98] V. Blobel, E. Lohrmann, *Statistische und numerische Methoden der Datenanalyse*, B.G.Teubner Stuttgart, Leipzig 1998
- [Blu09] J. Blümer, R. Engel and J. R. Hörandel, *Cosmic Rays from the Knee to the Highest Energies*, *Prog. Part. Nucl. Phys.* **63** (2009), 293-338, 0904.0725
- [Bru93] R. Brun and F. Carminati, GEANT-Detector Description and Simulation Tool, *CERN Program Library Long Writeup*, 1993
- [Bur07] J. van Buren, Investigations of the Muon Component of Extensive Air Showers Measured by KASCADE-Grande, FZKA-7292, Forschungszentrum Karlsruhe 2007
- [Cla63] Clark G. W. *et al.*, *Proc. 8<sup>th</sup> Int. Cosmic Ray Conf.*, Jaipur (1963)
- [Cos09] F. Cossavella, Measurements of High Energy Cosmic Rays above 10 PeV with KASCADE-Grande, FZKA-7513, Forschungszentrum Karlsruhe 2009
- [Dar07] A. Dar, A. de Rújula, arXiv:astro-ph/0008474

- [Dol02] P. Doll et al., *Nucl. Instrum. Meth. A* 488 (2002) 517
- [Eng99] J. Engler et al., *Nucl. Instrum. Meth. A* 427 (1999) 528
- [Ent11] D. d'Enterria, R. Engel, T. Pierog, S. Ostapchenko and K. Werner, arXiv:1101.5596 [astro-ph.HE].
- [Fal05] H. Falcke et al., *Nature* 435 (2005) 313
- [Fal10] S. Falk, D. Kruppke-Hansen, H.-J. Mathes, S. Müller, R. Ulrich, M. Unger, A first look at HEAT data, GAP note 2010-123 , Pierre Auger Observatory, 2010
- [Fas00] A. Fasso, A. Ferrari, P. R. Sala, and J. Ranft, Status and prospective for hadronic applications. Prepared for International Conference on Advanced Monte Carlo for Radiation Physics, Particle Transport Simulation and Applications (MC 2000), Lisbon, Portugal, 23-26 Oct 2000
- [Fin11] M. R. Finger, Reconstruction of energy spectra for different mass groups of high-energy cosmic rays, 2011 doctoral dissertation KIT
- [Gai78] T. K. Gaisser, R. J. Protheroe, K. E. Turver and T. J. L. McComb, *Rev. Mod. Phys.* **50** (1978) 859 [Erratum-ibid. **51** (1979) 649].
- [Gai90] T. K. Gaisser, *Cosmic Rays and Particle Physics*, Cambridge University Press, 1990
- [Gol64] R. Gold, Argonne National Laboratory Report ANL-6984, Argonne, 1964
- [Gre56] K. Greisen, *Prog. Cosmic Ray Physics* Vol. III (1956) 1
- [Gre66] K. Greisen, *Phys. Rev.* 16 (1966) 748
- [Gru00] C. Grupen, *Astroteilchenphysik*, Vieweg, Braunschweig/Wiesbaden 2000
- [Hec98] D. Heck, G. Schatz, T. Thouw, J. Knapp, and J. N. Capdevielle, CORSIKA: A Monte Carlo code to simulate extensive air showers., Forschungszentrum Karlsruhe, FZKA-6019, Forschungszentrum Karlsruhe 1998
- [Hei44] W. Heitler, *Quantum Theory of Radiation*, Oxford University Press, 1944
- [Hes12] V. F. Hess, *Physikalische Zeitschrift* 13 (1912) 1084
- [Hör04] J. R. Hörandel, *Astropart. Phys.* 21 (2004) 241
- [Hör07] J. R. Hörandel, *Modern Physics Letters A* 22 (2007) 1533

- [Jam75] F. James and M. Roos, *Comput. Phys. Commun.* 10 (1975) 343
- [Kal97] N. N. Kalmykov et al., *Nucl. Phys. B (Proc. Suppl.)* 52B (1997) 17
- [Kam58] K. Kamata and J. Nishimura, *Prog. Theoret. Phys. Suppl.* 6 (1958) 93
- [Kei04] B. Keilhauer, *Astroparticle Physics* 22 (2004) 249
- [Lon81] M. S. Longair, *High energy astrophysics*, Cambridge University Press, 1981
- [Mai03] G. Maier, doctoral dissertation (2003), Karlsruhe Institute of Technology (KIT)
- [Mar08] I. C. Mariş, Measurement of the Ultra High Energy Cosmic Ray Flux using Data of the Pierre Auger Observatory, 2011 doctoral dissertation KIT
- [Mat05] J. Matthews, *Astropart. Phys.* 22 (2005) 387
- [Mat11] H.-J. Mathes et al., The HEAT Telescopes of the Pierre Auger Observatory. Status and First Data, proceedings of the 32nd International Cosmic Ray Conference, Beijing, China (2011), arXiv:1107.4807v1 [astro-ph.IM]
- [Mül03] M. Müller, Untersuchung unbegleiteter Hadronen in durch kosmische Strahlung induzierten Luftschauern im Bereich bis einem PeV, FZKA-6912, Forschungszentrum Karlsruhe 2003
- [Mül07] D. Müller et al., *Proc. 30<sup>th</sup> Int. Cosmic Ray Conf.*, Merida (2007)
- [Nav04] G. Navarra et al., *Nucl. Instr. and Methods A* 518 (2004) 207
- [Neh08] S. Nehls, Calibrated Measurements of the Radio Emission of Cosmic Ray Air Showers, FZKA-7440, Forschungszentrum Karlsruhe 2008
- [Nel85] W. R. Nelson, H. Hirayama, D. W. O. Rogers, Stanford Linear Accelerator Center SLAC 265 (1985)
- [Ner06] F. Nerling, J. Blümer, R. Engel, M. Risse, 'Universality of electron distributions in high-energy air showers - Description of Cherenkov light production', *Astroparticle Physics* 24 (2006) 421
- [Ost06] S. Ostapchenko, *Nucl. Phys. (Proc. Suppl.)* 151 (2006) 143
- [Ove07] S. Over et al., Search for anisotropy and point sources of cosmic rays with the KASCADE-Grande experiment, proceedings of the 30th International Cosmic Ray Conference, Merida, Mexico (2007)

- [Pie07] F. Di Pierro et al., Shower size spectrum reconstructed with KASCADE-Grande, FZKA-7340, Forschungszentrum Karlsruhe 2007
- [Pla02] R. Plaga, *New Astronomy* 7 (2002) 317
- [Ptu10] V. Ptuskin et al., *Astrophysical Journal* 718 (2010) 31
- [Ulr04] H. Ulrich, Untersuchungen zum primären Energiespektrum der kosmischen Strahlung im PeV-Bereich mit dem KASCADE-Experiment, FZKA-6952, Forschungszentrum Karlsruhe 2004
- [Ung08] M. Unger et al., Reconstruction of Longitudinal Profiles of Ultra-High Energy Cosmic Ray Showers from Fluorescence and Cherenkov Light Measurements, [arXiv:astro-ph/0801.4309], 2008
- [Völ04] H. J. Völk et al., *Nature* 432 (2004) 75
- [Wer06] K. Werner et al., *Phys. Rev. C* 74 044902 (2006)
- [Zat66] V. I. Zatsepin and V. A. Kuz'min, *JETP* 4 (1966) 78



# Danksagung

An dieser Stelle möchte ich allen danken, die zum Gelingen dieser Arbeit beigetragen haben.

Mein Dank gilt:

- Herrn Prof. Dr. Johannes Blümer für die Ermöglichung dieser Arbeit am Institut für Experimentelle Kernphysik und die Übernahme des Referats.
- Herrn Prof. Dr. Thomas Müller für die Übernahme des Korreferats.
- Herrn Dr. Andreas Haungs für die Betreuung dieser Arbeit und seine vielen Ratschläge.
- Frau Dr. Fabiana Cossavella, Frau Dr. Donghwa Kang, sowie den Herrn Dr. Paul Doll, Dr. Jürgen Wochele, Dr. Marcel Finger, Dr. Sven Over, Dr. Hans-Jürgen Mayer und Dr. Michael Unger für die ständige Hilfs- und Diskussionsbereitschaft.
- allen explizit nicht genannten Mitgliedern der Auger-, LOPES- und KASCADE-Grande- Kollaborationen für die angenehme Zusammenarbeit.

Besonderer Dank gilt meinen Eltern für ihre fortwährende Unterstützung, ohne die die Anfertigung dieser Arbeit nicht möglich gewesen wäre.

Karlsruhe, den 16. Dezember 2011

Michael Wommer



Hiermit versichere ich, dass ich die vorliegende Arbeit selbstständig und nur unter Verwendung der angegebenen Quellen angefertigt habe.

Karlsruhe, den 16. Dezember 2011

Michael Wommer